



Norwegian University of  
Science and Technology

# Displacement of Non-Newtonian Fluids in Annular Spaces

**Tri Thanh Nguyen**

Mechanical Engineering

Submission date: June 2018

Supervisor: Tor Ytrehus, EPT

Co-supervisor: Reidar Kristoffersen, EPT  
Craig Usher, Centraflow

Norwegian University of Science and Technology  
Department of Energy and Process Engineering







EPT-M-2018-62

**MASTER THESIS**

for

Student: Tri Nguyen

Spring 2018

English title:

Displacement of Non-Newtonian Fluids in Annular Spaces

*Norwegian title:**Fortrengning av ikke-newtonske væsker i annulære ringrom***Background and objective**

Cementing jobs in long horizontal wells require optimum displacement of drilling fluid and cuttings, which means basic understanding of flow patterns, frictional pressure losses and mutual interactions of Non-Newtonian fluids in annular spaces, in addition to solid particle – fluid interactions. The study will be a continuation of the autumn 2017- project by the candidate, based largely upon a recent review of state-of-the-art in this field. The fundamental focus should be on fluid mechanics and related computational techniques, with the Newtonian case as point of departure, in particular with regard to the solid particle – fluid interactions which are required for modelling the transport of cuttings. Flow rates and fluid velocity profiles over annular cross-sections are to be studied for concentric and typical eccentric cases for chosen fluids rheology, and displacement efficiency of drilling fluid by standard cement slurry is to be predicted. The main objective of this study is to demonstrate how Computational Fluid Dynamics (CFD) can be a useful tool to identify practical guidelines and solutions to cement displacement challenges in well technology.

**The following tasks are to be considered:**

- 1 Compare velocity profiles for a typical Newtonian fluid with those of a few Non-Newtonian cases in a simple 2D geometry for the same pressure gradient and inlet conditions.
- 2 For standard horizontal well conditions, (as for instance specified in note from C. Usher, Centraflow, March 2017), identify the critical factors which effect fluid flow in different eccentricities in a downhole annulus.
- 3 Make a computation of displacement of a typical drilling fluid by a typical cement slurry, assuming immiscible fluids in the annular space.
- 4 Introduce a cuttings bed at the low-side of the space, and look for a model of displacement by the cement flow.

Within 14 days of receiving the written text on the master thesis, the candidate shall submit a research plan for his project to the department.

When the thesis is evaluated, emphasis is put on processing of the results, and that they are presented in tabular and/or graphic form in a clear manner, and that they are analyzed carefully.

The thesis should be formulated as a research report with summary both in English and Norwegian, conclusion, literature references, table of contents etc. During the preparation of the text, the candidate should make an effort to produce a well-structured and easily readable report. In order to ease the evaluation of the thesis, it is important that the cross-references are correct. In the making of the report, strong emphasis should be placed on both a thorough discussion of the results and an orderly presentation.

The candidate is requested to initiate and keep close contact with his/her academic supervisor(s) throughout the working period. The candidate must follow the rules and regulations of NTNU as well as passive directions given by the Department of Energy and Process Engineering.

Risk assessment of the candidate's work shall be carried out according to the department's procedures. The risk assessment must be documented and included as part of the final report. Events related to the candidate's work adversely affecting the health, safety or security, must be documented and included as part of the final report. If the documentation on risk assessment represents a large number of pages, the full version is to be submitted electronically to the supervisor and an excerpt is included in the report.

Pursuant to "Regulations concerning the supplementary provisions to the technology study program/Master of Science" at NTNU §20, the Department reserves the permission to utilize all the results and data for teaching and research purposes as well as in future publications.

The final report is to be submitted digitally in DAIM. An executive summary of the thesis including title, student's name, supervisor's name, year, department name, and NTNU's logo and name, shall be submitted to the department as a separate pdf file. Based on an agreement with the supervisor, the final report and other material and documents may be given to the supervisor in digital format.

- Work to be done in lab (Water power lab, Fluids engineering lab, Thermal engineering lab)  
 Field work

Department of Energy and Process Engineering, 15. January 2018

  
Tor Ytrehus  
Academic Supervisor

Research Advisor: Reidar Kristoffersen







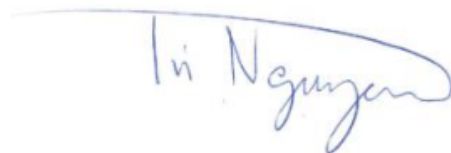
# Preface

---

This master thesis is written as a part of the study program of *Mechanical Engineering* with specialization in *Fluid Engineering*. The thesis was written in the spring of 2018 during the last year of the study of Master of Science at the *Norwegian University of Science and Technology*.

The basis for this thesis stemmed from a collaboration with the company Centraflow, in order to develop a better insight into the world of Computational Fluid Dynamics for product design and analysis. The company develops products for the oil & gas industry and utilize CFD in their product design. The thesis is a continuation of the project work performed fall of 2017.

Trondheim, June 10, 2018



Tri Nguyen





# Acknowledgements

---

I would like to show my profound gratitude to my supervisor, Tor Ytrehus, for providing guidance, help during the project phases and evaluating my work. This has been of great importance during the progression of the work, as well as finalizing the thesis.

I would like to thank my supervisor from Centraflow, Craig Usher, for providing with knowledge, technical insight, a perspective from field operations, and for introducing me to the world of petroleum engineering. I would also thank Nader Behjat and Grant Knight, the CEO, and CTO of Centraflow, which also has contributed with useful information and help on drilling-related topics.

I must also thank Dr. Zhigarev from the Siberian Federal University for providing experimental data and for being open to questions.



# Abstract

---

A successful cement job is determined by the displacement efficiency. Displacement of drilling fluids in horizontal annuli is a critical element in the completion of wellbores. Optimum displacement requires an understanding of flow patterns, frictional pressure losses and mutual interaction of mud, spacers, and cement in annular spaces. Modelling this complex behaviour is difficult, and requires a fundamental understanding of fluid mechanics, rheology, and computational techniques. Nevertheless, it is essential to understand the flow propagation to guarantee displacement success.

A Computational Fluid Dynamics (CFD) model has been developed, and simulations have been performed in order to analyze the operational downhole conditions during primary cementing. The simulations accounted for complexities such as non-Newtonian fluids and eccentricity in annuli for both single-phase and multiphase flow of mud-cement-spacer.

The study identifies the fluid displacement and failure modes associated with fluid displacement due to high eccentricity. For single-phase analysis, the numerical analysis shows  $\pm 5\%$  accuracy compared to experimental data and study of Zhigarev et al. Multiphase simulations show that the studied fluid train of drilling mud-spacer-cement display adequate displacement efficiency. Although, an increase of modelling complexity should be performed in order to obtain more accurate representation. Data acquired from the multiphase simulations should be verified against experimental work, in order to justify the feasibility of the CFD model used for product design and analysis in specific conditions. Overall, a CFD approach for analysis of primary cementing may yield adequate information in order to improve cementing to ensure sufficient zonal isolation, which is necessary for well integrity.

# Sammendrag

---

Vellykket sementering bestemmes av effektiviteten av transport av borefluider. Forskyvning av borefluider i horisontale ringrom er en kritisk faktor for fullføring av brønner. Optimal forskyvning av fluider krever en forståelse av strømningsmønstre, trykktap og gjensidig vekselvirkning av borevæske, spacer, og sement i ringrom. Modellering av denne komplekse oppørselen er av vanskelig, og krever en fundamental forståelse av fluid mekanikk, reologi, og numeriske beregningsteknikker. Likevel er det essensielt å forstå flyttutbredelsen for å garantere væskeforskyvningssuksess.

En numerisk strømningsberegnings-modell (CFD-model) har blitt utviklet og simuleringer har blitt gjennomført for å analysere operasjonsforhold i brønner under primær sementering. Simuleringer har tatt for seg kompleksiteter som ikke-Newtonske væsker og eksentrisitet i ringrom for både en-fase og trefase strømning av borevæske-spacer-cement.

Studien har identifisert væskeforskyvningen og feil moduser av væske forskyvning grunnet høy eksentrisitet. For en-fase analyser har de numeriske resultatene vist en  $\pm 5\%$  nøyaktighet sammenlignet med eksperimentell data og studier utført av Zhigarev et al. (2011). Flerfase simuleringene har vist at borevæske-spacer-sement viser tilstrekkelig forskyvningseffektivitet. Likevel bør en økning av modelleringskompleksiteten bli utført for å få en mer nøyaktig representasjon. Dataen som er tilegnet for flerfase simuleringer burde også bli verifisert mot eksperimentelt arbeid for å rettferdiggjøre CFD-modellen brukt for produktdesign og analyser av spesifikke forhold. Alt i alt er en CFD fremgangsmåte for analyse av primær sementering en effektiv metode for å tilegne seg informasjon for å forbedre sementering og for å sørge for sone-isolasjon, som er nødvendig for brønnintegritet.



# Contents

---

Preface	I
Acknowledgements	III
Abstract	V
Sammendrag	VI
List of Figures	XII
Nomenclature	XVIII
<b>1. Fluid Displacement in Wellbores</b>	<b>1</b>
1. Introduction	2
1.1. Problem description . . . . .	2
1.2. Motivation & Objectives of Research . . . . .	4
1.3. Outline of the Thesis . . . . .	6
2. Background	7
2.1. Primary Well Cementing . . . . .	7
2.2. Fluid Flow and Displacement in the Annulus . . . . .	12
2.2.1. Flow behaviour of Non-Newtonian Fluids . . . . .	15
2.2.2. Effects of Eccentricity . . . . .	17
2.2.3. Modelling Primary Cementing in Annulus . . . . .	20



<b>II. Computational Fluid Dynamics</b>	<b>23</b>
<b>3. Fluid Dynamics &amp; Flow Modelling</b>	<b>24</b>
3.1. Rheological Model Application for Viscous Term . . . . .	24
3.2. Multiphase Flow . . . . .	29
3.2.1. Physics of Multiphase flows . . . . .	30
3.2.2. Modelling approach . . . . .	30
3.2.3. Volume-of-Fluid Method . . . . .	32
3.3. General Transport Equation . . . . .	36
<b>4. Assessment of CFD Implementation</b>	<b>38</b>
4.1. Differencing Schemes . . . . .	39
4.1.1. Assessment of Upwind Discretization Scheme . . . . .	39
4.1.2. Properties of Discretization Schemes . . . . .	42
4.2. Discretization of Transport Equations . . . . .	45
4.2.1. Discretization of the Continuity Equation . . . . .	45
4.2.2. Discretization of the Momentum Equation . . . . .	46
4.2.3. Differencing Schemes Employed in the Transport Equation . . . . .	47
4.2.4. Spatial Discretization: Gradient . . . . .	47
4.2.5. Spatial Discretization: Pressure & Momentum . . . . .	49
4.2.6. Explicit Scheme: Volume Fraction . . . . .	50
4.3. Solution of 3D Convection-Diffusion Problems with FVM . . . . .	51
4.4. Implementation of Boundary Conditions . . . . .	55
4.4.1. Best-Practise CFD Implementation of Boundary Conditions . . . . .	61
4.5. Solution of System of Equations . . . . .	63
4.6. Solution of Discretized Equations . . . . .	65
4.7. Solver-Algorithms for Pressure-Velocity Coupling . . . . .	69
4.7.1. Pressure-Velocity Coupling . . . . .	69
4.7.2. SIMPLE Algorithm . . . . .	71
<b>5. Computational Domain</b>	<b>74</b>
5.1. Grid Structure . . . . .	74

5.2. Mesh Metric and Mesh Quality . . . . .	77
5.3. Grid Generation . . . . .	80
5.3.1. Data Structure of the Mesh . . . . .	84
5.3.2. Data Structure of ANSYS Fluent . . . . .	85
<b>III. Simulations &amp; Case Studies</b>	<b>88</b>
<b>6. Single-phase Flow Modelling</b>	<b>89</b>
6.1. Model Validation: Single-Phase . . . . .	89
6.2. Model Validation: Mesh Independence . . . . .	93
6.3. Single-phase: Eccentricity Analysis . . . . .	94
6.3.1. Solver Settings . . . . .	99
6.3.2. Schematic of present CFD set-up . . . . .	101
6.3.3. Results . . . . .	102
6.3.4. Assessment of Pressures in Annuli with Correlated Models . . . . .	109
6.3.5. Effects of Eccentricity . . . . .	111
6.3.6. Assessment of Herschel-Bulkley Modelling of Non-Newtonian Flow . . . . .	112
<b>7. Multiphase Flow Modelling</b>	<b>114</b>
7.1. Multiphase: Drilling Mud, Spacer & Cement . . . . .	114
7.1.1. Solver Settings . . . . .	119
7.1.2. Schematic of present CFD set-up . . . . .	120
7.1.3. Results . . . . .	121
7.1.4. Displacement Efficiency . . . . .	126
<b>8. Conclusion</b>	<b>129</b>
<b>A. Appendix</b>	<b>137</b>
A.1. Rheology Analysis . . . . .	137
A.2. Mesh Settings and Mesh Statistics . . . . .	141
A.2.1. Single-Phase - Eccentricity Case . . . . .	141
A.2.2. Multiphase - Three-phase Case . . . . .	143
A.3. Results - Eccentricity Cases: Pressure & Velocity Development . . . . .	144

A.4. Results - Eccentricity Cases: Velocity Profiles . . . . .	148
A.5. Results: Residuals . . . . .	151
A.6. CFD Implementation . . . . .	156
A.6.1. Schematic of Approach for problem solving with CFD . . . . .	156
A.6.2. Schematic of CFD Flowchart for Fluent . . . . .	157
A.6.3. Schematic of Solver . . . . .	158
A.7. Fundamentals of Fluid Dynamics . . . . .	159
A.7.1. Mass Conservation of a Fluid Element . . . . .	159
A.7.2. Momentum Equation in Three-Dimensions . . . . .	161
A.7.3. Equations of State . . . . .	163
A.7.4. Navier-Stokes Equations for Fluid Flow . . . . .	164

# List of Figures

---

1.1. Settlement of cuttings during horizontal drilling (Courtesy of Centraflow). . . .	2
1.2. Inadequate cementing due to the presence of cuttings in the wellbore (Courtesy of Centraflow). . . . .	3
1.3. The flow diverter product, CE-BOND. . . . .	5
1.4. Flow visualization for streamlines past CE-BOND in an eccentric annulus. . . .	5
2.1. An illustration of the most common drill bit, polycrystalline diamond compact (PDC), drilling through formations [1]. . . . .	8
2.2. Downhole pressure modes.[2] . . . . .	9
2.3. Drilling windows during drilling operations [2]. . . . .	10
2.4. An illustration of cement flow in the annulus through the various formations [3].	11
2.5. Example of a recommended fluid train for WBM drilling. . . . .	13
2.6. Displacement of mud-spacer-cement for primary cementing [4]. . . . .	15
2.7. Correlated data of fluids with the Reynolds number model plotted against friction factor, Madlener et al. (2009). . . . .	17
2.8. An annulus defined with variables which decides degree of eccentricity. . . . .	18
2.9. Correlation factor vs. eccentricity for a annulus with pipe ratio of 0.7 (Hacislamoglu & Langlinais) [5]. . . . .	19
2.10. Rheology analysis for Herschel-Bulkley model performed by Peng. et. al. (2013) [6]. . . . .	20
2.11. A presentative plot from the study Zulqarnain & Tyagi (2016), describing a displacement plot [7]. . . . .	21

3.1. Four time-independent fluids presented [8]. . . . .	27
3.2. An illustration of different velocity regions for three type of fluids in eccentric annuli [9]. . . . .	28
3.3. Example of gas-liquid flow for different multiphase flow regimes [10]. . . . .	30
3.4. Interface calculations for geometric reconstruction and the donor-acceptor scheme to represent the actual interface [11]. . . . .	32
3.5. An illustration of interface between two fluid and showing the normal-vector [12]. . . . .	34
4.1. Stencils for first- and second-order upwind considered in the x-direction. . . .	40
4.2. An illustration of CV evaluation for gradients and scalar value consideration. .	47
4.3. An illustration of cell-center evaluation for least-square cell-based gradient. . .	48
4.4. Stencil for 2D & 3D FVM. . . . .	51
4.5. Grid arrangement at boundaries, where the dotted lines represents the boundaries for the cells. . . . .	56
4.6. $u$ - and $v$ -velocities at the inlet boundary . . . . .	57
4.7. Pressure correction cell and scalar cell at inlet boundary. . . . .	58
4.8. $u$ - and $v$ -velocities at the outlet boundary. . . . .	58
4.9. Pressure correction cell and scalar cell at outlet boundary. . . . .	59
4.10. $u$ - and $v$ -velocities at the wall boundary. . . . .	60
4.11. Pressure correction cell and scalar cell at wall boundary. . . . .	60
4.12. Numerical diffusion for the classical example on flow with misaligned grid, for first- and second-order upwind [13]. . . . .	70
4.13. Presentation of the staggered grid concept introduced by Harlow & Welch (1965) [14]. . . . .	70
4.14. Schematic of the modified solver process for SIMPLE. . . . .	73
5.1. Classifications of grids. . . . .	75
5.2. Mesh Terminology for 2D and 3D mesh. . . . .	76
5.3. Mesh resolution comparison of convergence rate for the well-known lid driven cavity [15]. . . . .	82
5.4. Outline of the various grid generation algorithms [16][17]. . . . .	83

5.5. Triangular cell with node, face volume. . . . .	84
5.6. Grid generation of a 2D rectangular domain with tri-cells with highlighted faces.	85
5.7. Node information extracted from the .msh-file. . . . .	86
5.8. Face information extracted from .msh-file. . . . .	87
5.9. Cell information extracted from the .msh-file. . . . .	87
5.10. User-defined information extracted from the .msh-file. . . . .	87
6.1. Generated mesh for a concentric case. . . . .	90
6.2. The flow domain of annular flow problems. . . . .	90
6.3. Pressure drop for simulated and experimental data for the different mud vary- ing with mass flow compared with Zhigarev (2011). . . . .	91
6.4. Computed vs. measure pressure drop for results from the present CFD simula- tions, as well as that of Zhigarev (2011). . . . .	91
6.5. The effects of eccentricity of the pressure drop shows agreement with the ex- perimental data for both Zhigarev (2011) and the performed simulations. . . . .	92
6.6. The results from the eccentricity study shows that the model shows a low de- gree of deviation from the experiments. . . . .	92
6.7. Mesh independence study performed, where pressure drop vs. number of cells is computed. . . . .	93
6.8. An example of generated mesh, here visualized for the 0.5 eccentricity case. . . . .	97
6.9. An illustration of the modelling domain for CFD analysis. . . . .	98
6.10. Schematic of CFD set-up in <i>Fluent</i> for performing single-phase simulations. . . . .	101
6.11. Illustration of the effect of eccentricity yielding improper cement displacement.	102
6.12. Comparison of Newtonian and Non-Newtonian ( <i>Herschel-Bulkley Model</i> with eccentricity = 0, visualized with a 3D velocity plot. . . . .	103
6.13. Comparison of Newtonian and Non-Newtonian ( <i>Herschel-Bulkley Model</i> with eccentricity = 0, visualized with a 2D velocity plot. . . . .	103
6.14. Comparison of Newtonian and Non-Newtonian ( <i>Herschel-Bulkley Model</i> with eccentricity = 0.25, visualized with a 3D velocity plot. . . . .	104
6.15. Comparison of Newtonian and Non-Newtonian <i>Herschel-Bulkley Model</i> with eccentricity = 0.25, visualized with a 2D velocity plot. . . . .	104

6.16. Comparison of Newtonian and Non-Newtonian ( <i>Herschel-Bulkley Model</i> with eccentricity = 0.50, visualized with a 3D velocity plot. . . . .	105
6.17. Comparison of Newtonian and Non-Newtonian ( <i>Herschel-Bulkley Model</i> with eccentricity = 0.50, visualized with a 2D velocity plot. . . . .	105
6.18. Comparison of Newtonian and Non-Newtonian ( <i>Herschel-Bulkley Model</i> with eccentricity = 0.75, visualized with a 3D velocity plot. . . . .	106
6.19. Comparison of Newtonian and Non-Newtonian ( <i>Herschel-Bulkley Model</i> with eccentricity = 0.75, visualized with a 2D velocity plot. . . . .	106
6.20. Comparison of Newtonian and Non-Newtonian ( <i>Herschel-Bulkley Model</i> with eccentricity = 1, visualized with a 3D velocity plot. . . . .	107
6.21. Comparison of Newtonian and Non-Newtonian ( <i>Herschel-Bulkley Model</i> with eccentricity = 1, visualized with a 2D velocity plot. . . . .	107
6.22. Simulation results for pressure drop [Pa/m] for the various eccentricity cases. .	108
6.23. Comparison of pressure drop computed from the present CFD simulations vs. eccentricity for Newtonian rheology model with correlation from the work of Hacıislamoglu & Langlinais (1990) and Madlener et. al.(2009). . . . .	109
6.24. Comparison of pressure drop computed from the present CFD simulations vs. eccentricity for non-Newtonian <i>Herschel-Bulkley</i> rheology model with correlation from the work of Hacıislamoglu & Langlinais (1990) and Madlener et. al.(2009). . . . .	110
7.1. Rendering of CAD representation of the geometry for multiphase cases. . . . .	116
7.2. The generated structured hex-mesh for the multiphase cases. . . . .	117
7.3. Schematic of CFD set-up in <i>Fluent</i> for performing three-phase simulations. . .	120
7.4. Inflow of mud, spacer and cement vs. elapsed time. . . . .	121
7.5. Outflow of mud, spacer and cement vs. elapsed time. . . . .	121
7.6. Displacement of mud, spacer and cement vs. elapsed time. . . . .	122
7.7. Displacement of mud by spacer for the elapsed solution time for a section of the annulus. . . . .	123
7.8. Displacement of spacer by cement for the elapsed solution time for a section in the annulus. . . . .	125

7.9. Results from one of the cases performed by Zulqarnain & Tyagi for mud-spacer-cement analysis showing instabilities. . . . .	127
A.1. Strain rate vs. shear stress plot for the drilling fluids for Oswald de Waele model for the validation case. . . . .	137
A.2. Rheology analysis performed for cement (9-5/8" Tail Slag, viscometer data by <i>Schlumberger</i> ). . . . .	138
A.3. Rheology analysis performed for WBM (viscometer data by MI-Swaco). . . . .	139
A.4. Rheology analysis performed for Spacer (Spacer-Mudpush II, viscometer data by <i>Schlumberger</i> .) . . . . .	140
A.5. Comparison of pressure development for the eccentricity = 0 cases. . . . .	144
A.6. Comparison of velocity development for the eccentricity = 0 cases. . . . .	144
A.8. Comparison of velocity development for the eccentricity = 0.25 cases. . . . .	144
A.7. Comparison of pressure development for the eccentricity = 0.25 cases. . . . .	145
A.9. Comparison of pressure development for the eccentricity = 0.5 cases. . . . .	145
A.10. Comparison of velocity development for the eccentricity = 0.5 cases. . . . .	145
A.11. Comparison of pressure development for the eccentricity = 0.75 cases. . . . .	146
A.12. Comparison of velocity development for the eccentricity = 0.75 cases. . . . .	146
A.13. Comparison of pressure development for the eccentricity = 1 cases. . . . .	146
A.14. Comparison of velocity development for the eccentricity = 1 cases for. . . . .	147
A.15. Comparison of velocity profiles for the eccentricity cases between Newtonian and Herschel-Bulkley rheology modelling for eccentricity=0. . . . .	148
A.16. Comparison of velocity profiles for the eccentricity cases between Newtonian and Herschel-Bulkley rheology modelling for eccentricity=0.25. . . . .	149
A.17. Comparison of velocity profiles for the eccentricity cases between Newtonian and Herschel-Bulkley rheology modelling for eccentricity=0.5. . . . .	149
A.18. Comparison of velocity profiles for the eccentricity cases between Newtonian and Herschel-Bulkley rheology modelling for eccentricity=0.75. . . . .	150
A.19. Comparison of velocity profiles for the eccentricity cases between Newtonian and Herschel-Bulkley rheology modelling for eccentricity=1. . . . .	150
A.20. Residuals for simulation of Newtonian model with 0 eccentricity. . . . .	151



A.21.Residuals for simulation of Newtonian model with 0.25 eccentricity. . . . .	151
A.22.Residuals for simulation of Newtonian model with 0.50 eccentricity. . . . .	152
A.23.Residuals for simulation of Newtonian model with 0.75 eccentricity. . . . .	152
A.24.Residuals for simulation of Newtonian model with 1 eccentricity. . . . .	153
A.25.Residuals for simulation of Herschel-Bulkley model with 0 eccentricity. . . . .	153
A.26.Residuals for simulation of Herschel-Bulkley model with 0.25 eccentricity. . . .	154
A.27.Residuals for simulation of Herschel-Bulkley model with 0.50 eccentricity. . . .	154
A.28.Residuals for simulation of Herschel-Bulkley model with 0.75 eccentricity. . . .	155
A.29.Residuals for simulation of Herschel-Bulkley model with 1 eccentricity. . . . .	155
A.30.Schematic of the general algorithm using CFD. . . . .	156
A.31.Schematic of the complete process in <i>Fluent</i> for solving CFD problems. . . . .	157
A.32.Schematic of the modified solver process for SIMPLE. . . . .	158
A.33.Fluid element for Conservations laws . . . . .	159
A.34.Mass flows in and out of a fluid element. . . . .	160
A.35.Stress components in a fluid element . . . . .	162

# Nomenclature

---

## **Abbreviations**

BHP Bottom-hole pressure

BPM Barrels per minute

CAD Computer aided design

CAE Computer aided engineering

CFD Computational fluid dynamics

ECD Equivalent circulating density

FDM Finite difference method

FVM Finite volume method

HP-HT High pressure - high temperature

LPM Liters per minute

OBM Oil-based mud

ROP Rate of penetration

TVD True vertical depth

WBM Water-based mud

WOC Waiting on cement

### **Mathematical Expressions**

$\delta$  Kronecker delta

$\dot{\gamma}$  Strain rate

$\eta$  Viscosity

$\eta_e$  Effective viscosity

$\Gamma$  Diffusion coefficient

$\mu$  Dynamic viscosity

$\phi$  General variable for transport property

$\rho$  Density

$\tau$  Shear stress

$\tau_0$  Yield shear stress

$\tau_e$  Effective shear stress

$K$  Consistency index

$n$  Flow index parameter

### **CFD Technical Terms**

$\alpha$  Relaxation Factor

AMG Algebraic multigrid

CFL Courant-Friedrichs-Lewy

CV Control volume

DNS Direct numerical simulation

OQ Orthogonal quality

Pe Peclet number

Re Reynolds number

SIMPLE Semi-implicit method for pressure-linked equations

URF Under relaxation factor

VOF Volume-Of-Fluid

## Part I.

# Fluid Displacement in Wellbores

# Introduction

---

## 1.1. Problem description

For completion of wells, the main purpose of cementing operations is to provide zonal isolation and provide well-integrity. A key factor determining successful cementing is an adequate removal of drilling fluid. Effective displacement of drilling mud is an important element to ensure sufficient cuttings transportation during drilling operations, and consequently provide a successful cement job in a wellbore. To establish optimal mud removal, the main technique is to displace the drilling mud with a spacer fluid. The spacer has modified rheological characteristics designed for a favourable mud-to-spacer and spacer-to-cement interaction to enhance the fluid displacement. For many cases, it is desirable to monitor how this interface evolves in time. However, an improper displacement of spacer and mud may lead to contamination during the cementing. The contamination of drilling muds or spacer fluids in the cement, can have unfavourable effects during cement settlement and consequently, a significant increase in costs due to the requirement of remedial repair of the

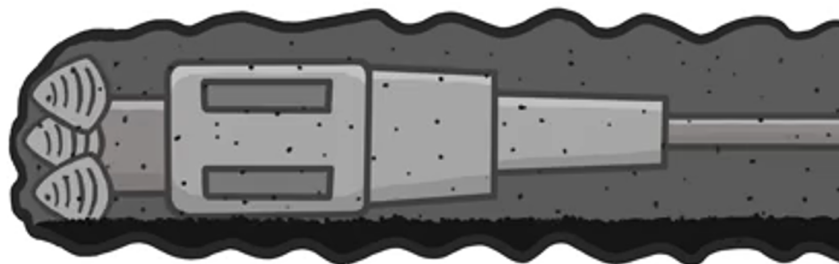


Figure 1.1.: Settlement of cuttings during horizontal drilling (Courtesy of Centraflow).

inadequate cemented wellbore.

Other factors that impact the mud displacement is the wellbore geometry, mud conditioning, drill string movement, casing centralization and optimal pump operations [18]. Yet, it is often the lack of information to which these variables affect the displacement of drilling fluids, especially when these complexities are combined. An assumed simple displacement operation can evolve into a challenging scenario when the variables are increased. The oil & gas industry has performed numerous studies in this area over the last centuries to evaluate the importance of these parameters and their effect on displacement efficiency [19].

Despite the number of theoretical, numerical and experimental research devoted to drilling fluids in wellbores, it is difficult to give a complete description of flow characteristics in the wellbore for a wide range of drilling operational parameters. In practice, annular flow increases in complexity due to the presence of eccentricity in annuli, as well as rotation and reciprocation. Moreover, the drilling fluids applied for drilling operations exhibit non-Newtonian behaviour. In general, no exact analytic solution can describe this intricate flow which is complex by nature. Since a well-described solution does not exist, this is still actively studied.



Figure 1.2.: Inadequate cementing due to the presence of cuttings in the wellbore (Courtesy of Centraflow).

### 1.2. Motivation & Objectives of Research

The thesis is developed from a collaboration with the oil & gas company, *Centraflow*. With the defined problem description stated previously, Centraflow has developed and designed down-hole products which aim to improve the fluid displacement. The main series of products, namely CE-BOND, have the ability to divert the flow such that fluid displacement is desirable in different modes during the drilling operations. These modes can be fluid displacement and cuttings transportation in deviated and horizontal wellbores, drill-string eccentricity due to gravity forces, and all aspects related to pumping of various fluids related to primary cementing.

The basis of the product comes from a patented flow-diversion design, where models have been designed in CAD environment, analyzed and optimized with CFD as a design tool, and validated with flow loop tests. The following study emphasizes on the CFD modelling enforced to provide a multi-purpose model for flow analysis and design optimization. This thesis is a continuation of the project work performed in the fall of 2017.

The scope for this thesis will be on the following focus areas:

- Laminar flow behaviour of non-Newtonian fluids
- Rheological analysis of non-Newtonian fluids
- Assessment of CFD tools in the CFD-software, *Fluent*
- Assessment of CFD implementation in *Fluent*
- Development of CFD model for non-Newtonian fluids
- Analysis of the effect of eccentricity for single-phase flow
- Analysis of the displacement efficiency for three-phase flow
- Propose suggestions for improvement of primary cementing in well operations

The thesis aims to increase the knowledge of fluids exhibiting non-Newtonian behaviour in annular flow, determining important flow characteristics such as pressure losses and velocity profile in annuli. It can be noted that flow regimes in the transition to turbulent and fully turbulent flow, as well as modelling of cuttings transportation with the non-Newtonian flu-



ids, are not considered. Only operational conditions regarding the pumping of fluid trains in annuli are of interest.



Figure 1.3.: The flow diverter product, CE-BOND.

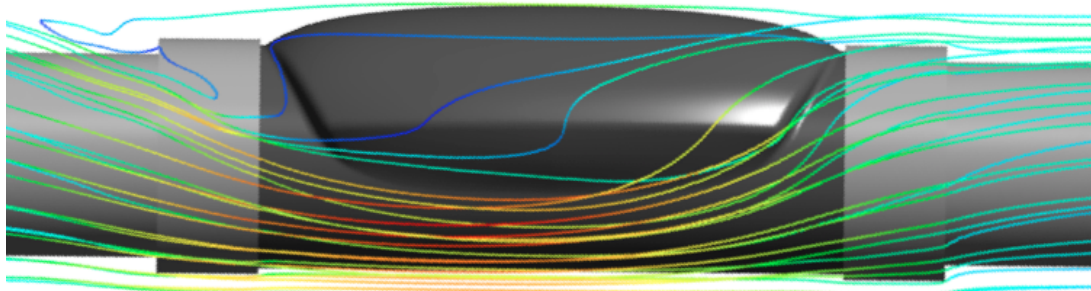


Figure 1.4.: Flow visualization for streamlines past CE-BOND in an eccentric annulus.

## 1.3. Outline of the Thesis

In the following, an outline of the structure of the thesis is presented.

### **Part I: Fluid Displacement in Wellbores**

The following chapter contains a background description of fluid displacement, with emphasis on primary cementing and the drilling problems related to the aspect of petroleum engineering, respectively.

### **Part II: Computational Fluid Dynamics**

Chapter 3 highlights the governing equations of the fluid dynamics and models used. Chapter 4 provides an assessment of CFD implementation and the techniques utilized in the CFD model. Chapter 5 presents the knowledge behind computational domain, such as grid structure and grid generation for CFD analysis.

### **Part III: Simulations & Case Studies**

Chapter 7 presents the results of the CFD analysis performed. Lastly, Chapter 8 provides a conclusion of the study.

# Background

---

For sub-surface operations, drilling and cementing of wells is the most critical component for well completion. For various well architecture and constructions, the structure must satisfy extreme criteria of robustness. The process of drilling and cementing is referred to as *primary cementing*, and is the well completion process which is the main focus areas of this thesis.

## 2.1. Primary Well Cementing

### Drilling of Wells

The process of drilling is essentially having a drill bit attached to a drill string, cutting into the Earth by mechanical actions of shear and cutting forces. During drilling operations, the fragmented rock, referred to as cuttings, is transported by drilling muds to the surface for collection. The drilling mud is pumped through nozzles on the drill bit and has various other applications, such as providing cooling, lubrication, etc. The drilling mud is pumped into the wellbore and transports the cuttings through the annulus between the drilling string and wellbore, illustrated in Fig. 2.1. When the drilling fluids reach the surface, the cuttings are filtered out by systems called *shakers*, and then pumped back down to the well.

### Downhole Pressures

An important function of drilling mud is to control the pressure inside the well during drilling. The drilling mud forms a column inside the wellbore, exerting hydrostatic pressure to the

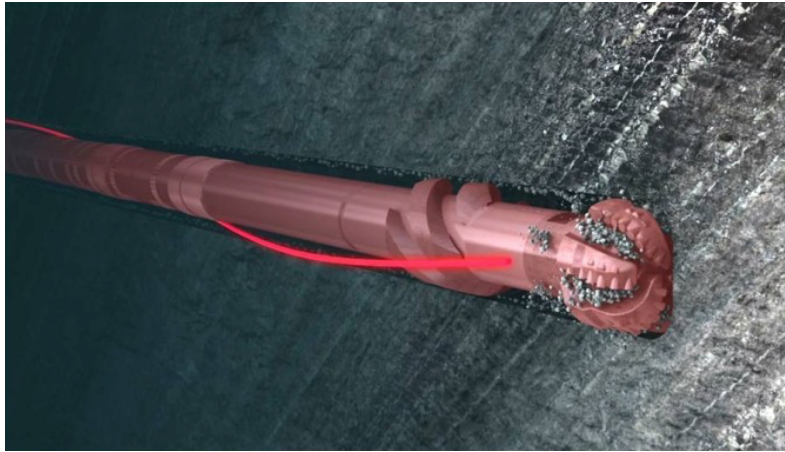


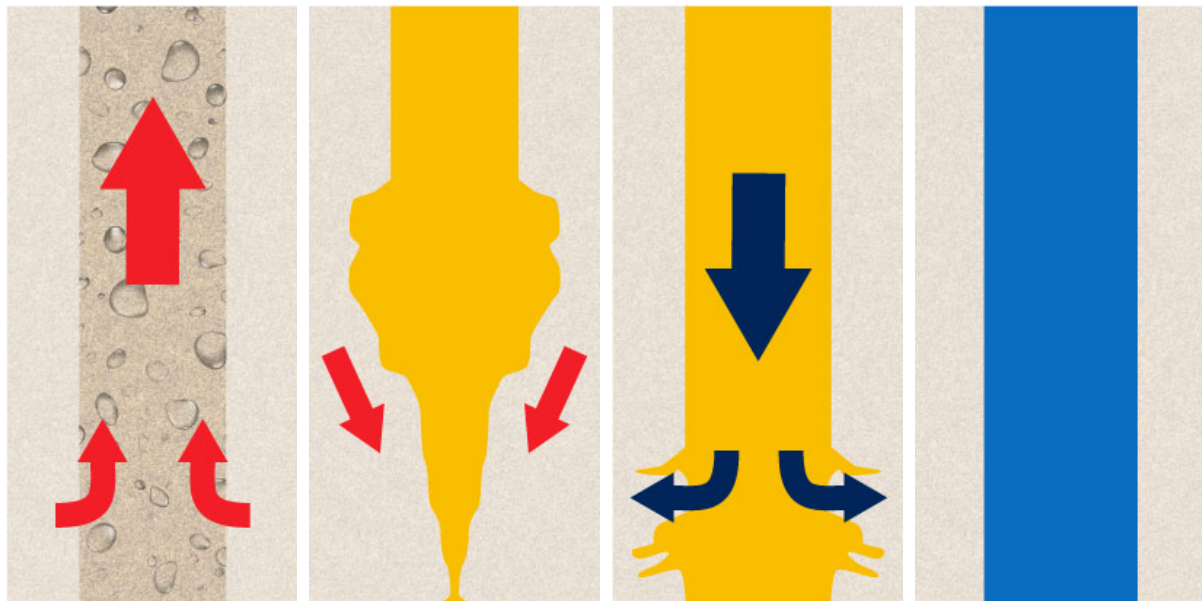
Figure 2.1.: An illustration of the most common drill bit, polycrystalline diamond compact (PDC), drilling through formations [1].

formation preventing the well from collapsing. The properties of the drilling mud can be varied by changing the density with various weighting-agents.

The pressure exerted by the fluid column must be lower than the pressure causing the formations to fracture and higher than the pressure caused by the fluids in the rock. This is commonly known as the *drilling window*, seen in Fig. 2.3a. For drilling operations, the drilling window highly dictates the drilling progression and the quality of the well integrity.

There exist four different downhole pressure modes of importance. *Formation pressure*, or *pore pressure*, refers to the pressure of hydrocarbons within the pores of a reservoir. The wellbore pressures must exceed the pore pressure to prevent leakage into the annulus during drilling. *Break-out pressure*, which is the pressure at which stress-induced enlargements occurs in the wellbore. This limit occurs when the pressure exerted by the fluid column is too low and does not fully support the surrounding formation. *Fracture pressure*, also known as the *breakdown pressure*, is the pressure at which the formation will break due to excessive pressures exerted by the fluids. This leads to cracks and pockets which allow fluids to flow inside. The final downhole pressure mode is the *hydrostatic pressure*. This is the pressure of fluids present in reservoirs. The pressure is exerted by the fluid column from a depth of reservoir onto the formations. All four modes can be seen in Fig. 2.2.

In order to maintain proper progression whilst maintaining the drilling window, different wellbore sizes are drilled with its corresponding casings. There exist standards of drilling



(a) Pore pressure. (b) Break-out pressure. (c) Fracture pressure. (d) Hydrostatic pressure.

Figure 2.2.: Downhole pressure modes.[2]

convention, dictating sizes of the wellbore and casings. This can be modified if drilling in a complex environment and narrow pressure windows are needed. This is done by cementing sections in the wellbore, and consequently maintaining, or saving, progress. Cementing is performed when the pore pressure gradient at the bottom-hole excess the fracture pressure in the wellbore. A casing-string transported down the well while the drill-string is replaced with string for pumping fluids [20].

### Cementing Process and Functions

For drilling operations to take place, the process of transporting cement slurry into the wellbore is referred to as the cementing process. The aim is to fill the annular space between the casing string and wellbore with cement, providing a seal and mechanical structure supporting the casing for operational procedures.

The purpose of the cementing process is to displace the cement slurry throughout the annulus, creating a bonding between the casing and the formation. Conventional methods involve pumping cement down the casing and displacing it around the casing shoe into the annulus. This also creates a zonal isolation in the wellbore. Zonal isolation is defined as isolating one zone from another, preventing cross flow and contamination between the dif-

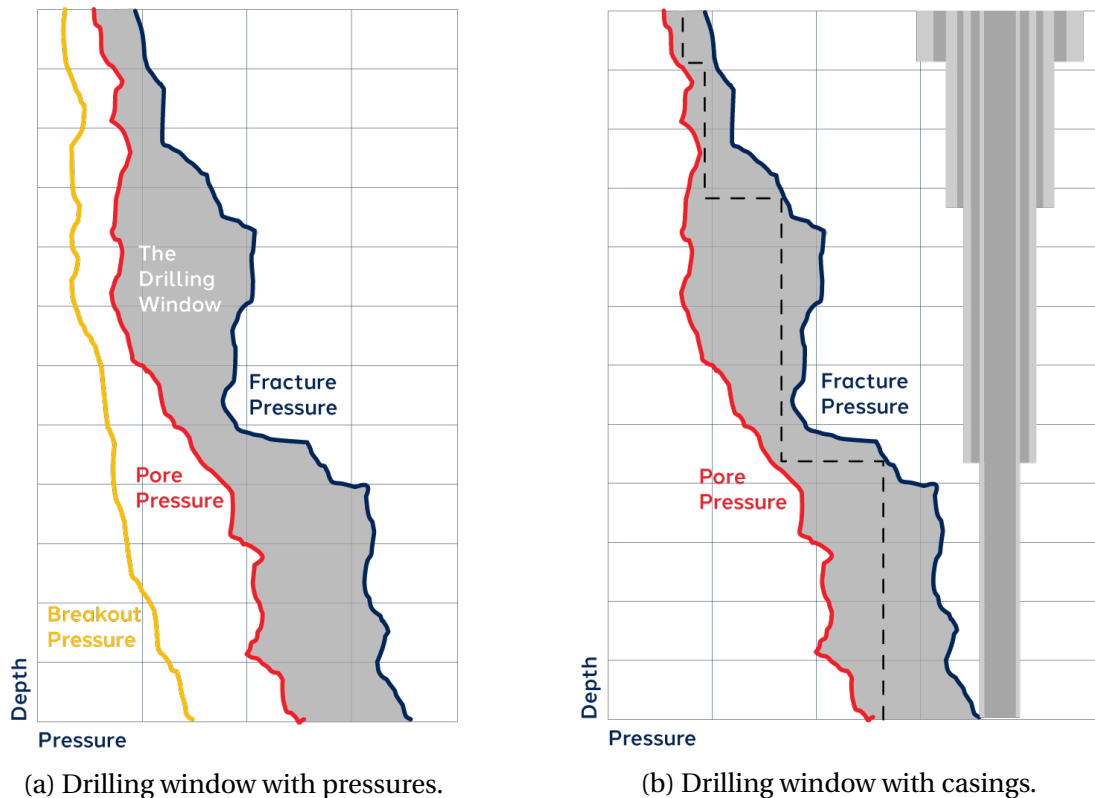


Figure 2.3.: Drilling windows during drilling operations [2].

ferent zones in the casing. Different zones can, for example, be between two different casing sizes, defined by the well schematics. Overall, a proper cement job is essential for further drilling, and for the production of any reservoir operations to take place.

The most important functions of a primary cementing can be represented in the following [20]:

- Provide zonal isolation
- Prevent movement of fluids between formations
- Provide structural integrity and protection of casing
- Provide isolation of the casing from corrosive fluids from the formation
- Seal off lost circulation zones
- Seal off leaks
- Provide a temporary plug
- Provide a permanent plug (Plug & Abandonment)

There also exists mechanical requirements for the cement which mainly provide adequate

compressive strength and low permeability during hardening of the cement slurry. This is especially important for geothermal wells. The most critical factor is to perform a satisfactory cement job to prevent channeling.



Figure 2.4.: An illustration of cement flow in the annulus through the various formations [3].

### Cementing Modes

*Primary cementing* is the technique of displacing cement in annular spaces between the casing and the borehole. The counter-part of primary cementing is *squeeze* or *remedial cementing*. This is the process of repairing a primary cement job or the process which falls outside of primary cementing. Remedial cementing is the process of applying pump pressure to inject cement into problematic void spaces at a desired location in the well. To remedy any faulty primary cementing procedure to make sure that the criteria described previously in the list. 2.1 are fulfilled. Remedial cementing can be performed any time during the life of the well, being during drilling operations, well-completion or production phase. The techniques used involve forcing cement through perforations in the casing, created by a specialized tool, to pump it into the problematic void spaces.

### 2.2. Fluid Flow and Displacement in the Annulus

During the process of primary cementing, a sequence of different fluids is pumped down the well into the annulus, in order to displace drilling mud and prepare the wellbore for cementing. The effects due to eccentricity, breakouts, and irregular cross-sections in wellbores have a significant impact on displacement efficiency. Moreover, it is shown that break-outs in the wellbore may have a substantial negative effect on displacement efficiency, due to that the displaced fluid might flow only into the break-out regions [20]. The effect of channelization is proved to be present if the wellbore geometry is irregular, even if wash-outs and break-outs are not present. Channelization may be effectively prevented by increasing the yield stress of the displacing fluid. The failure modes which is of interest for this study is to be discussed.

#### Mud Conditioning

Before the cementing procedure can commence, a sequence of fluids is pumped into the wellbore in order to displace the drilling mud and prepare the annulus for cement placement. The first process is to circulate all cuttings to the surface with the drilling mud. Thereafter, the drill string is removed out of the well while circulating drilling mud to maintain hydrostatic pressures in the pressure windows. The process of circulating mud is called *mud conditioning*, and has also the purpose of removing all gas and solids and removal of filter-cake. The mud conditioning is carried out as long as it takes to remove all solids and gelled mud from the annulus [21]. During the entire process, the well is continuously logged to obtain a full overview of the well conditions.

Another important aspect of proper mud conditioning is to replace the heavier and viscous fluids used while drilling, with a fluid with less density and viscous properties which are easier to displace during cementing. Ensuring that solids are not present near the wellbore walls, will increase the possibility of better cementing. However, when conditioning with a thinner mud, it is important to not inhibit its ability to hold weighting agents and solids in suspension and circulation with the highest allowable flow rate is recommended, according to current practices [22].



## Preflushing

When the wellbore is prepared with mud conditioning, fluids known as *preflushes* are injected into the well. The preflush fluids are commonly called spacer fluids. The spacer has to satisfy a set of requirements, preparing for cementing (Sauer, 1987, Nelson & Guillot 2006):

- Wetting the casing and wellbore walls for improved bonding of cement
- Sufficient contact-time with the surfaces for improved bonding
- Pumped with high allowable flow rate for efficient mud removal
- Ensure efficient mud displacement
- Rheology-compatible with the cement for improved displacement

All of these criteria must fulfill general requirements, such as maintaining in the drilling window. For example, spacer fluids must not be pumped at rates which can lead to fracture pressure. For industry practices, the effect of preflushing regarding contact-time recommends 10 minutes. According to Nelson & Guillot, contact-time of 4, 5 or 8 minutes of spacer exposure in the wellbore are recommended. For shorter contact-times, the spacers should be pumped in the turbulent flow regime, for increased hole-cleaning efficiency.

The purpose of a spacer is mainly to separate immiscible fluids and displacing drilling mud and solids from the wellbore. In order to prevent sedimentation of solids, viscosifiers are used as a major part of the spacer composition.

Main benefits of utilizing washes, is the increase of hole-cleaning capability, for both flow regimes of turbulent and laminar flow. However, when the circulation process is stopped, the risk of influx of formation-fluid is increased, due to the low density of the washers. The

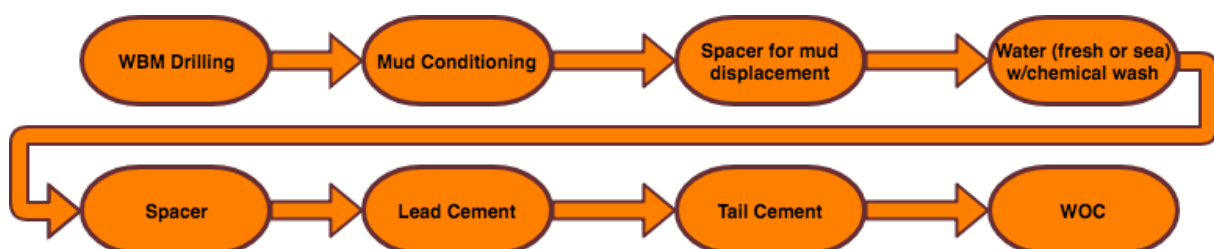


Figure 2.5.: Example of a recommended fluid train for WBM drilling.

pumping schedule should be planned such that the pressures in the wellbores are maintained in the pressure window.

To resolve this issue, the spacer fluids needs weighting in order to increase BHP and thus prevent borehole instabilities. According to the work of Sauer (1997), the spacer should be  $60 \text{ kg/m}^3$  heavier than the drilling mud. Similarly, Khalilova et al. suggest spacers to optimally be 10 % heavier, then the mud [23]. The commonly used weighting agents introduced in the spacer are barite, hematite and calcium carbonate.

In addition to improving hole-cleaning efficiency, the weighting of the spacer means increasing the fluid density. Consequently, BHP will increase which results in an increase of risk for formation fracture. This must be accounted for when designing the spacer, as well as having control of flow rates and pressure windows.

### **Importance of Fluid Displacement**

The process of displacement of fluids in the wellbore during primary cementing are key factors which determine the structural integrity of the cement. Consequently, this highly affects the lifetime of the well for production, as well as after the well is abandoned. If drilling mud is to be left in the annulus, this may lead to failure modes, well control issues, and as a result, economic and environmental impacts associated with cementing failure.

An ideal primary cementing operation implies that all fluids and solids are removed from the wellbore, replaced entirely by cement. However, this is rarely achievable, due to the possibility of undisplaced fluids and solids, which may remain in wash-out areas and other geometrical irregularities in the wellbore.

Main contributors which affect the fluid flow and displacement during primary cementing are:

- Wellbore geometry (wash-outs, break-outs)
- Eccentricity
- Rheology of fluids
- Density of fluids

- Operational conditions (Flow rate, pumping time)
- Well inclination
- Flow regime
- Circulation losses
- Fluid losses leaking into the formation

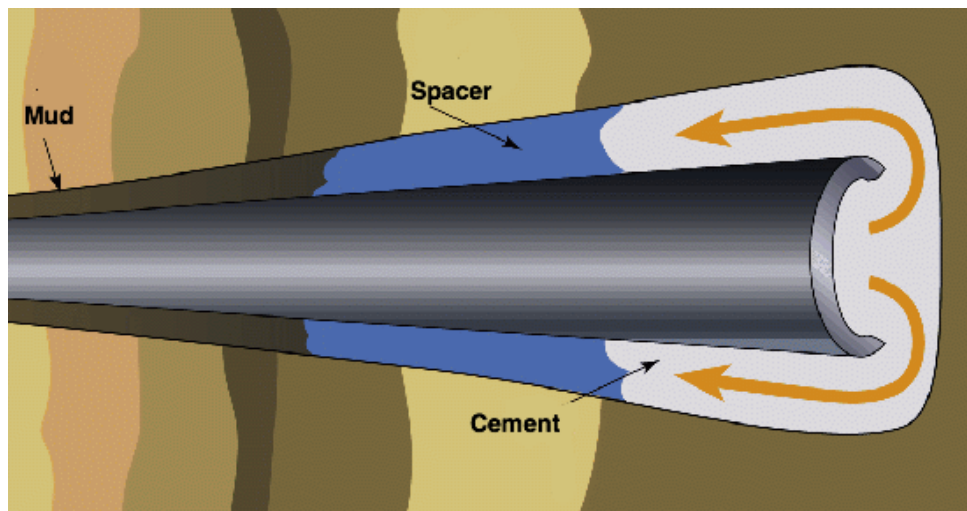


Figure 2.6.: Displacement of mud-spacer-cement for primary cementing [4].

### 2.2.1. Flow behaviour of Non-Newtonian Fluids

In the literature, there are extensive studies performed for analysis of the flow behaviour of Non-Newtonian flow. Some of the most notable is the work by Metzner & Reed (1955). A thorough study was conducted in order to obtain a correlated representation of the friction factor for flow analysis of annular flow. One of the key results was a representation of the Reynolds number derived from an analytical point-of-view in conjunction with rheological parameters, to use for computation of frictional pressure losses [24]. In recent times, Madlener et. al. (2009) derived an extended version of the generalized Reynolds number for flow analysis of non-Newtonian fluids, based on Metzner & Reed's formulation, where the Herschel & Bulkley model was at the focus for gelled fluids [25]. This resulted in a general representation of the Reynolds number available for a range of non-Newtonian fluids

expressed as:

$$Re_{GenHBE} = \frac{\rho u_m^{2-n} D^n}{\left( \frac{\tau_0}{8} \left( \frac{D}{u_m} \right)^n + K \left( \frac{3m+1}{4m} \right)^n 8^{n-1} + \eta_\infty \frac{3m+1}{4m} \left( \frac{D}{u_m} \right)^{n-1} \right)} \quad (2.1)$$

, where

$$m = \frac{nK \left( \frac{8u_m}{D} \right)^n + \eta_\infty \left( \frac{8u_m}{D} \right)}{\tau_0 + K \frac{8u_m}{D}^n + \eta_\infty \left( \frac{8u_m}{D} \right)}$$

The results showed that the introduction of a generalized Herschel-Bulkley Reynolds number,  $Re_{GenHBE}$ , is not valid only for fluids exhibiting viscosity characteristics of the Herschel-Bulkley model, but for all viscosity laws which can be included in the given equation. These viscosity laws are limited to, Newtonian, Bingham, Ostwald de Waele (Power-Law) and Herschel-Bulkley, respectively.

The presented model allows estimating laminar, transitional and turbulent flow conditions. Due to its general nature, the model is applicable for Newtonian as well as Bingham-Plastic and Power-Law, due to relations between stated models with Herschel-Bulkley. It can be shown that introducing the rheology parameter for a specific model in the generalized Herschel-Bulkley equation, the aforementioned models will be derived. Thus, all viscosity laws are included in the presented expression.

From their work, they observed that since the viscosity of their fluid of interest, kerosene-gel, reached the Newtonian plateau for large shear rates, it is assumed that the critical Reynolds number where the fluid transitions from laminar to turbulent was from that of Newtonian fluids,  $Re_{crit} = 2300$ , up to around 4000, highly dependent on the rheology.

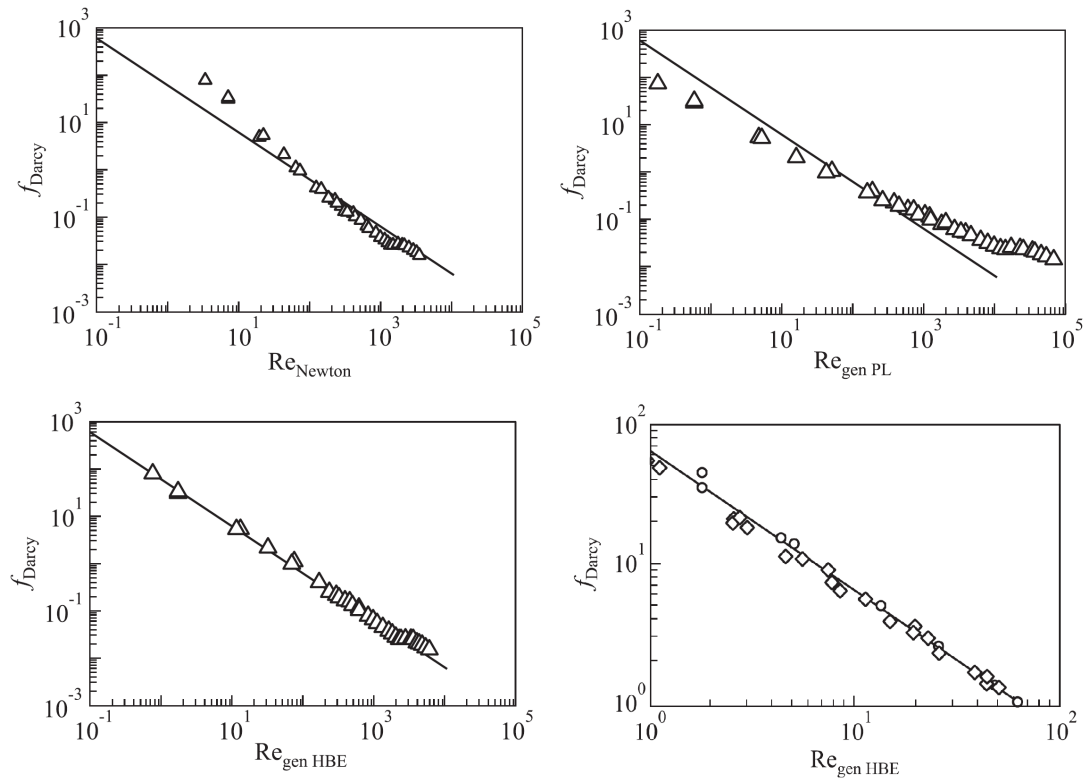


Figure 2.7.: Correlated data of fluids with the Reynolds number model plotted against friction factor, Madlener et al. (2009).

### 2.2.2. Effects of Eccentricity

The common term in petroleum engineering is to use *stand-off* as an measure of eccentricity, which may be expressed as:

$$\text{Stand-off [\%]} = \frac{C}{A - B} * 100 \tag{2.2}$$

, where A is the radius of the outer circle, B is the radius of the inner circle, and C is the lower gap between the inner and outer diameter, seen in Fig. 2.8.

For 100 % stand-off implies concentricity between the casing and open-hole, and 0 % stand-off denote that the casing is in contact with the wellbore.

For an annulus, eccentricity is defined as the ratio of the distance between the center of the outer and inner diameter located on the axis. In mathematical terms, this may be expressed

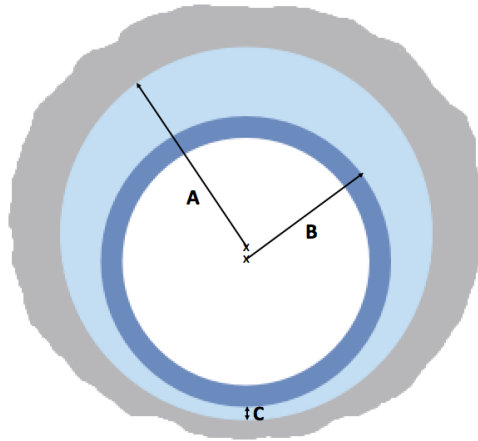


Figure 2.8.: An annulus defined with variables which decides degree of eccentricity.

as:

$$\text{Eccentricity} = 1 - \frac{C}{A - B} \quad (2.3)$$

If the casing string is eccentrically positioned in the wellbore, the main effect is for the fluid to follow the path of less resistance. This will occur in the wider section of the wellbore, often referred to as the *high-side*. Similarly, the narrow section in the annulus, due to eccentricity, is called the *low-side* of the annulus. In addition, another contribution of high-side channeling is the non-zero yield stress, which is the non-Newtonian characteristic of most drilling fluid [20].

To give a more general classification of the different fluids, the drilling mud will be referred to as mud, the injected fluids as spacer, and the cementing fluids as cement.

The efficiency of the displacement of mud in eccentric annulus is determined by the following factors:

- Eccentricity/Stand-off
- Yield stress and effective viscosity
- Density of spacer
- Flow rates

An alternative method for prediction of pressure loss in eccentric annulus was presented by Hacıislamoglu (1989). A correlation of frictional pressure losses for eccentric annulus was presented by using a correlation factor and the pressure loss based on concentric geometry. This correlation is expressed as:

$$R = \frac{\left(\frac{\Delta P_f}{\Delta L}\right)_e}{\left(\frac{\Delta P_f}{\Delta L}\right)_c} \quad (2.4)$$

, where the correlation factor,  $R$ , is given as:

$$R = 1 - 0.072 \frac{e}{n} \left(\frac{D_i}{D_o}\right)^{0.8485} - 1.5e^2 \sqrt{n} \left(\frac{D_i}{D_o}\right)^{0.1852} + 0.96e^3 \sqrt{n} \left(\frac{D_i}{D_o}\right)^{0.2527} \quad (2.5)$$

This treatment has been further analyzed for prediction of pressure losses have been used in various studies, notably by Langlinais et. al. (1985) [26], Hacıislamoglu & Langlinais (1990) [27] and more recently by Peng et al. (2013) [6]. For the latter, an error estimation of the Herschel-Bulkley model was performed with high-order non-Newtonian rheology models.

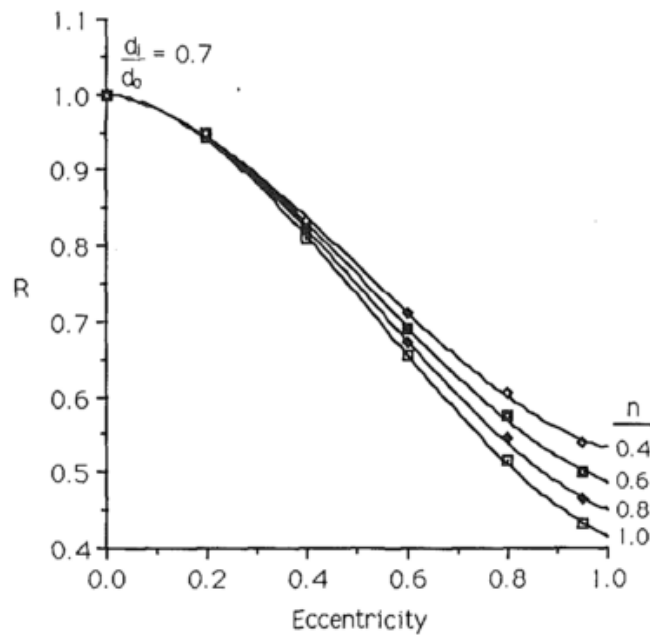
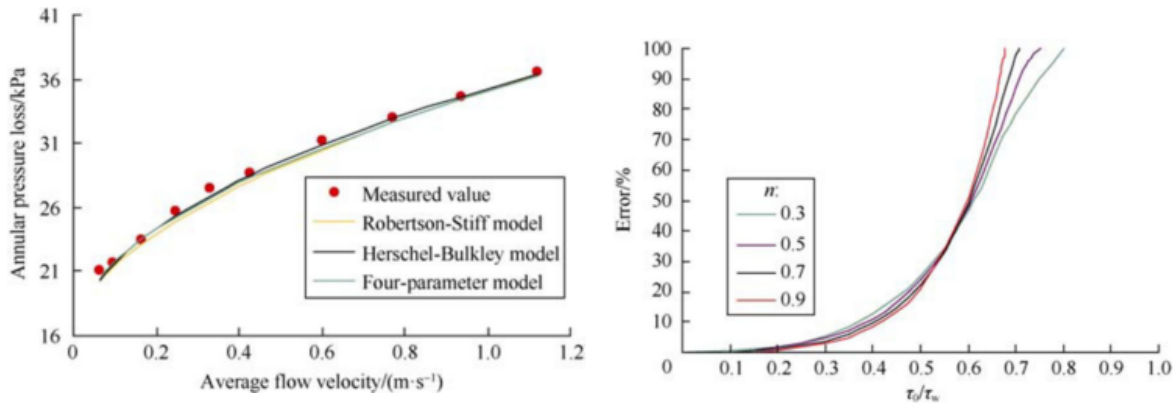


Figure 2.9.: Correlation factor vs. eccentricity for a annulus with pipe ratio of 0.7 (Hacıislamoglu & Langlinais) [5].



(a) Pressure loss analysis from different rheological models. (b) Error analysis of the Herschel-Bulkley model.

Figure 2.10.: Rheology analysis for Herschel-Bulkley model performed by Peng. et. al. (2013) [6].

As seen in Fig. 2.10, the Herschel-Bulkley model showed satisfactory fitment compared with experimental data and other rheological models. It was shown for the error estimation of Herschel-Bulkley that the error related to the ratio of the yield stress of the fluid and wall shear stress increased as the ratio increased, with different flow index parameter,  $n$ .

### 2.2.3. Modelling Primary Cementing in Annulus

The modelling approach for fluid displacement may typically be performed in three different ways, that is:

1. Kinematic Models
2. 2D Models
3. 3D Models

For complex geometry and conditions, it is shown that an utilization of CFD may yield a significant amount of data for different flow problems. Numerous studies in this field have been conducted, especially for pressure loss prediction, velocity characteristics, and multiphase analysis for including two or more phases. Some studies that approach analyses with CFD modelling will be presented.

For analysis of single-phase non-Newtonian fluids of the effect of eccentricity, there ex-



ist numerous research in the literature. Sorgun & Ozbayoglu (2011) presented a study on frictional pressure loss of horizontal drilling with non-Newtonian fluids [28]. By using a Eulerian-Eulerian multiphase model, the authors performed extensive experiments, validating against the CFD simulations, and presented pressure losses and flow characteristics of given cases. Sorgun (2010) [29] performed similar study, comparing with experimental and the *slot flow approximation*, presented by Fredrickson & Bird (1958) [30]. Rushd et al. (2017) [31], Zhigarev et al (2016) [32], Mao et al. (2012) [33] and Podryabinkin et al. (2013) [34], all performed noticeable studies on the analysis of eccentric annuli.

On the other hand, for studies involving multiphase analysis for studying fluid-fluid in annuli, present studies in the literature, there exists less extensive analysis. Both in terms of modelling and experimental approaches.

Noticeable studies was performed by Zulqarnain & Tyagi (2016) [7] and Enayatpour & van Oort (2017) [35], performing 2D and 3D CFD studies for modelling cement displacement complexities. Both studies were based on three- and two-phase modelling approach with mud-spacer-cement utilizing the Volume of Fluid (VOF) multiphase model. It can be noted that the studies were not performed for the same case, but showed similarities in both approach and trends of the results. Although, the effects of displacement and the presence of instabilities shows that the difference in CFD set-up, as well as rheology and operational parameters, may have resulted in the difference in results.

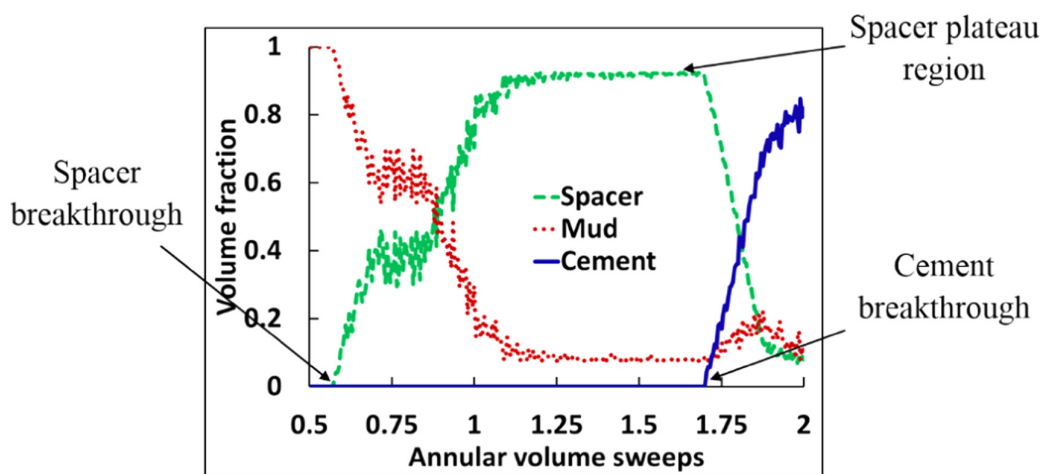


Figure 2.11.: A representative plot from the study Zulqarnain & Tyagi (2016), describing a displacement plot [7].

## 2.2. FLUID FLOW AND DISPLACEMENT IN THE ANNULUS

---

The areas of eccentricity and fluid-fluid analysis are the focus areas for this thesis of multi-phase flow modelling of primary cementing.

Part II.

Computational Fluid Dynamics

# Fluid Dynamics & Flow Modelling

---

# 3

The basis of the following discussion is based on the fundamentals of fluid dynamics, which are thoroughly discussed in Appendix. A.7.

For clarity, the most important mathematical aspects will be defined. The *continuity* equation, given as:

$$\nabla \cdot \mathbf{u} = 0 \quad (3.1)$$

The *Navier-Stokes* equation, given as:

$$\frac{\partial(\rho\mathbf{u})}{\partial t} + \nabla \cdot (\rho\mathbf{u} \otimes \mathbf{u}) = -\nabla P + \mu\nabla \cdot \boldsymbol{\tau} + S_M \quad (3.2)$$

The rest of the following chapter will have an emphasis on rheological modelling and implementation of the fundamental equations for CFD purposes.

## 3.1. Rheological Model Application for Viscous Term

The conservation equations for fluid flow has more unknown variables than equations. This is referred to as a closure problem. To close the system, there is required additional mathematical relations which can be denoted as *constitute equations*.

For viscous stresses,  $\boldsymbol{\tau}$ , a constitutive equation is the *rheological equation of state*, which describes the stresses in the fluid as a function of the strain rate that the fluid experience.

Fluids can be characterized as Newtonian and non-Newtonian. Newtonian fluids exhibit viscous stress in the fluid as a function of a strain rate. More generally, isotropic, isothermal Newtonian fluids have a constitutive equation given by:

$$\boldsymbol{\tau} = \mu \dot{\boldsymbol{\gamma}} - \frac{2}{3} \mu (\nabla \cdot \mathbf{u}) \boldsymbol{\delta} \quad (3.3)$$

, where  $\mu$  is the constant dynamic viscosity,  $\boldsymbol{\delta}$  is the Kronecker delta and  $\dot{\boldsymbol{\gamma}}$  is the strain rate vector, or rate of deformation tensor defined:

$$\dot{\boldsymbol{\gamma}} = \nabla \mathbf{u} + (\nabla \mathbf{u})^T \quad (3.4)$$

Applying the assumption of incompressible fluid, isothermal flow, and Newtonian fluid, the viscous stress tensor becomes:

$$\boldsymbol{\tau} = \mu \dot{\boldsymbol{\gamma}} \quad (3.5)$$

### Non-Newtonian contribution on Rheological Equation of State

For non-Newtonian fluid, various characterization can be used for describing it. The following represents some ways:

- A fluid whose stress is a non-linear function of strain rate
- A fluid which exhibits non-zero normal stress difference in shear flows
- A fluid with a memory effect due to micro-structures

A non-Newtonian fluid cannot be described by eq.(3.3). Thus, another representation has to be provided for it to be applicable in the viscous stress term. Two main classifications of non-Newtonian fluids are time-independent (inelastic) fluids or time-dependent (viscoelastic) fluids. In both cases, an important characteristic of a non-Newtonian fluid is a shear-rate

dependent viscosity,  $\eta(\dot{\gamma})$ , where the shear rate is given by:

$$\dot{\gamma} = \sqrt{\frac{1}{2}\dot{\gamma}\dot{\gamma}} = \sqrt{\frac{1}{2}\sum_{i,j}\dot{\gamma}_{ij}\dot{\gamma}_{ij}} \quad (3.6)$$

, where the last term is given by Einstein summation.

If the predominant rheological characteristic of a fluid is time-independent and shear rate dependent viscosity, then the fluid may be modelled with the general constitutive equation:

$$\tau = \eta(\dot{\gamma})\dot{\gamma} \quad (3.7)$$

, where a viscosity model must be specified for  $\eta(\dot{\gamma})$ . These models are empirical by nature. Fluids with a shear rate-dependent viscosity  $\eta(\dot{\gamma})$  can be classified into different non-Newtonian rheological classifications.

#### Classification of non-Newtonian Rheological Models

As stated previously, non-Newtonian fluids are characterized by a non-linear relationship between strain and stress rates. These characteristics form the basis of classification of fluids exhibiting different characteristics as the following [36]:

- Shear-thinning (Pseudoplastic)
- Shear-thickening (Dilatant)
- Yield-Value (Viscoplastic)

For each of these classifications, there exist various different non-Newtonian models describing the rheology of the fluid. Deciding which model which is suited for the numerical computations, is affected by various factors. For instance, the rheology of the fluid itself, which can be determined through experiments, required accuracy, computational resources, complexity, etc.

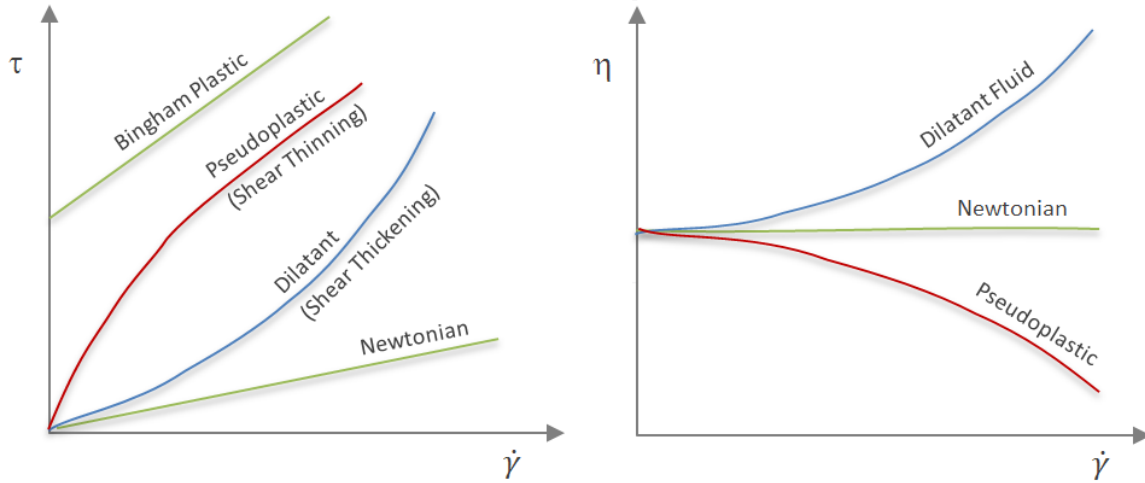


Figure 3.1.: Four time-independent fluids presented [8].

### Rheological Parameters non-Newtonian Fluids

For a general description of non-Newtonian behaviour, three parameters characterize this relationship, namely the *consistency index*,  $K$ , flow index parameter,  $n$ , and yield shear stress,  $\tau_0$ . The consistency index describes the rheological properties related to cohesion in the fluid, its ability to deform and its resistance to the flow. The consistency index is directly proportional to the effective viscosity of the fluid [37]. The flow behaviour index is the measure of the shear-thinning effect. For Newtonian fluids, this relationship is linear, i.e  $n = 1$ . Fluids with shear-thinning properties have flow behaviour index of  $n < 1$ , whereas shear-thickening fluids have values of  $n > 1$ .

Due to the fact that the viscosity of non-Newtonian fluids changes with the shear rate, the term of *effective viscosity* is defined to give an expression which compensates for the change of shear rate of the viscosity. The effective viscosity and the corresponding effective shear stress can be defined as:

$$\eta_e = \frac{\mu}{\dot{\gamma}} \qquad \tau_e = \frac{\tau}{\dot{\gamma}} \qquad (3.8)$$

, where  $\eta_e$  denotes the effective viscosity and  $\tau_e$  is the effective shear stress. The viscosity  $\eta$

is used to distinguish effective viscosity from the dynamic Newtonian viscosity,  $\mu$ .

For Bingham-Plastic fluids, shear stress can be defined as:

$$\tau_e = \tau_0 + K \dot{\gamma} \quad (3.9)$$

For Power-Law fluids, the non-Newtonian model is represented by the Ostwald de Waele model,

$$\tau_e = K \dot{\gamma}^n \quad (3.10)$$

For the Yield Power-Law model, also known as the Herschel-Bulkley model, a three-parameter fluid model is used to model the fluid behaviour. This was introduced by Herschel & Bulkley (1926) and is represented as:

$$\tau_e = \tau_0 + K \dot{\gamma}^n \quad (3.11)$$

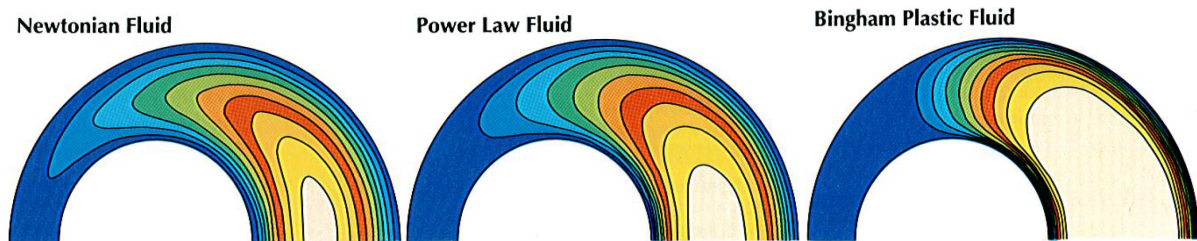


Figure 3.2.: An illustration of different velocity regions for three type of fluids in eccentric annuli [9].

Choosing the non-Newtonian model will ultimately decide which mathematical representation of  $\eta(\dot{\gamma})$ , which is to be implemented for the viscous stress. Consequently, the fluid problems involving non-Newtonian fluids are very similar to Newtonian problems, but where the expression for shear stress is determined by either eq. (3.5) for Newtonian fluids, and eq. (3.7) for Non-Newtonian fluids, where a suitable non-Newtonian model needs to be specified for solving the problem.



## 3.2. Multiphase Flow

Multiphase flow is defined as the simultaneous flow of material of different phases, i.e gas, liquid and solid, or exhibiting chemical properties for the same phase, such as a fluid-fluid system of oil in water. The phases may be denoted as primary, secondary phases, and so on, depending on the number of phases of interest. For two-phase dispersed multiphase flow, the primary phase will be the continuous phase whilst the secondary are dispersed in the continuous phase. For stratified flow, the phases are separated by an interface between the phases [38].

Regarding multiphase flow, the volume fraction of phases of the domain is often of interest. Each phase exhibit the same flow characteristics as any fluids. The major difference compared to single-phase flow, taking dispersed flow as an example, the primary phase may be in the turbulent flow regime, while the secondary phase remains turbulent with respect to the continuous phase.

In the following a list of multiphase flow regimes is given:

- *Discrete bubble flow*: Discrete gaseous bubbles in continuous liquids
- *Annular flow*: Continuous liquid along walls where gaseous flow is in the core
- *Droplet flow*: Discrete fluid droplets in continuous gases
- *Slug flow*: Large gaseous bubbles in continuous liquid
- *Particle-laden flow*: Discrete solid particles in a continuous fluid
- *Stratified flow*: Immiscible fluids separated
- *Free-surface flow*: Immiscible fluids separated by an interface, such as air and water

In industrial applications, multiphase flow is of importance for processes such as fluidized bed, bubble-column reactors, scrubbers, combustion, open channel flows, etc. The typical objective when conducting flow analysis for multiphase flow is to understand the flow dynamics of the total system or the interaction of phases for an operation or process.

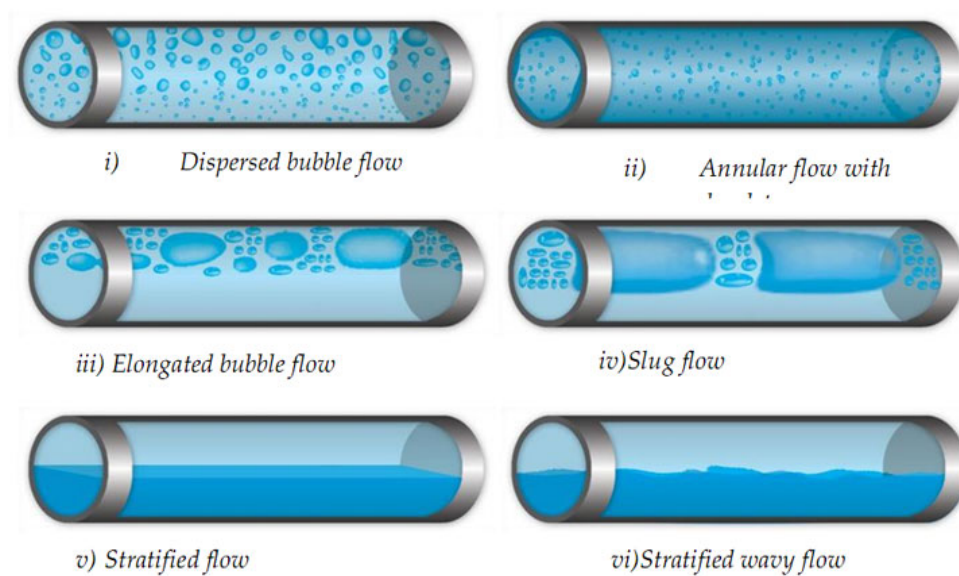


Figure 3.3.: Example of gas-liquid flow for different multiphase flow regimes [10].

### 3.2.1. Physics of Multiphase flows

Due to the complexity of multiple phases for a flow problem, there are various characteristics that must be understood before performing a multiphase analysis. These may be:

- Characteristics of the flow
- Flow regime present for the phases
- Modelling one flow regime at a time
- Diluted or dense flow
- Additional physical modelling, such as for drag considerations

### 3.2.2. Modelling approach

There exists several approaching for modeling the physics of multiphase flow. The most basic is the empirical correlations, to the fully resolved and coupled treatment. In between are of these two extrema are the five main classes for multiphase analysis, which is [39]:

- Eulerian-Lagrangian model
- Eulerian-Eulerian model

- Mixture model/Algebraic-slip model
- Porous-bed Model
- Volume-of-Fluid Model

For *Eulerian-Lagrangian modelling*, the primary phase is modelled as a continuum, solving for the Navier-Stokes equations. For the secondary phase, a large number of individual particles are modelled as the dispersed phase, where it can exchange mass, momentum, and energy with the fluid phase. Due to this treatment, the particle trajectories are computed for either each particle or for a bundle of particles. This approach is limited to systems where the volume fraction of the dispersed phase is low.

For *Eulerian-Eulerian* models, all phases are treated as continuous phases, where continuity and momentum are solved for each phase. This model can handle flows with high complexity, but may not yield satisfying results, due to that empirical models is needed due to closure problems of the momentum equations. Applications for this model are stirring in tanks, bubble columns, and other areas.

For *mixture model*, also referred to as *Algebraic-slip model*, the phases are assumed to interact in a significant manner, such that solving momentum balances between phases for each phase is not required. A key factor is the mixture model is the modelling of viscosity for the mixture. Velocities for the respective phases are computed from drag, buoyancy and other forces that may affect the flow characteristics. Examples of applications are fine particle suspensions, stirring and other.

For the *porous-bed model*, the modelling aspect is the pressure drop across the porous bed. Assuming a bed containing a lot of particles, the geometry complexity becomes a constraint for solving the Navier-Stokes. Thus, the pressure drop is needed through derived models.

Lastly, for the *Volume-Of-Fluid model*, this model is based on a Eulerian-Eulerian type, where the interface between phases is tracked. VOF modelling is suitable for stratified flows, free-surface flows and bubble flow where there exists large movement in liquids. Due to issues resolving the interfaces, it is not applicable for small droplets or bubbles.

The most relevant model for the problem of interest, the VOF model is the most suited model to analyze the displacement of mud, spacer, and cement. When the rheology of the fluids chemistry is developed, fluid interaction is an important parameter, where the fluids should not intermix or disperse during displacement. Due to this premise, this implies that stratified flow is a reasonable assumption. Thus, any further discussion of multiphase modelling will have an emphasis on stratified flow, and especially VOF modelling.

**Models for Stratified Flows: Fluid-Fluid Interaction**

As mentioned in Section. 3.2.2, the objective is to track the interface of the phases. Where Lagrange and Euler-Euler models fail, utilization of stratified modelling such as front-tracking, level-set or VOF methods should be applied. Furthermore, these models can be applied for more advanced CFD approaches, such as DNS for dispersed multiphase problems. It must be noted that the aforementioned methods assume no-slip condition between the interface, which also will require to be resolved all the way to the Kolmogorov length scale in presence of turbulence.

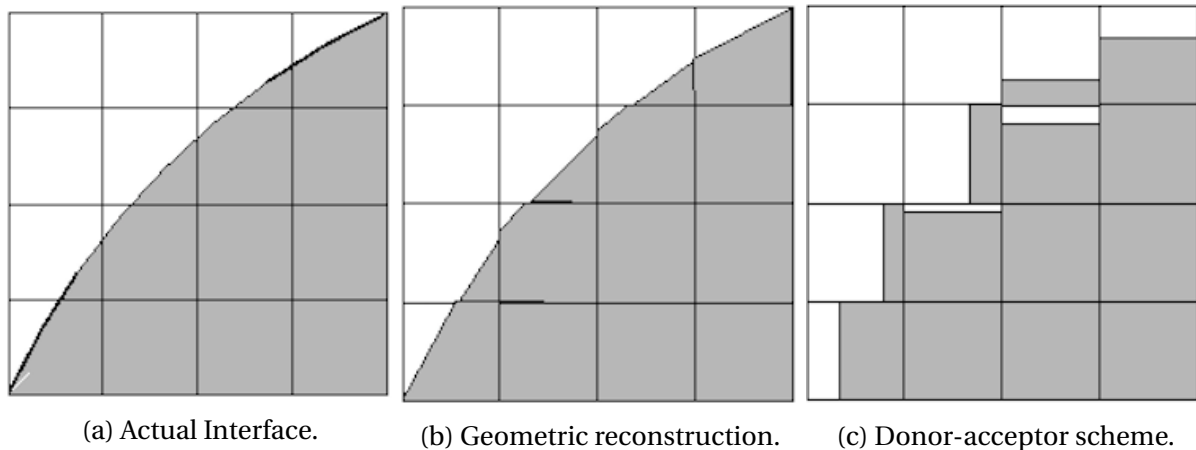


Figure 3.4.: Interface calculations for geometric reconstruction and the donor-acceptor scheme to represent the actual interface [11].

**3.2.3. Volume-of-Fluid Method**

The VOF method uses the volume fraction on a cell basis to give information about the interface. The advective terms of the equation are solved by special schemes, such as Lagrangian and geometrical schemes. The schemes for the advection can handle situations regarding

cross-flow and are better at handling mass conservation, rather than the counterpart, which is the level-set method. However, due to the interface problematics, it can be shown that the accuracy is only first-order in space and time, and a refined computational grid is required to resolve the physics.

### Volume Fraction of Multiphase systems

The tracking of interfaces is performed by obtained the solution of the continuity equation expressed with the volume fraction of the phases. This can be expressed as [11]:

$$\frac{1}{\rho_q} \left[ \frac{\partial}{\partial t} (\alpha_q \rho_q) + \nabla \cdot (\alpha_q \rho_q v_q) = S_{\alpha_q} + \sum_{p=1}^n (\dot{m}_{pq} - \dot{m}_{qp}) \right] \quad (3.12)$$

, where  $\alpha_q$  is the volume fraction of the  $q$ th fluid,  $S_{\alpha_q}$  is the source term, and  $\dot{m}_{pq}$  and  $\dot{m}_{qp}$  is the mass transfer between the phase  $p$  and fluid  $q$ .

The volume fraction,  $\alpha$ , has three possible conditions are the absense of fluid  $q$  in a cell,  $\alpha_q = 0$ , fluid  $q$  completely fills the cell,  $\alpha_q = 1$ , and where a cell contains the interface and is filled by fluid  $q$  with one or more fluids,  $0 \leq \alpha_q \leq 1$ .

The material properties of a multiphase system of  $n$  phases, the density is computed by the volume fraction averaged density given as:

$$\rho = \sum \alpha_q \rho_q \quad (3.13)$$

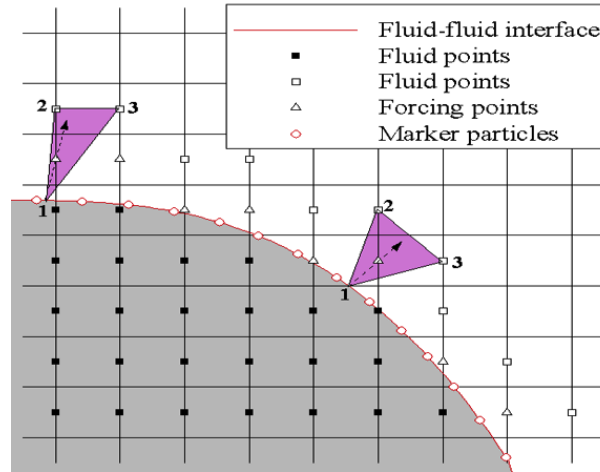


Figure 3.5.: An illustration of interface between two fluid and showing the normal-vector [12].

### Surface Tension

VOF modelling includes the effects of surface tension forces for the interface between the phases. Additional specifications of contact between the phases and the walls, such as capillary forces, can be implemented if required. These forces are included in the formulations for momentum equations for the source terms.

The surface tension model used for formulating the VOF in Fluent is the continuum surface force model presented by Brackbill (1992) [40]. Surface forces can be expressed as volume forces, by applying Gauss's theorem, and the following can be expressed as[11]:

$$F_{surface} = \sum_{i \neq j} \sigma_{ij} \frac{\alpha_i \rho_i \nabla \cdot n_j \nabla \alpha_j + \alpha_j \rho_j \nabla \cdot n_i \nabla \alpha_i}{\frac{1}{2}(\rho_i + \rho_j)} \quad (3.14)$$

, where  $\sigma$  is the surface tension coefficient and  $\nabla \cdot n$  divergence of the unit normal vector in the  $i$ - or  $j$ -direction.

For the momentum equations, the computation of eq.(3.12), (3.13) and (3.14) is used in the momentum equation (A.14), where the surface forces are included in the source term. It must be noted that only the cell in the interface that is shared among the cells for the respective phases that the momentum equation is different than that of single-phase models.

The effects of surface tension must be included in the analysis by checking the capillary number and Weber number. These are defined as:

$$Ca = \frac{\mu U}{\sigma} \qquad We = \frac{\rho L U^2}{\sigma}$$

, where  $U$  is the free-stream velocity, and  $L$  is the length scale.

The effects of surface tensions should be included if  $Ca < 1$  or  $We < 1$ , and may be neglected if  $Ca \gg 1$  or  $We \gg 1$ .

The energy equation is not considered due to its absence from the CFD model used in the thesis. For other scalar quantities, such as turbulence variables, a single set of transport equations is solved where the turbulence parameters are shared for the phases.

### 3.3. General Transport Equation

From the momentum Eq. (A.14), it can be shown that there are significant commonalities between the various equations. Introducing a general scalar variable  $\phi$ , the conservative form of all fluid flow equations, including equations for scalar quantities, may be written in general form, expressed as the following:

$$\frac{\partial(\rho\phi)}{\partial t} + \nabla \cdot (\rho\phi u) = \nabla \cdot (\Gamma\nabla\phi) + S_\phi \quad (3.15)$$

, where  $\Phi$  is a scalar transport property,  $\Gamma$  is the diffusion coefficient, and  $S_\phi$  is the source term of  $\Phi$  [15].

It can be noted that bringing out the common features for the transport equations requires to hide term which is not shared between the conservation equations into the source term,  $S_\phi$ . This mathematical representation clearly highlights the various transport properties present for fluid flow.

In words, Eq.(3.15) represents rate of increase of  $\phi$  of the fluid element + net rate of flow of  $\phi$  out of fluid element, which equals the rate of increase of  $\phi$  due to diffusion + rate of increase of  $\phi$  due to source terms.

Eq. (3.15) is the instance of departure for computational procedures for FVM, which will be explained and analyzed in more depth in section 4.2. By providing an input of  $\phi$  equal to the transport properties (1, u, v, w, P, etc.), and selecting suitable values for  $\Gamma$  and  $S_\phi$ , the five PDEs of mass, momentum and energy conservation is obtained, seen in Table. 3.1.

The key step of FVM, which is to be developed, is the integration of Eq. (3.15) over the CVs:

$$\int_{CV} \frac{\partial(\rho\phi)}{\partial t} dV + \int_{CV} \nabla \cdot (\rho\phi u) dV = \int_{CV} \nabla \cdot (\Gamma\nabla\phi) dV + \int_{CV} S_\phi dV \quad (3.16)$$

The volume integrals can be rewritten as the integrals over boundaries of the CVs. This is



Table 3.1.: Transport Equation variable substitution for acquiring the fluid equations.

Equation	$\phi$	$\Gamma$	$S_\phi$
Mass Conservation	1	1	$\phi$
X-momentum	$u$	$\mu$	$\frac{\partial p}{\partial x} + \rho f_x$
Y-momentum	$v$	$\mu$	$\frac{\partial p}{\partial y} + \rho f_y$
Z-momentum	$w$	$\mu$	$\frac{\partial p}{\partial z} + \rho f_z$
Energy Equation	$T$	$\kappa / c_p$	$(\tau \cdot \nabla) \cdot u / c_p$
Specific Mass Fraction	$Y_k$	$\rho D_k$	$\dot{\omega}_k$

performed be using *Gauss's divergence theorem*, which can be stated as:

$$\int_{CV} \nabla \cdot (\mathbf{a}) dV = \int_A \mathbf{a} \cdot \mathbf{n} dA \quad (3.17)$$

, where  $a$  is a arbitrary vector and  $n \cdot a$  is the component of vector  $a$  in the direction of the vector  $n$  normal to surface element  $dA$ .

Applying Gauss's Divergence Theorem to Eq. (3.16), Eq. (3.16) can be written as:

$$\frac{\partial}{\partial t} \left( \int_{CV} \frac{\partial(\rho\phi)}{\partial t} dV \right) + \int_A (\rho u \phi \cdot n) dA = \int_A (\Gamma \nabla \phi \cdot n) dV + \int_{CV} S_\phi dV \quad (3.18)$$

It can be shown that in the general transport equation Eq. (3.18) can become the fundamental fluid equation be substituting  $\phi$ ,  $\Gamma$  and  $S_\phi$  with the terms seen in table 3.1, as discussed previously.

The discussion presented, clarifies that integration of the PDE generates a statement of the conservation of fluid properties for a finite-sized control volume. This forms the fundamental basis of the Finite Volume Method for solving fluid flow problems.

# Assessment of CFD Implementation

---

# 4

A discretization method is a technique of approximating the partial differential equations by a system of algebraic equations for the variables of a set of discrete locations in space and time. The discretization process for Finite Volume Method (FVM) can be summarized with the following properties:

- Method based on discretizing the integral form of the conservation equations over each control volume of the discrete domain. The basic quantities, such as mass and momentum, will be conserved at the discrete levels.
- Method is applicable for control volumes for any given geometry
- The systems of PDEs is evaluated in a coupled or segregated manner
- Method is applicable for both steady-state and transient simulations.

## 4.1. Differencing Schemes

In computational physics, various different numerical methods exist for solving partial differential equations. Furthermore, numerous classes of numerical discretization methods are available for treating PDEs of different characteristics.

The following section will only take account for numerical discretization methods commonly used for CFD applications, and utilized in this thesis.

### 4.1.1. Assessment of Upwind Discretization Scheme

#### Upwind Scheme

For analysis utilizing computational physics, the schemes using an upwind approach known as *upwind schemes*, denote a class of discretization methods for solving hyperbolic PDEs. Upwind schemes are based on an adaptive FDM evaluate the direction of which the information in a flow field propagates. Moreover, by using FDM biased approach, the direction of flow propagation are determined by the characteristic speeds [41].

To be able to illustrate this method, consider the linear advection equation in the  $x$ -direction:

$$\frac{\partial u}{\partial t} + a \frac{\partial u}{\partial x} = 0 \quad (4.1)$$

, which describes a wave propagating with a velocity  $a$  in the  $x$ -direction.

#### First-order Upwind Scheme

The most simple upwind scheme of eq. , is the first-order upwind scheme, given by:

$$\frac{u_i^{n+1} - u_i^n}{\Delta t} + a \frac{u_i^n - u_{i-1}^n}{\Delta x} = 0, \text{ for } a > 0 \quad (4.2)$$

$$\frac{u_i^{n+1} - u_i^n}{\Delta t} + a \frac{u_{i+1}^n - u_i^n}{\Delta x} = 0, \text{ for } a < 0 \quad (4.3)$$

### Second-Order Upwind Scheme

For discretization of the linear advection equation, the spatial accuracy can be increased by evaluating for three nodes, instead of two which is the case for the first-order upwind method. As a result, a more accurate finite difference stencil is used to approximate the spatial derivative. The second-order upwind scheme may be expressed as:

$$u_x^- = \frac{3u_i^n - 4u_{i-1}^n + u_{i-2}^n}{2\Delta x} \quad (4.4)$$

and a three-point forward difference is defined,

$$u_x^+ = \frac{-u_{i+2}^n - 4u_{i+1}^n + 3u_i^n}{2\Delta x} \quad (4.5)$$

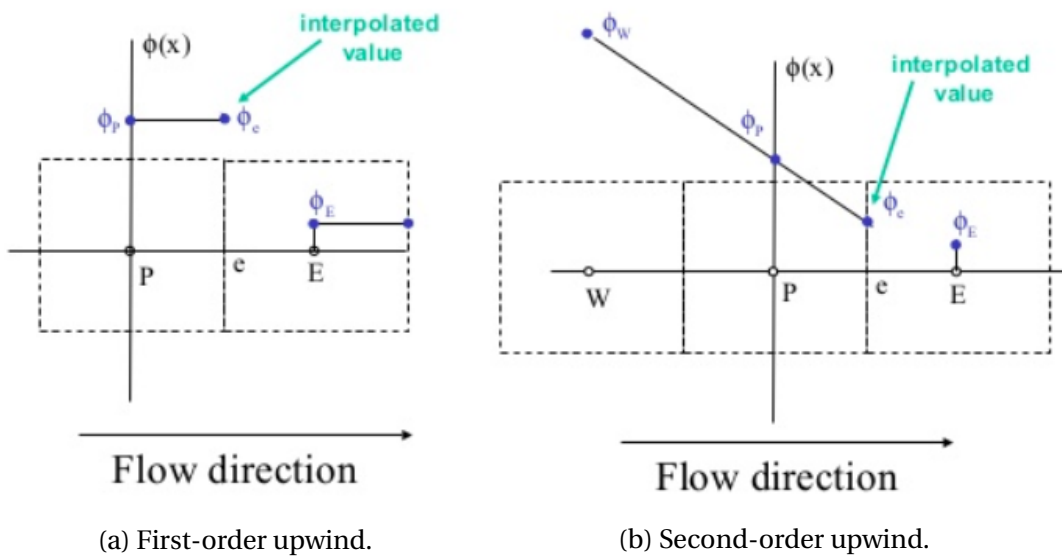


Figure 4.1.: Stencils for first- and second-order upwind considered in the x-direction.

### Stability of the Upwind Schemes

For the transient simulations performed in this thesis, being aware of the stability conditions is a great tool for preventing diverging simulations.

The stability of the upwind scheme is determined by the Courant-Friedrichs-Lewy (CFL) condition is satisfied [42]:

$$C = \left| \frac{a\Delta t}{\Delta x} \right| \leq 1 \quad (4.6)$$

If a *Taylor expansion analysis* of the upwind scheme is performed, it can be shown that the scheme is first-order accurate in space and time, i.e  $O(\Delta x, \Delta t)$ .

Using first-order difference in time, and first-order upwind in space, it can be shown by performing a von Neumann stability analysis that the first-order upwind scheme has a stability condition of:

$$C \leq \frac{\Delta x}{\Delta t} \quad (4.7)$$

Eq. 4.7 shows that the discretization scheme is conditionally stable if and only if the velocity,  $C$ , is less than the step length,  $\Delta x/\Delta t$ , where the  $\Delta x$  can represent the size of the largest cell, and  $\Delta t$  is the time-step.

For the second-order upwind consideration, we assume that first-order difference stencil for time in the linear advection equation. This is also known as the *Beam-Warming* second-order upwind method [43]. Through von Neumann analysis, with Fourier analysis applied, it can be shown that the stability condition is:

$$\Delta t \leq 2 \frac{\Delta x}{|a|} \quad (4.8)$$

, where the CFL condition should be fulfilled.

The second-order scheme show less diffusive behaviour compared to the first-order scheme. In addition, the scheme has the ability to not be restricted by the Peclet number and has a less diffusive than the first-order scheme, which results in a more accurate method when applied for discretization of physical problems.

### 4.1.2. Properties of Discretization Schemes

The downside of the differencing method is that for certain cases for both convection and diffusion, it is highly beneficial to be aware of the properties of the discretization schemes. Since the computational domain has to be divided into a finite amount of cells, the numerical analysis will only be physically feasible when the discretization employed show certain properties. The most influential is the following:

- Conservativeness
- Boundedness
- Transportiveness

Accuracy and stability will also provide significant relevance, but in terms of the effect of discretization, the focus will be on the three presented properties.

#### Conservativeness

Evaluating convection-diffusion problems over a finite computational domain, consisting of finite control volumes yields a system of discretized conservation equations involving the transport property  $\phi$  through the CV. To ensure that the conservation laws are met for the solution of the entire domain, the transport property  $\phi$  entering and leaving a CV must be equal to give physical meaning. This is achieved by representing the adjacent cells that share a common cell boundary in a consistent manner for the entire system of CVs.

#### Boundedness

At each node, the discretized equations represent a set of equations that is to be solved to obtain a solution. Typically, iterative techniques are utilized to solve these large systems

of equations. These methods initialize the solution with an initially guessed distribution of the transport quantity,  $\phi$ , and continuously update the data structure for the computational domain until a converged solution is reached. It can be shown that a sufficient condition for convergence of iterative methods, in terms of numerical analysis, can be expressed as:

$$\frac{\sum |a_{nb}|}{|a'_p|} = \begin{cases} \leq 1 & \text{at all nodes} \\ < 1 & \text{at least in one node} \end{cases} \quad (4.9)$$

, where  $a'_p$  is the net coefficient of cell P, and the summation is taken over all the neighbouring nodes ( $nb$ ) [44].

If the chosen differencing schemes produce coefficients from the discretized transport equation that satisfy the criterion given in eq. 4.9, the resulting coefficient matrix is *diagonally dominant*. Diagonally dominance is a property that satisfies the criterion of *boundedness*.

### Transportiveness

The property of *transportiveness* for fluids, can be illustrated by considering the effect at the cell of interest,  $P$ , due to constant sources of the transport quantity  $\phi$  [45].

This can be quantified by using the cell-Peclet number, which is a measure of relative strength convection and diffusion expressed as:

$$Pe = \frac{F}{D} = \frac{\rho u}{\Gamma/\delta x} \quad (4.10)$$

, where  $\delta x$  is the characteristic length [15].

For two extreme cases, as the cell-Peclet number goes towards 0, this means there is no convection and pure diffusion. Where the counterpart is the cell-Peclet number going towards infinity, there is no diffusion and pure convection. The transportiveness is an important measure, as it represents the relationship between the flow direction and rate of transportivity, expressed with the cell-Peclet number. The transportiveness is directly bourne from the

discretization scheme.



## 4.2. Discretization of Transport Equations

In the following, the discretization of the transport equation will be used in conjunction with FVM that results in the solution of equations, which form the basis of what is to be solved in a CFD simulation.

### 4.2.1. Discretization of the Continuity Equation

From the continuity equation, Eq. A.5, may be integrated over the control volume, as seen in Fig. 4.3 to yield the following discrete equation [11]:

$$\sum_f^N J_f A_f = 0 \quad (4.11)$$

, where  $J_f$  is the mass flux through cell boundary  $f$ ,  $A_f$  is the area of boundary  $f$ , and is summed over all boundaries of the control volumes.

Due to the utilization of *staggered grid* to prevent checkboard pattern, further discussed in Section. 4.7.1, Fluent uses a technique similar to that of Rhie and Chow, preventing numerical diffusion [46]. The discretization of continuity is performed where a momentum-weighting average is computed. This is done by using weight-factors based on coefficient from the cell-center,  $a_p$ , performed during the iteration of the transport equation for momentum, seen in Tab. ???. In conclusion, continuity is calculated with the following expression:

$$\begin{aligned} J_f &= \rho_f \frac{a_{p,c0} v_{n,c0} + a_{p,c1} v_{n,c1}}{a_{p,c0} v_{n,c1}} + d_f ((p_{c0} + (\nabla p)_{c0} \cdot \vec{r}_0) - (p_{c1} + (\nabla p)_{c1} \cdot \vec{r}_1)) \\ &= \hat{J}_f + d_f (p_{c0} + p_{c1}) \end{aligned} \quad (4.12)$$

, where the pressure and velocities is given by  $p_{c0}$ ,  $p_{c1}$  and  $v_{n,c0}$ ,  $v_{n,c1}$ , and  $\hat{J}_f$  contains influence of velocities in the cells of interest. The term given as  $d_f$  is a function of the average of the momentum equations for the cell-center, denoted  $\bar{a}_p$  [11].

### 4.2.2. Discretization of the Momentum Equation

For the transport equations, the difference scheme is already described in Section. 4.1. The following discretization is used for all scalar quantities, including for momentum. If the transport quantity is set as  $\phi = u$ , in eq. 4.18, the  $x$ -momentum equation is calculated in the form [11]:

$$a_p u = \sum_{nb} a_{nb} u_{nb} + \sum p_f A \cdot \hat{i} + S \quad (4.13)$$

, where  $p_f$  is pressure at a cell boundary calculated from an interpolation scheme.

The reasoning for having an additional calculation of pressure is to solve the problem due to storage of data and discretization of the pressure gradient. If all velocities and mass fluxes are known, the velocity field can easily be obtained. However, these quantities are not known a priori in the calculation and must be obtained during calculation of the solution. Due to the fact that a co-located scheme is enforced, the pressure and velocity are stored at the cell-centers, and not directly at the boundary of the cell, where it is calculated. Thus, an additional scheme is required to interpolate the pressures at all boundaries, given by the cell-value. The  $p_f$  is then calculated by [11]:

$$P_f = \frac{\frac{P_{c0}}{a_{p,c0}} + \frac{P_{c1}}{a_{p,c1}}}{\frac{1}{a_{p,c0}} + \frac{1}{a_{p,c1}}} \quad (4.14)$$

It can be mentioned that the interpolation scheme can be changed to any discretization scheme desired, but requires a more delicate procedure to adjust the solver calculation.

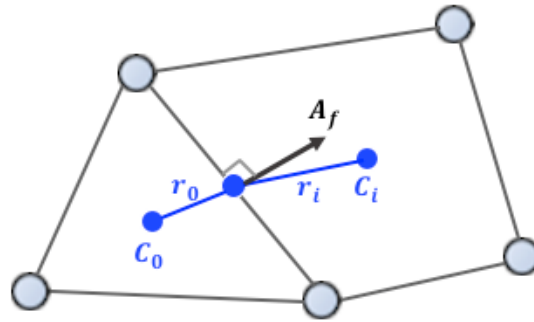


Figure 4.2.: An illustration of CV evaluation for gradients and scalar value consideration.

### 4.2.3. Differencing Schemes Employed in the Transport Equation

For the discretized equations to be computed, suitable differencing schemes should be chosen satisfying the requirements regarding the physical problem, mesh, accuracy and computational time.

Depending on the aforementioned requirements, suitable spatial discretization schemes implemented for the solution method must be chosen. For general fluid problems, there are three variables which must be solved for in any fluid dynamical problem. Due to the use of numerical methods, this results in choosing discretization schemes for:

- Gradient
- Pressure
- Momentum

### 4.2.4. Spatial Discretization: Gradient

The gradient  $\nabla\phi$  of the transport property  $\phi$ , is computed to be able to discretize the convection and diffusion terms. In Fluent, the gradients may be computed by three different methods:

- Green-Gauss Cell-Based
- Green-Gauss Node-Based
- Least-Squares Cell-Based

Computing and obtaining gradients is important for calculating values of any scalar at the cell boundaries, as well as computing velocity derivatives and secondary diffusion terms. If any other method is desired, a User-Defined code must be implemented.

The *Green-Gauss Cell-Based* computes face values taken from the arithmetic average of the values of the neighbouring cell centers. The *Green-Gauss Node-Based* computes the face values from the arithmetic average of the nodal values on the face.

### Least Square Cell-Based

The focus will now be addressed for the *Least-Square Cell-Based* which is the difference scheme used for gradient calculations in this thesis. For the method, a major assumption is that the solution is assumed to vary linearly. The change in cell values from an arbitrary cell  $C_0$  and  $C_i$  along the vector  $r_i$ , from the cell-center  $c_0$  and  $c_i$  can be expressed as:

$$(\nabla\phi)_i \cdot r_i = (\phi_{i+1} - \phi_i) \tag{4.15}$$

, where  $\phi$  represents any quantity of interest and  $r_i$  is the distance between cell  $i$  and the adjacent cell of interest  $i + 1$ .

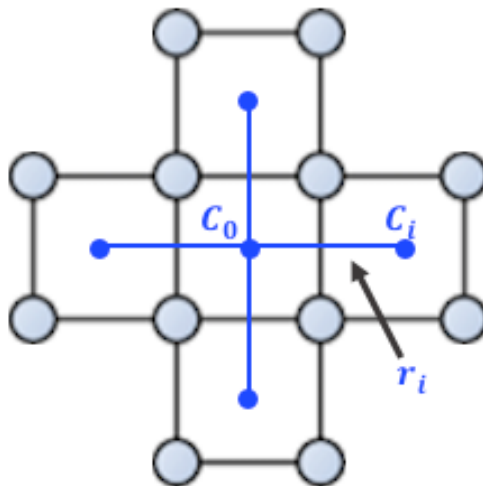


Figure 4.3.: An illustration of cell-center evaluation for least-square cell-based gradient.

The linear system of equations that is stated is over-determined, and is solved by using the

Gram-Schmidt process [47] in the code. The result of the process is a matrix of weights for each cell, and the gradient at the cell center can now be determined by multiplying with the weight factor.

For irregularities in the unstructured grid, such as cells with high skewness and distortion, where mesh quality is further discussed in Section. 5.2. The least-square method accuracy is equal to the accuracy of the node-based gradient method. On the other hand, it is less computationally expensive and is the main reason for choosing this solver [11].

For the second-order spatial discretization schemes chosen, the solver in *Fluent* uses a multidimensional linear reconstruction method, based on Barth & Jespersen (1989) work [48]. For this approach, a Taylor expansion is performed about the cell-center which yields high-order accuracy at the cell faces. Second-order upwind can be expressed as:

$$\phi_i = \phi + \nabla\phi \cdot \vec{r} \quad (4.16)$$

, where  $\phi$  represents the value at the cell-center  $\nabla\phi$  the gradient in the adjacent cell, and  $\vec{r}$  the direction vector from cell-center to the face-center. The gradient is determined by the least-square method, discussed previously.

#### 4.2.5. Spatial Discretization: Pressure & Momentum

The discretization is explained in Section. 4.2.2, where the general transport equation is applied for velocities or pressure. For the transport property, which is the velocities and pressure at the cell-centers and faces, the Least-Squares cell-based method is used for the transport properties, and a first-order or second-order upwind used, depending on the discretization scheme desired. This is explained in section 4.5 which are implemented in Eq. (4.13).

### 4.2.6. Explicit Scheme: Volume Fraction

The volume fraction equation, previously described in Section. 3.2.3, is discretized using any scheme desired. In Fluent, the discretization is of the form [11]:

$$\frac{\alpha_q^{n+1} \rho_q^{n+1} - \alpha_q^n \rho_q^n}{\Delta t} V + \sum_f (\rho_q U_f^n \alpha_{q,f}^n) = \left[ \sum_{p=1}^n (\dot{m}_{pq} - \dot{m}_{qp} + S_{\alpha_q}) \right] V \quad (4.17)$$

, where  $n$  is the index of previous time step,  $n+1$  is the index for the next time step,  $\alpha_{q,f}$  is the volume fraction computed from Eq. (3.12),  $V$  is the volume of the cell, and  $U_f$  is the volume flux through the cell.

Interpolation of cells containing one or more phases are described in Sec. 3.2.2, where a chosen interpolation scheme is used reconstruct the interface.

## 4.3. Solution of 3D Convection-Diffusion Problems with FVM

In the following, it will be shown how the discretization of the general transport equation reduces to a system of linear equations which can be implemented into general CFD code. This forms the basis of CFD implementable code based on numerical schemes and FVM techniques.

The first step starts with the generation of a computational domain. For a derivation of a simple general case, the *West-East-South-North-Bottom-Top* (WESNBT)-Stencil is utilized.

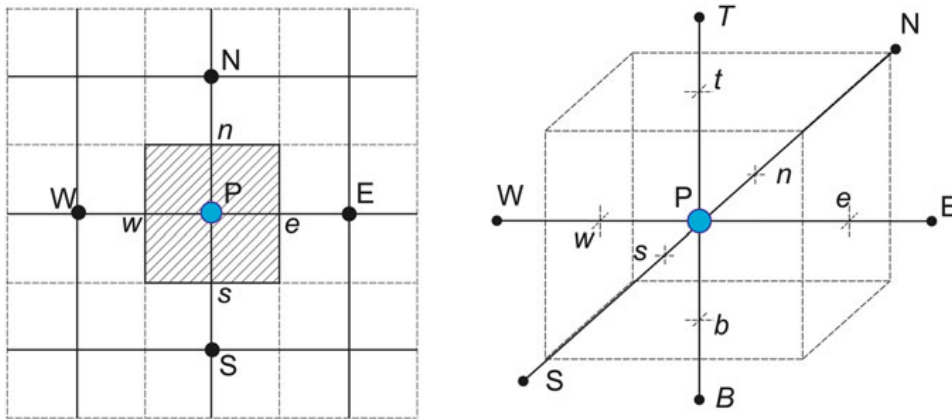


Figure 4.4.: Stencil for 2D & 3D FVM.

A series of assumptions must be employed in order to yield a simplified discretized form of the transport equation. The transport equation is defined earlier in Eq. (3.15) in differential form, but will be stated again for a more clear view in this section.

$$\frac{\partial(\rho\phi)}{\partial t} + \nabla \cdot (\rho\phi u) = \nabla \cdot (\Gamma\nabla\phi) + S_\phi \quad (4.18)$$

Applying steady-state conditions, three-dimensions in space and incompressible flow yields:

$$\nabla \cdot (\rho\phi u) = \nabla \cdot (\Gamma\nabla\phi) + S_\phi \quad (4.19)$$

Applying a CV integration which is necessary for the FVM formulation yields:

$$\int_{CV} \nabla \cdot (\rho \phi u) dV = \int_{CV} \nabla \cdot (\Gamma \nabla \phi) dV + \int_{CV} S_\phi dV \quad (4.20)$$

Applying the Divergence Theorem for the volume yields:

$$\begin{aligned} \int_{\Delta V} \frac{\partial}{\partial x} (\rho \phi u) dV + \int_{\Delta V} \frac{\partial}{\partial y} (\rho \phi u) dV + \int_{\Delta V} \frac{\partial}{\partial z} (\rho \phi u) dV = \\ \int_{\Delta V} \frac{\partial}{\partial x} \left( \Gamma \frac{\partial \phi}{\partial x} \right) dV + \int_{\Delta V} \frac{\partial}{\partial y} \left( \Gamma \frac{\partial \phi}{\partial y} \right) dV + \int_{\Delta V} \frac{\partial}{\partial z} \left( \Gamma \frac{\partial \phi}{\partial z} \right) dV + \int_{\Delta V} S_\phi dV \end{aligned} \quad (4.21)$$

, where  $dV = \delta x \delta y \delta z$  is the control volume, respectively.

Applying the stencil for the fluxes around the control volume yields:

$$\begin{aligned} [(\rho UA \phi)_e - (\rho UA \phi)_w] + [(\rho UA \phi)_n - (\rho UA \phi)_s] + [(\rho UA \phi)_t - (\rho UA \phi)_b] = \\ \left[ \left( \Gamma A \frac{\partial \phi}{\partial x} \right)_e - \left( \Gamma A \frac{\partial \phi}{\partial x} \right)_w \right] + \left[ \left( \Gamma A \frac{\partial \phi}{\partial y} \right)_n - \left( \Gamma A \frac{\partial \phi}{\partial y} \right)_s \right] + \left[ \left( \Gamma A \frac{\partial \phi}{\partial z} \right)_t - \left( \Gamma A \frac{\partial \phi}{\partial z} \right)_b \right] + \end{aligned} \quad (4.22)$$

$\bar{\Delta V}$

### Defining Discretization Schemes in the CV

Table 4.1.: Difference scheme for face values for nodal points.

Difference Scheme at Faces	x-direction	$\phi_e = \phi_E - \phi_P$	$\phi_w = \phi_P - \phi_W$
	y-direction	$\phi_n = \phi_N - \phi_P$	$\phi_s = \phi_P - \phi_S$
	z-direction	$\phi_t = \phi_T - \phi_P$	$\phi_b = \phi_P - \phi_B$

Table 4.2.: Convective Fluxes.

Convective Fluxes	x-direction	$F_e = (\rho UA)_e$	$F_w = (\rho UA)_w$
	y-direction	$F_n = (\rho UA)_n$	$F_s = (\rho UA)_s$
	z-direction	$F_t = (\rho UA)_t$	$F_b = (\rho UA)_b$



Table 4.3.: Difference Scheme for Fluxes at faces for nodal points.

Differencing Scheme of Fluxes	x-direction	$\left(\frac{\partial\phi}{\partial x}\right)_e = \frac{\phi_E - \phi_P}{\delta x_{PE}}$	$\left(\frac{\partial\phi}{\partial x}\right)_w = \frac{\phi_P - \phi_W}{\delta x_{WP}}$
	y-direction	$\left(\frac{\partial\phi}{\partial y}\right)_n = \frac{\phi_N - \phi_P}{\delta y_{PN}}$	$\left(\frac{\partial\phi}{\partial y}\right)_s = \frac{\phi_P - \phi_S}{\delta y_{SP}}$
	z-direction	$\left(\frac{\partial\phi}{\partial z}\right)_t = \frac{\phi_T - \phi_P}{\delta z_{PT}}$	$\left(\frac{\partial\phi}{\partial z}\right)_b = \frac{\phi_P - \phi_B}{\delta z_{BP}}$

Table 4.4.: Diffusive Fluxes.

Diffusive Fluxes	x-direction	$D_e = \frac{\Gamma_e A_e}{\delta x_{PE}}$	$D_w = \frac{\Gamma_w A_w}{\delta x_{WP}}$
	y-direction	$D_n = \frac{\Gamma_n A_n}{\delta y_{PN}}$	$D_s = \frac{\Gamma_s A_s}{\delta y_{SP}}$
	z-direction	$D_t = \frac{\Gamma_t A_t}{\delta z_{PT}}$	$D_b = \frac{\Gamma_b A_b}{\delta z_{BP}}$

The source term can be discretized as:

$$\bar{S}\Delta V = S_u + S_\phi\phi_P \quad (4.23)$$

Now that the fluxes have been defined with a numerical scheme, these relationships can be inserted in eq.(4.22) which yields:

$$\begin{aligned} & [F_e(\phi_E - \phi_P) - F_w(\phi_P - \phi_W)] + [F_n(\phi_N - \phi_P) - F_s(\phi_P - \phi_S)] + \\ & [F_t(\phi_T - \phi_P) - F_b(\phi_P - \phi_B)] = [D_e(\phi_E - \phi_P) + D_w(\phi_P - \phi_W)] + \\ & [D_n(\phi_N - \phi_P) + D_s(\phi_P - \phi_S)] + [D_t(\phi_T - \phi_P) + D_b(\phi_P - \phi_B)] + \\ & S_u + S_\phi\phi_P \end{aligned} \quad (4.24)$$

Rearranging the terms gives:

$$\begin{aligned} & [(D_e + D_w + D_n + D_s + D_t + D_b) - (F_e + F_w + F_n + F_s + F_t + F_b) - S_\phi] \phi_P \\ & = (D_e - F_e) \phi_E + (D_w - F_w) \phi_W + (D_n - F_n) \phi_N + \\ & (D_s - F_s) \phi_S + (D_t - F_t) \phi_T + (D_b - F_b) \phi_B + S_u \end{aligned} \quad (4.25)$$

This can be written into:

$$a_P\phi_P = a_E\phi_E + a_W\phi_W + a_N\phi_N + a_S\phi_S + a_T\phi_T + a_B\phi_B + S_u \quad (4.26)$$

, where the coefficients are given in the table 4.5.

Table 4.5.: Coefficients

$a_P$	$(D_e + D_w + D_n + D_s + D_t + D_b) - (F_e + F_w + F_n + F_s + F_t + F_b) - S_\phi$
$a_E$	$D_e - F_e$
$a_W$	$D_w - F_w$
$a_N$	$D_n - F_n$
$a_S$	$D_s - F_s$
$a_T$	$D_t - F_t$
$a_B$	$D_b - F_b$

In a more compact form:

$$a_P\phi_P = \sum a_{nb}\phi_{nb} + S_u \quad (4.27)$$

, where  $nb$  denotes the neighbouring points of the node of interest,  $P$ .

Equation (4.27) is a useful, compact version of the general transport equation, which forms the basis for the solution of equations. A general description of the solution algorithms for solving the transport equation will be discussed in Section. 4.6.

## 4.4. Implementation of Boundary Conditions

For all problems solved with CFD, the physics of interests are initialized and calculated with respect to the boundary and initial conditions. The process of solving flow problems is essentially the extrapolation of dataset defined at the boundaries into the interior domain. Therefore, it is of importance to understand and specify suitable conditions for physical realistic solutions and well-posed boundary conditions. The conditions highly affect the numerical analysis and solution. One of the main causes of rapid convergence for CFD simulations is appropriate boundary conditions [15]. For transient calculations, the initializing data of all flow variables are needed at all cells in the computational domain. This involves no more special measures than initialization of the data arrays in the CFD code, and will not be discussed further.

This section will present a brief description of the implementation in the discretized equations for FVM, with common boundary conditions. It can be noted that these specific boundary conditions are implemented for the simulations performed in this thesis. These are:

- Inlet
- Outlet
- Wall
- Symmetry

It can be mentioned that these specific boundary conditions, which is to be discussed, are implemented for the simulations for this thesis. Other problem specific boundary conditions such as moving walls, periodic or cyclic boundary conditions are not discussed further.

When constructing the staggered grid arrangement, discussed in sec. 4.7.1, additional nodes are specified around the physical boundary. Calculations are performed for internal cells, not accounting the set boundary. There are two notable arrangements. Firstly, physical boundaries which coincide with CV boundaries, and secondly, cells adjacent to the inlet outside the domain for inlet condition storage. These are also known as *ghost points* [49]. By utilizing this technique enables implementation of boundary conditions with minor modifications to the discretized equations near the inlet. An illustration of an example of the grid

#### 4.4. IMPLEMENTATION OF BOUNDARY CONDITIONS

---

arrangement and physical boundaries can be seen in Fig. 4.5.

For cells at the boundary, it can be shown that  $a_p$  and  $a_nb$  can be neglected. Thus, the discretized equations effectively reduce to:

$$\phi_p = \phi_{fix} \quad (4.28)$$

, which sets a fixed value at  $P$  for the transport quantity  $\phi$ .

Additionally, by setting the value of a variable of interest for the internal cells, the treatment is useful in dealing with obstacles in the domain by fixing  $\phi_{fix} = 0$ , or any other specified value, at the cells for the obstacle region. Thus, the system of discretized equations which deals with obstacles can be solved without any special treatment.

For further discussion around the boundary conditions and implementation in the discretized equations, 2D, subsonic flow, hybrid differencing method and SIMPLE solution algorithm will be assumed. This will enable a more relevant general description of the implementation.

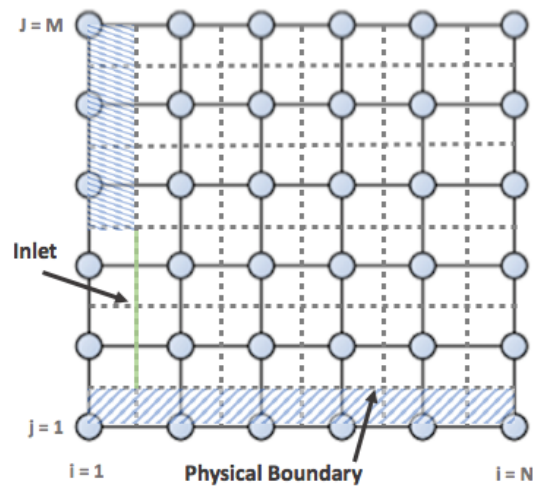


Figure 4.5.: Grid arrangement at boundaries, where the dotted lines represents the boundaries for the cells.

## Inlet Boundary Conditions

The distribution of flow variables required to be set at the inlet boundaries As previously mentioned, the grid extends outside the physical boundary. The nodes along the inlet, line(s) for 2D or face(s) for 3D, are used to store the inlet values of flow variables. An illustration of how the different velocities are treated in the mesh can be seen in Fig. 4.6.

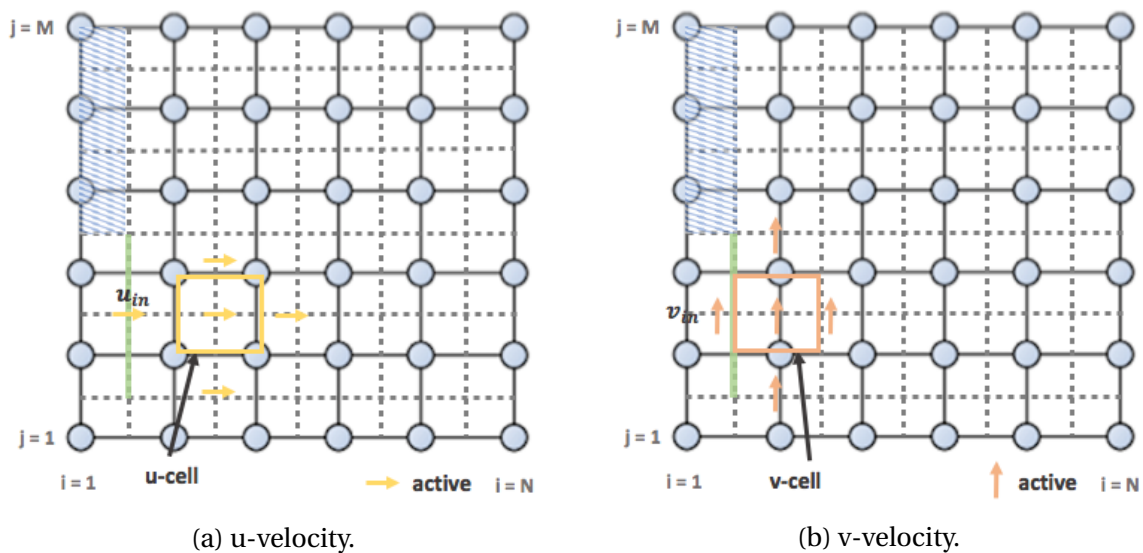


Figure 4.6.:  $u$ - and  $v$ -velocities at the inlet boundary

The pressure field is obtained during pressure correction calculation, which does not yield absolute pressure (Patankar, 1980). Therefore, fixing the absolute pressure at inlet nodes, and performing pressure correction at the respective cells is common practice. By specifying the reference value in advance, the absolute pressure field can be acquired. An example of how this is done for a simple grid is shown in Fig. 4.7.

#### 4.4. IMPLEMENTATION OF BOUNDARY CONDITIONS

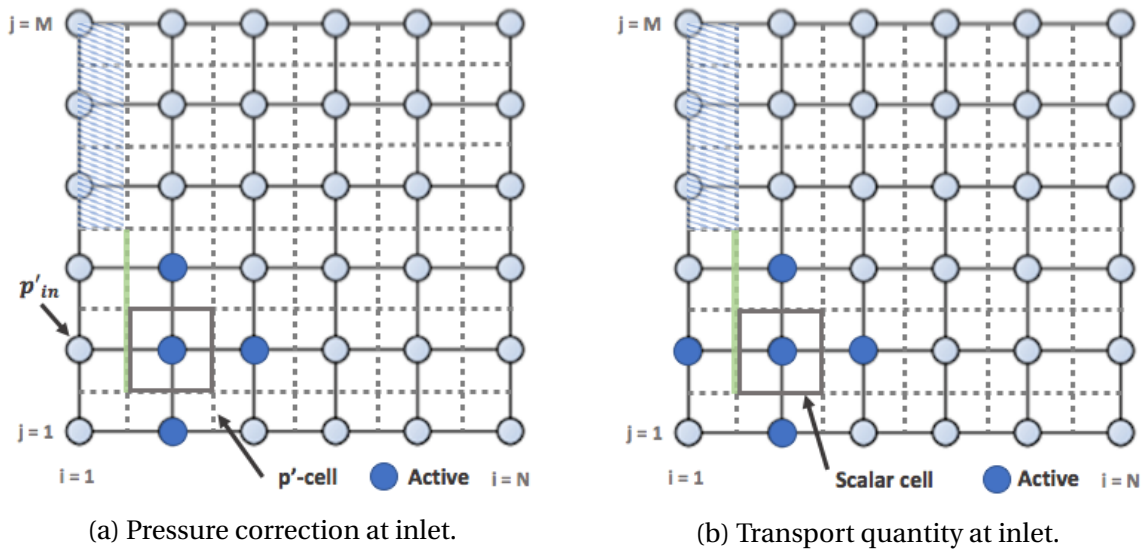


Figure 4.7.: Pressure correction cell and scalar cell at inlet boundary.

#### Outlet Boundary Conditions

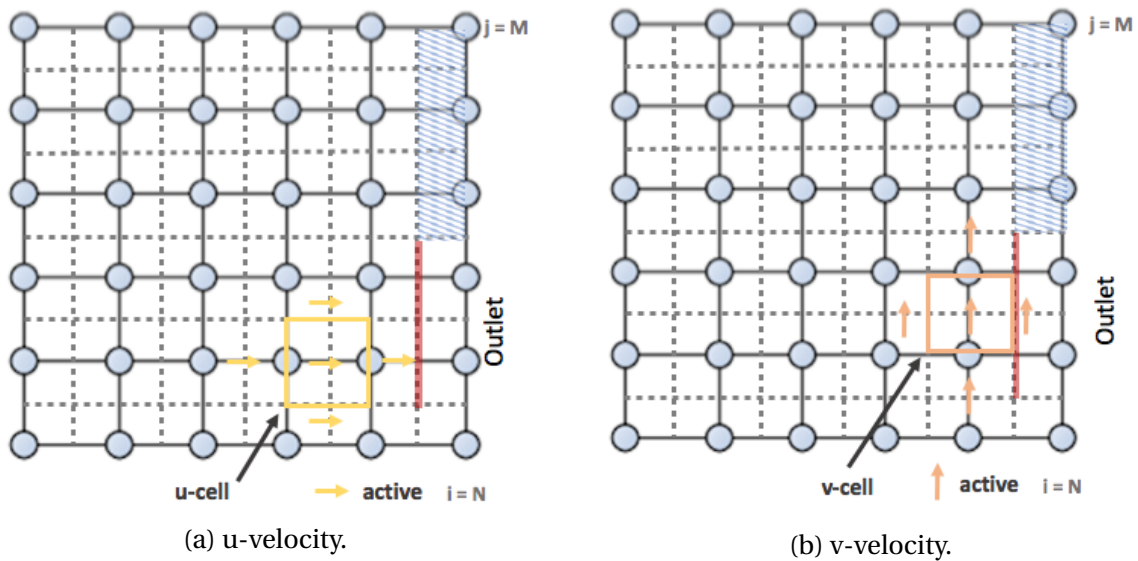


Figure 4.8.:  $u$ - and  $v$ -velocities at the outlet boundary.

Outlet boundary conditions are often applied in conjunction with inlet boundary conditions. The location of an outlet should be sufficiently away from any geometries which may disturb the flow, such that the flow field can reach a fully developed state. The result of this is that there occurs no change in the flow direction before the flow exits through the outlet. As a result, this enables the possibility to select the outlet perpendicular to the flow directions

and let the gradients in the direction normal to the outlet equal to zero [15]. The way the velocity components, pressure-correction, and scalar values are treated can be seen in Fig. 4.8 and Fig. 4.9.

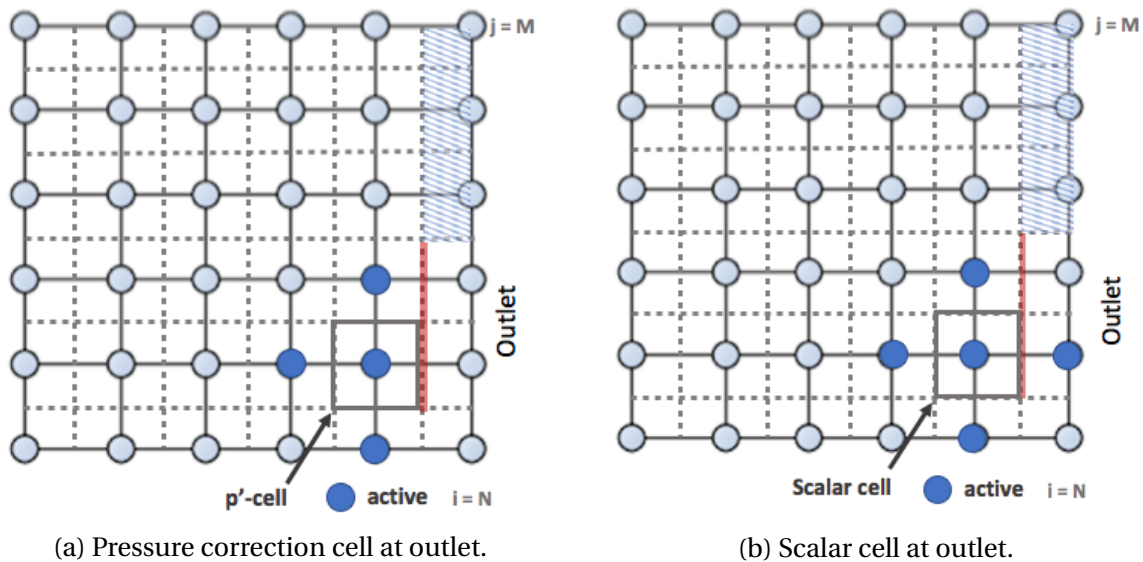


Figure 4.9.: Pressure correction cell and scalar cell at outlet boundary.

## Wall Boundary Conditions

Wall boundary conditions are commonly utilized in confined physical flow problems, which arises for many applications. For the velocity components adjacent to the wall, a no-slip condition is the most fitting condition. For the cells adjacent to the wall, the node at the wall-face is set to be equal to zero. This is represented in Fig. 4.10. Thus, the discretized transport equation for momentum regarding wall treatment can be evaluated without specifying modifications. Furthermore, since the wall necessary are dictated by the no-slip condition, pressure correction is not performed at the wall, seen in Fig. 4.11.

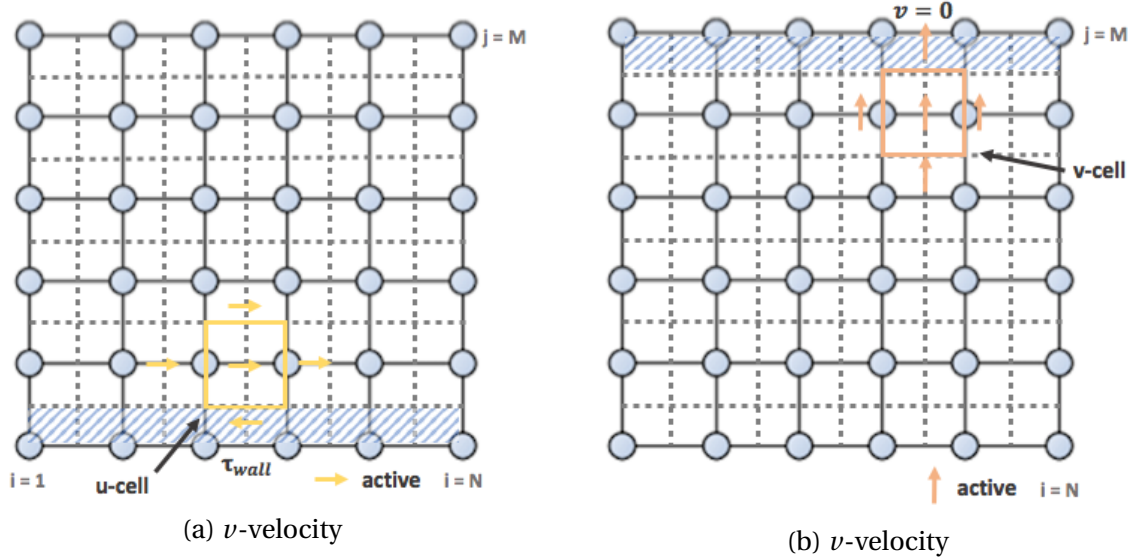


Figure 4.10.:  $u$ - and  $v$ -velocities at the wall boundary.

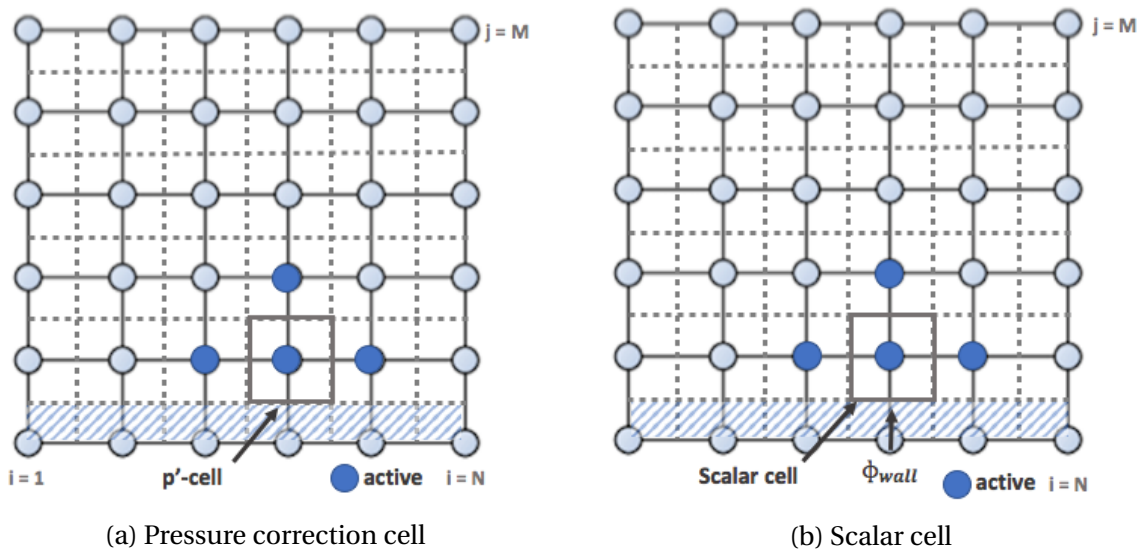


Figure 4.11.: Pressure correction cell and scalar cell at wall boundary.

### Symmetry Boundary Conditions

Symmetry boundary conditions are utilized if there exists geometrical symmetry for the geometry. At the symmetry boundary, no flow is crossed and the scalar flux at the boundary is zero. For CFD implementation, due to the scalar flux being zero, the normal velocities are also zero, and the values outside of the domain next to the symmetry boundary are equated to the values for the adjacent cell inside the domain. Assuming that  $J$  is the symmetry bound-



ary, the transport quantity  $\phi$ , the previously stated property can be shown as:

$$\phi_{\text{symmetry boundary},J} = \phi_{\text{neighboring nodes},J} \quad (4.29)$$

For the pressure correction, the link between the symmetry boundary is performed by setting the coefficient to zero, resulting in no modifications of the discretized pressure correction equation.

#### 4.4.1. Best-Practise CFD Implementation of Boundary Conditions

Due to the fact that poorly defined boundary conditions may have a significant impact on the solution, specifying appropriate boundary conditions related to the physical problem at hand is of importance. Therefore, there exist various guidelines for boundary implementation for CFD purposes which one should be aware of. Some guidelines may be:

- *Inflow and outflow boundaries*

The location of the inflow and outflow boundaries should have the flow entering or leaving normal to the boundaries. This may lead to better convergence.

- *Gradients near a boundary*

Observation of large gradient normal to a boundary indicates an incorrect setup, and the boundary should be moved further upstream/downstream away from the gradients.

- *Mesh near the boundary*

For the mesh, the cells near the boundary should not have high skewness, a mesh metric discussed in Sec. 5.2. Error from high skewness will propagate through the rest of the flow domain.

For chosen boundary conditions, there exists arrangements which lead to a well-posed boundary specification [39]. This may also be the range with robustness. The most robust inlet/outlet boundary arrangement is the velocity inlet and pressure outlet arrangement. The flow is driven by the velocity depending on the inlet conditions set, with a static pressure outlet (velocity inlet/pressure outlet). The inlet total pressure is an implicit result of the pre-

diction. A robust inlet/outlet configuration is the mass flow inlet with a static pressure at the outlet (pressure outlet). The total pressure of at the inlet is adjusted by the specified mass flow. A less robust, but which can yield satisfying robustness is by specifying boundary condition of total pressure at the inlet, with a static pressure at the outlet (pressure inlet/pressure outlet). By utilizing these conditions, the mass flow of the system will be part of the solution, which can be used as a measure of accuracy and convergence criteria. The downside with this configuration it that is is highly sensitive to the initial guess. Inaccurate initial guesses may lead to unphysical results.

There have been presented three well-posed boundary arrangements, but there also exists arrangements which is unreliable. One of these is specifying total pressure or mass flow rate at the inlet with an outflow boundary outlet. This can either be pressure inlet/ outflow or mass flow inlet with outflow. These combinations should be avoided because the static pressure will vary depending on the solution, hence it is not fixed. Although, if it is desired to apply mass flow inlet and outflow configuration for incompressible flow, it can be used since it is less pressure sensitive. The last unreliable arrangement is applying a velocity inlet and velocity outlet for the domain. This system will be highly numerically unstable due to the way the driving forces are implemented [50].

## 4.5. Solution of System of Equations

The discretized equation, as seen in Eq. (4.27), must be arranged for cells in the computational domain in order to perform simulations. For CVs adjacent to the domain boundaries, modifications are performed to the general discretized equation, Eq. (4.27), in order to include the boundary conditions. The resulting system of equations is then solved to obtain the distribution of property  $\phi$  [15].

The discretization using the FVM leads to a sparse linear system of equations, given that the diffusion coefficient is independent of  $\phi$ . This yields a corresponding matrix with seven diagonals or a heptadiagonal matrix.

To obtain the solution for the system of equations, a finite mesh must first be defined. When the computational domain is defined, discretization over the domain yields one equation for each node. Represented in a general form, the matrix which is to be solved may be expressed as:

$$Ax = b \tag{4.30}$$

The general transport equation will be on the form:

$$A\phi = S_u \tag{4.31}$$

, where A is the coefficient matrix,  $A = \{a_B, a_S, a_W, a_P, a_E, a_N, a_T\}$ .



## 4.6. Solution of Discretized Equations

Discretization of the governing fluid equations results in a system of equations, shown in Section. 4.2. The size and complexity of system depending on the number of grid points as well as discretizations used. The first dictates the number of equations needed to be solved, where the latter affect the number of mathematical operations required for the sub-routines. For solving matrices, any desired procedure is valid for solving the algebraic equations. But the main constraint is the computational resources available.

There exist two families of solution techniques for solving linear algebraic equations, that is:

- Direct Methods
- In-direct Methods (Iterative Methods)

Iterative methods are general-purpose algorithms that are easily implementable in CFD code, but their convergence rate can be slow if the system of equations is large. Historically, they were not considered suitable for general-purpose CFD procedures. However, more recently multigrid techniques have been developed that have improved convergence rates of iterative solvers to an extent that they now are the method of choice in commercial CFD codes.

Due to the statements stated above, the focus will be on iterative methods. Furthermore, the method of interest will be on *Gauss-Seidel* iteration in conjunction with *relaxation methods*, due to their properties. Additionally, it is the techniques utilized for the solver algorithm implemented in this thesis.

### Gauss-Seidel Iteration Method

The Gauss-Seidel method also referred to as Liebmann method or method of successive displacement, is developed by Gauss and von Seidel. The method is similar to the well known *Jacobi method*. The method is applicable for all matrices which have non-zero diagonal elements, and convergence is achieved if the system is diagonally dominant. As discussed in Section. 4.3 as seen in the matrix. 4.32, the coefficient matrix obtained from the discretized

equations fulfills the requirements of the Gauss-Seidel method. Generalized, the iteration equation for the Gauss-Seidel method can be expressed as:

$$x_i^{(k)} = \sum_{j=1}^n \left( \frac{a_{ij}}{a_{ii}} \right) x_j^{(k)} + \sum_{j=1+1}^n \left( \frac{a_{ij}}{a_{ii}} \right) x_j^{(k-1)} + \frac{b_i}{a_{ii}} \quad (4.33)$$

In matrix form:

$$\mathbf{x}^{(k)} = \mathbf{T}_1 + \mathbf{T}_2 \mathbf{x}^{(k-1)} + \mathbf{c} \quad (4.34)$$

A few main benefits of the Gauss-Seidel method is that data storage and convergence. During treatment of elements, a storage vector is required such that each element can be overwritten during the computation. In other words, the Gauss-Seidel requires less memory to store the data, which is advantageous for a larger computational mesh. Ralston and Rabinowitz (1978) note that the convergence rate of Gauss-Seidel faster, compared with the Jacobi method [15]. On the contrary, convergence is never guaranteed, since there exist many factors which may contribute to diverging solutions. Rapaport et al. have shown that Gauss-Seidel, and iterative methods in general, has convergence issues even though the problem may be well-posed [51].

### Relaxation Methods

The rate of convergence for the Gauss-Seidel method depends on the properties of the coefficient matrix. It can be shown that an improvement of the iteration method is achieved by implementing a relaxation parameter,  $\alpha$ , using methods known as *relaxation method* for the solution of the system of equations.

The relaxation method modifies the convergence rate of iteration sequences by multiplying second- and third-order terms by  $\alpha$ . Implemented for a solution method, the following form

is obtained:

$$x_i^{(k)} = x_i^{(k-1)} + \alpha \left[ \sum_{j=1}^n \left( \frac{a_{ij}}{a_{ii}} \right) x_j^{(k-1)} + \frac{b_i}{a_{ii}} \right] \quad (i = 1, 2, \dots, n) \quad (4.35)$$

The main technique is varying the relaxation factor to yield different iteration sequences. If relaxation factor of  $0 < \alpha < 1$  is implemented, the procedure is called and *under-relaxation method*. If relaxation factor of  $\alpha > 1$ , the procedure is called an *over-relaxation method*.

In general, utilizing the over-relaxation method can increase the convergence rate, as the smaller order terms will have a greater impact on the iteration procedure at the cost of higher numerical residuals, whereas utilizing the under-relaxation method will increase the accuracy, but with reduced convergence rate. Thus, the selection of relaxation factor  $\alpha$  will affect simulation time, as well as the numerical accuracy.

The residual,  $r_i^{(k)}$ , after  $i$ th equation after  $k$  iterations be expressed as the following for the iteration sequence:

$$r_i^{(k)} = b_i - \sum_{j=1}^n a_{ij} x_j^{(k)} \quad (i = 1, 2, \dots, n) \quad (4.36)$$

It can be shown that the expression inside the square bracket of Eq. (4.35) is the residual vector after  $k - 1$  iterations. Thus, resulting in the iteration sequence which may be given by:

$$x_i^{(k)} = x_i^{(k-1)} + \alpha \left[ \frac{r_i^{(k-1)}}{a_{ii}} \right] \quad (i = 1, 2, \dots, n) \quad (4.37)$$

It can be shown that the relaxation parameter,  $\alpha$ , does not affect the converged solution, as it is not an independent of the residuals. This also suggests that the relaxation method may be advantageous if an optimum value of the relaxation factor is found and chosen, to minimize the number of iterations required to reach the converged solution.

By utilizing the relaxation parameter in the iteration sequence, the computational time can

be reduced. But it has to be noted that finding the optimum value of  $\alpha$  for a given problem may be problematic and is dependent on the computational grid. Thus, giving a precise guidance for the value is difficult to achieve. Nevertheless, it is in principle possible to select suitable values of the relaxation factor, which yields faster convergence for the solution. There exist other methods which use the properties of relaxation method, such as the *successive over-relaxation* technique.



## 4.7. Solver-Algorithms for Pressure-Velocity Coupling

Convection effects of a transport property,  $\phi$ , depends solely on the direction and magnitude of the velocity field. In general, the velocity field is unknown and emerges as a part of the solution along with auxiliary variables of the flow. Different strategies exist for obtaining the unknown variables for attaining information of the entire flow field [15]. The focus will be on a segregated flow, where the pressure-velocity coupling is utilized.

### 4.7.1. Pressure-Velocity Coupling

For segregated flow modelling, the pressure-velocity coupling is performed by using the discretized equation of continuity, eq. (4.11) to derive a supplementary condition for the pressure term, by reformatting the equation. For the software used, the pressure-velocity algorithms of *SIMPLE*, *SIMPLEC*, and *PISO* are available [11]. These are based on a predictor-corrector approach, will be discussed.

#### Staggered Grid

Discretization of the flow domain for the transport equations in a conventional way yields a problem regarding storing of information. If the pressure, velocity or other flow variables are stored in the same location, this is known as a *Collocated grid*, described by Rhie and Chow (1983) [52]. If velocities and pressure are defined at the same node, a phenomenon can occur where a highly non-uniform pressure field can act as uniform pressure field. This shortcoming can be described as numerical-smearing-error due to the spatial domain discretization.

A solution for the numerical error was introduced by Harlow & Welch (1965) by introducing a *staggered grid* with a method known as Marker-And-Cell (MAC) method [53]. This concept is to evaluate scalar variables at cell-center, but for the velocity components on a staggered grid centered around the cell faces. This can be viewed as a shifting of the grid when computing the velocities. The effect of *staggering*, results in bypassing the non-physical behaviour of spatially oscillating pressures. An advantage of this technique is that the shift of location for

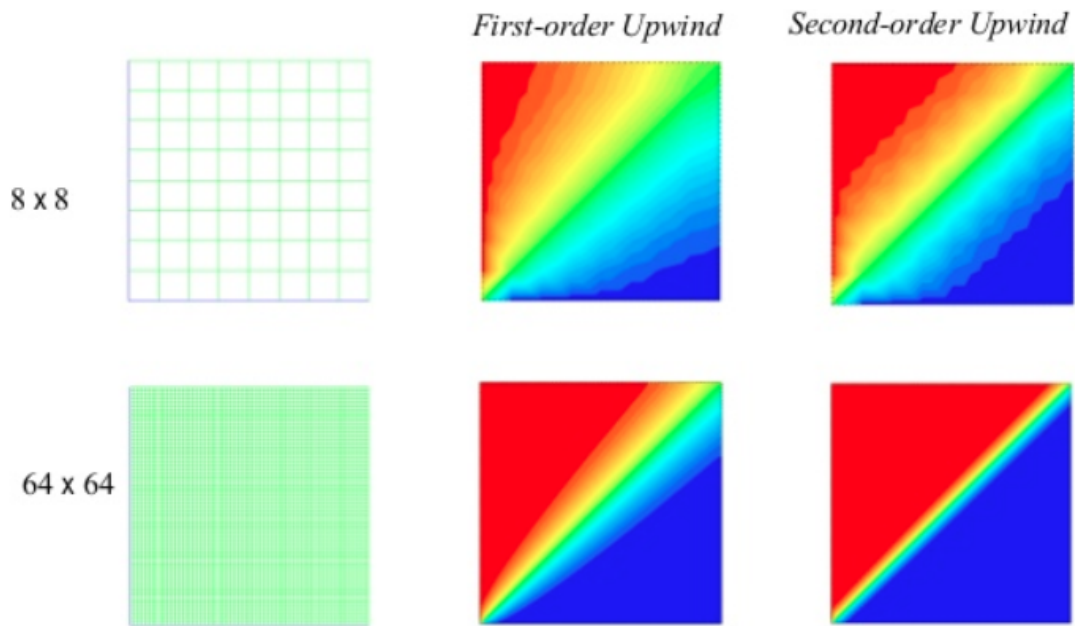


Figure 4.12.: Numerical diffusion for the classical example on flow with misaligned grid, for first- and second-order upwind [13].

computing a velocity in a direction requires the computations of the transport properties. Thus, no interpolation is needed at the cell faces, since the information can be extracted directly. This is previously illustrated during the discussion of boundary conditions, in Section. 4.4.

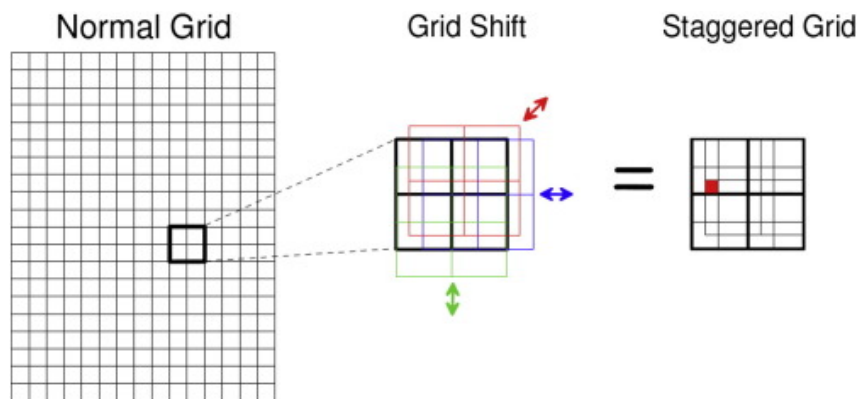


Figure 4.13.: Presentation of the staggered grid concept introduced by Harlow & Welch (1965) [14].

### 4.7.2. SIMPLE Algorithm

The *Semi-Implicit Method for Pressure-Linked Equations*, better known under the acronym *SIMPLE*, is an algorithm which was originally presented by Patankar and Spalding (1972) [54]. SIMPLE is, in essence, a solver which uses a guess-and-correct-methodology for calculating the pressure on a staggered grid [15]. The SIMPLE-algorithm is a segregated algorithm, meaning that the discretized equations are solved sequentially. This decoupling is a characteristic of segregated algorithms, where the counter-part are coupled algorithms, which solves the system of momentum and pressure-based continuity equations simultaneously.

The SIMPLE algorithm is based on a relationship between pressure- and velocity-correction, where mass conservation is employed to obtain the pressure field. The momentum equation is solved using a guessed pressure field,  $p^*$ , and resulting flux computed from the discretized continuity equation, Eq. (4.11). This yields an expression for continuity, with the guessed pressure field, which may be expressed as [11]:

$$J'_f = d_f(p'_{c0} - p'_{c1}) \quad (4.38)$$

, where  $p'_{c0}$  and  $p'_{c1}$  is the corrected pressure in cell 0 and 1, and the flux at the cell boundary is corrected with the following:

$$J_f = J_f^* + J'_f \quad (4.39)$$

, where  $J_f$  is the corrected flux,  $J'_f$  the correction of flux and  $J_f^*$  the guessed flux.

The corrected pressure  $p'$ , is calculated with the discretized transport equation, eq. 3.3, which may be expressed as:

$$a_p p' = \sum_{nb} a_{nb} p'_{nb} + S_{p'} \quad (4.40)$$

, where  $S_{p'}$  is the net flow rate into a cell, given by:

$$S_{p'} = \sum_f^N J_f^* A_f \quad (4.41)$$

, which is obtained by the guessed continuity equation.

The pressure-corrected equation can be solved by using a multigrid method to reduce computational time for the intermediate iterations. When the solution is obtained, the pressure in the cell can be calculated by:

$$p = p^* + \alpha_p p' \quad (4.42)$$

, where  $\alpha_p$  is the under-relaxation factor for pressure, using the relaxation method described in Section. 4.6.

The corrected flux through a cell,  $J_f$ , is obtained since the corrected pressure have been computed, such that:

$$J_f = J_f^* + d_f(p'_{c0} - p'_{c1}) \quad (4.43)$$

It can be shown that the velocity-correction equations are similar to that of pressure correcting, substituting the calculated, guessed and corrected quantity with velocity-component in an arbitrary direction. In Fig. A.32, complete algorithm can be visualized.

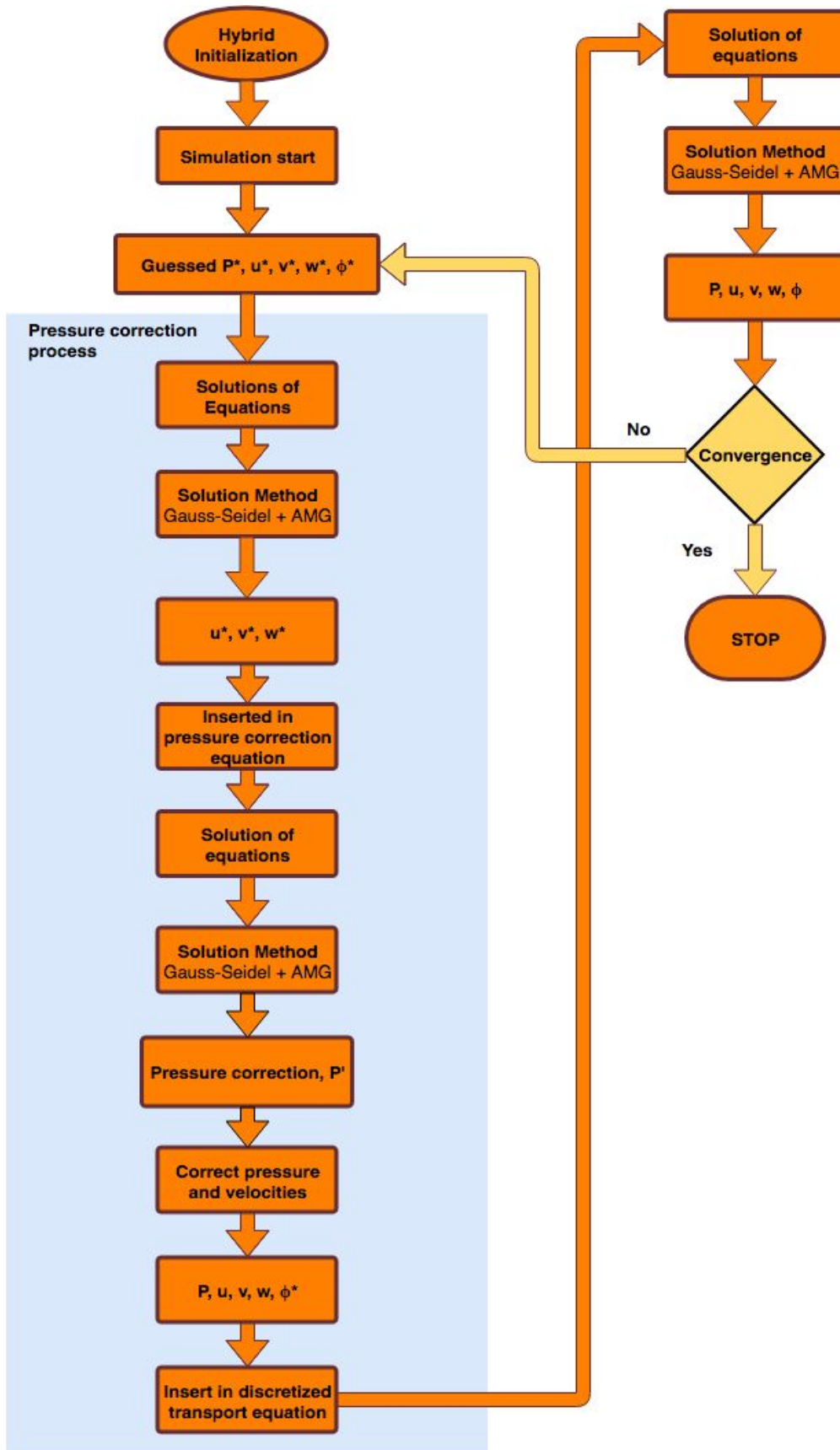


Figure 4.14.: Schematic of the modified solver process for SIMPLE.

# Computational Domain

---

This chapter contains a review of modern methodologies for generating computational domains. In the following, principles for grid generation will be introduced, which are widely accepted and applied for in the realm of CFD, with the main focus on applications for commercial CFD software. Principles related to expanded research, techniques and discussion will be excluded in this thesis.

Acquiring satisfactory mesh is of utmost importance, due to the fact that the computational grid forms the basis for which the discretized equations in the flow domain will be solved. This implies that being aware of mesh behaviour and its effects on important factors such as convergence, accuracy, computational time and more importantly, obtaining a satisfactory physical solution are essential fundamental knowledge for any CFD user. At the end of the chapter, an assessment of the data structure which is implemented into *Fluent* will be addressed.

## 5.1. Grid Structure

### Classification of Grids

All types of grid structures can be divided into two main groups, that is structured and unstructured mesh. Based on connectivity, the cells are connected to each other, in an ordered or unordered manner, which can be shaped to any geometry for analysis.

For structured grids, the cells and nodes are ordered and connected in a structured man-

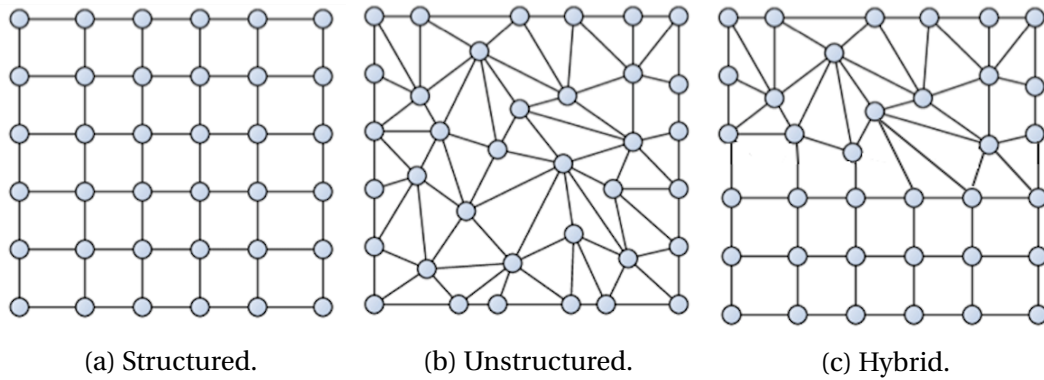


Figure 5.1.: Classifications of grids.

ner. Normally with equidistant spacings, but also for unequal spacings if one is to refine the grid spacings in any arbitrary direction. For unstructured grids, any arbitrary geometrical shape which is identified by an irregular connectivity. Compared to structured grids, this model is less space efficient and calls for a higher explicit storage of neighbouring cells. For some cases, a combination of structured and unstructured grids denoted as a hybrid grid. This mesh configuration is commonly used for complex geometries or multi-body analysis, requiring both classes of mesh structures. The classifications of a grid can be seen in Fig. 5.1.

### Type of Cell-Shapes

For grid generation, there exist three major classes of grids. These are triangular(tri), quadrilateral(quad) and polygonal(poly) grids. Tri and quad are the most used types for both 2D and 3D problems. Furthermore, utilizing both tri and quad common practice, especially for capturing the physical boundary of geometries the flow behaviour, such as boundary layers. In recent years, due to the development of meshing technology polygonal and polyhedral mesh [55]. A table summarizing the different cell-shapes are listed in Tab. 5.1.

Table 5.1.: Classes of Cell-Shapes.

Cell Classes	2D	3D
Triangular	Triangle	Tetrahedron Pyramid Prism
Quadrilateral	Quad	Hexahedron
Polygonal	Polygonal	Polyhedral

### Terminology

For mesh generation and mesh control in a meshing environment, there exist various ways of handling the computational domain at hand. For proper mesh control, several terminologies must be understood, since this forms basis during meshing operations. These are:

- Cell: Control volume into which the domain consists of
- Node: Gridpoint
- Cell Center: Center of a cell
- Edge: Boundary of a face
- Face: Boundary of a cell
- Zone: Grouping of nodes, faces and cells
- Domain: Group of node, face and cell zones

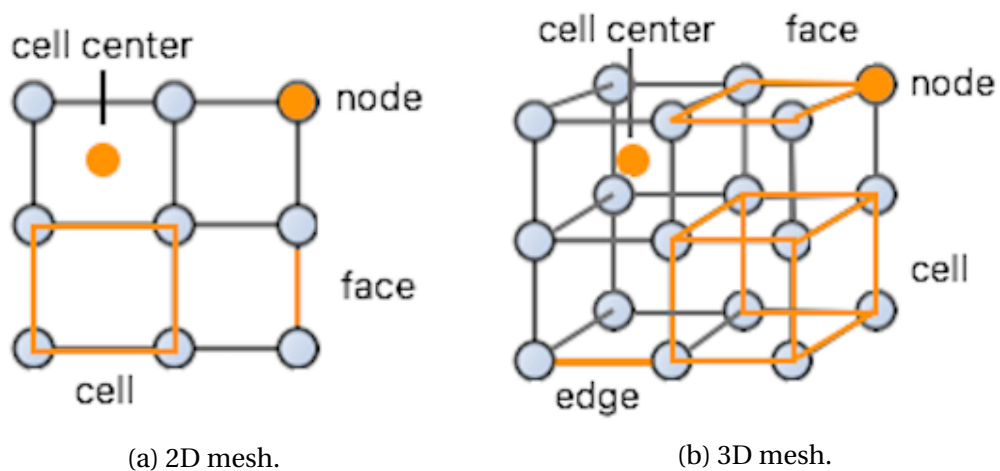


Figure 5.2.: Mesh Terminology for 2D and 3D mesh.



## 5.2. Mesh Metric and Mesh Quality

There exist various ways of quantifying the quality of the mesh during grid generation. For CFD applications, are some parameters which are commonly used as mesh metric for evaluating mesh quality [56]. These parameters are geometrical considerations and will be further explained.

### Skewness

Skewness is a metric to evaluate the optimal size of a cell. For skewness, there are two methods for mesh analysis. That is based on equilateral volume or based on deviation from a normalized equilateral angle.

The first can be mathematically expressed as:

$$Skewnesss = \frac{Optimal\ Cell-size - Cell-size}{Optimal\ Cell-size} \quad (5.1)$$

Quantifying the quality of equilateral volume applies only to triangles and tetrahedrons, and is the default method for tri- and tet-mesh.

The skewness based on deviation from a normalized equilateral angle can be expressed as:

$$Skewness = \max \left[ \frac{\theta_{max} - 90}{90}, \frac{90 - \theta_{min}}{90} \right] \quad (5.2)$$

Applies to all cell and face shapes. Always used for prisms and pyramids.

The most common measure of quality is based on equiangle skewness, which is defined:

$$\max \left[ \frac{\theta_{max} - \theta_e}{180 - \theta_e}, \frac{\theta_e - \theta_{min}}{\theta_e} \right] \quad (5.3)$$

, where:

- $\theta_{max}$  = Largest angle in a face or cell
- $\theta_{min}$  = Smallest angle in a face or cell
- $\theta_e$  = angle for equiangular face or cell (i.e 60 for triangle and 90 for square)

The range of the skewness parameter ranges from 0 to 1, where an idealized cell is equidistant, and consequently equiangular, gives an optimal skewness value. The counterpart is infinite thin cells giving high skewness values.

For large skewness, the accuracy will be compromised of the interpolated regions due to large jumps compared to the neighbouring cells. In addition, this can lead to numerical errors, affect the convergence rate and divergence.

### Orthogonality

Orthogonal quality (OQ) for cells is computed using the face normal vector, i.e the vector from the cell centroid to the cell centroid of all adjacent cells. The orthogonal quality for a cell is computed as the minimum of the following quantities for each face,  $i$ .

$$\frac{\vec{A}_i \cdot \vec{f}_i}{|\vec{A}_i| \cdot |\vec{f}_i|} \quad (5.4)$$

, where  $\vec{A}_i$  is the face normal vector and  $\vec{f}_i$  is the vector from the centroid to the adjacent cell that face and where:

$$\frac{\vec{A}_i \cdot \vec{c}_i}{|\vec{A}_i| \cdot |\vec{c}_i|} \quad (5.5)$$

, where  $\vec{c}_i$  is the vector from the cell-center to the adjacent cell that shares the face [11].

Orthogonal quality ranges from 0-1, where 1 is optimal for a cell and 0 is the worst.

### Aspect Ratio and Smoothness

The aspect ratio is defined as the ratio of the longest and the shortest edge of a cell. For an equidistant grid, this will be the optimum value of 1. Smoothness is defined as the change in

size during mesh transition. There should be no sudden jumps in size, which will cause erroneous results at the nearby cells. The aspect ratio may be a metric describing the smoothness of the mesh.

### Mesh-Type Selection for Grid Generation

Depending on the physical problem and the flow behaviour of interest, several cell-types and mesh configurations can form the computational domain. This discussion will only present the geometrical aspects of the mesh. Numerical considerations will be addressed in the next section.

If accuracy is of high priority, a hexahedral mesh is usually preferred. The mesh-density required for capturing all flow features, and if the geometry allows for it, hex cells should be the main cell-type in the domain. Although, the mesh-density should not be too high, capturing details of the flow which is not of interest. In presence of walls, the adjacent cells must be refined such that boundary layer effects can be resolved [57]. Quad, hex, and prism cells are preferred here due to the fact that the faces of the cells can be aligned in the normal direction from the wall and inwards into the domain [58]. Inside the domain in far proximity from wall and wall-effects, quad and hex cells can be generated. Aligning these cells to the flow will lead to the ability to capture flow effects in a better manner. This is justified due to improved of resolving transportation of physical quantities through the cells [59].

Utilizing the mesh-metrics discussed in Sec.5.2 is a useful basis for determining the quality of the mesh. For the orthogonal quality and skewness, there exist limits which should not be exceeded after grid generation. The critical factors for both metrics are the minimum orthogonal quality and maximum skewness. For a cell, high values for OQ and skewness results in an inadequate computational starting point and may lead to several problems with the simulation. For best-practice CFD implementation, the following mesh-metrics can be classified into different ranges of quality, seen in tab.5.2.

Table 5.2.: Mesh quality for the mesh metrics, orthogonal quality and skewness for grids [11].

	<b>Excellent</b>	<b>Very good</b>	<b>Good</b>	<b>Accept-able</b>	<b>Bad</b>	<b>Unaccept-able</b>
Min. OQ	0.95-1.0	0.7-0.95	0.2-0.69	0.15-0.20	0.001-0.14	0-0.001
Max. Skewness	0-0.25	0.5-0.8	0.5-0.8	0.80-0.95	0.95-0.97	0.98-1.0

To summarize the mesh-type and consideration regarding mesh quality, the following should be addressed:

- For a fixed mesh-density, hexahedral meshes that are aligned with the flow are preferred
- Mesh-density must be sufficiently high to capture all flow characteristics
- Mesh-density adjacent to walls must be sufficiently high to resolve boundary layer effects
- Achieving high mesh-quality using Tab.5.2 is advised.
- Mesh independence study should be performed to quantify mesh-density vs. simulation results

### 5.3. Grid Generation

Grid generation is defined as the process of dividing a physical domain into sub-domains, which consists of cells [60]. In recent times, mesh generation has become a topic of interesting research due to its wide application and influence in technology involving numerical simulation such as CAD, CFD-analysis, FEA-analysis [56]. A chart of the many various mesh generation techniques can be found in Fig.5.4. Further detail regarding techniques will not be discussed, as it is not a topic of interest of this thesis, but several techniques are applied for mesh generation for performing the simulations - later seen in Part.III.

### Importance of Grid Generation

In the following, a general description of why proper grid generation is important and how it affects important simulations aspects. The main topics of interests are:

- Physics of interest
- Solution accuracy
- Rate of convergence
- Computational time
- Grid independence

The main focus when performing grid generation is to ensure that the mesh will capture all flow physics. Not taking models (i.e turbulence, acoustics, etc) into account, the mesh should be discretized such that flow characteristics of interest are resolved. To ensure satisfactory solution accuracy a suitable mesh-density should be present for constructing the computational domain. Although solution accuracy is highly dependent on the models implementing for the physics, having a sufficiently resolved grid is of importance due to its influence on the numerical methods and simulation results.

It is previously stated that an acceptable mesh-density should be generated. However, the number of cells have an eminent impact on convergence rate, as it governs the number of calculations that are necessary for solving the solution matrix. As seen in Eq.4.32, the size of the matrix corresponds to the number of cells. Thus, increasing the grid resolution implemented for CFD simulation will consequently increase the convergence rate and computational time.

Grid independence is defined as the limit where the solution results exhibit minor or no change for a further resolved mesh. If case-analysis of a specific problem changing various flow parameters is conducted, a grid independence-study should be performed such that the limit for solution convergence or a critical mesh-density limit is quantified.

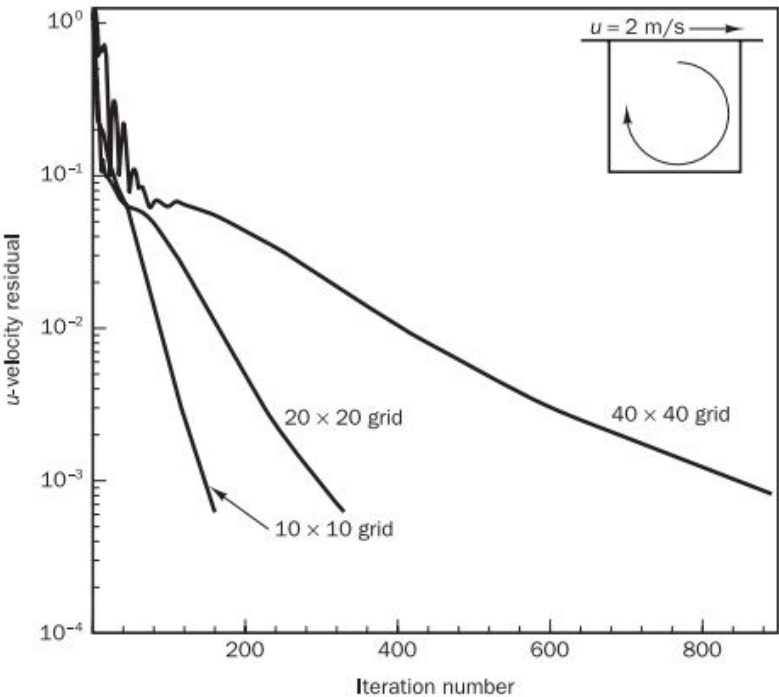


Figure 5.3.: Mesh resolution comparison of convergence rate for the well-known lid driven cavity [15].

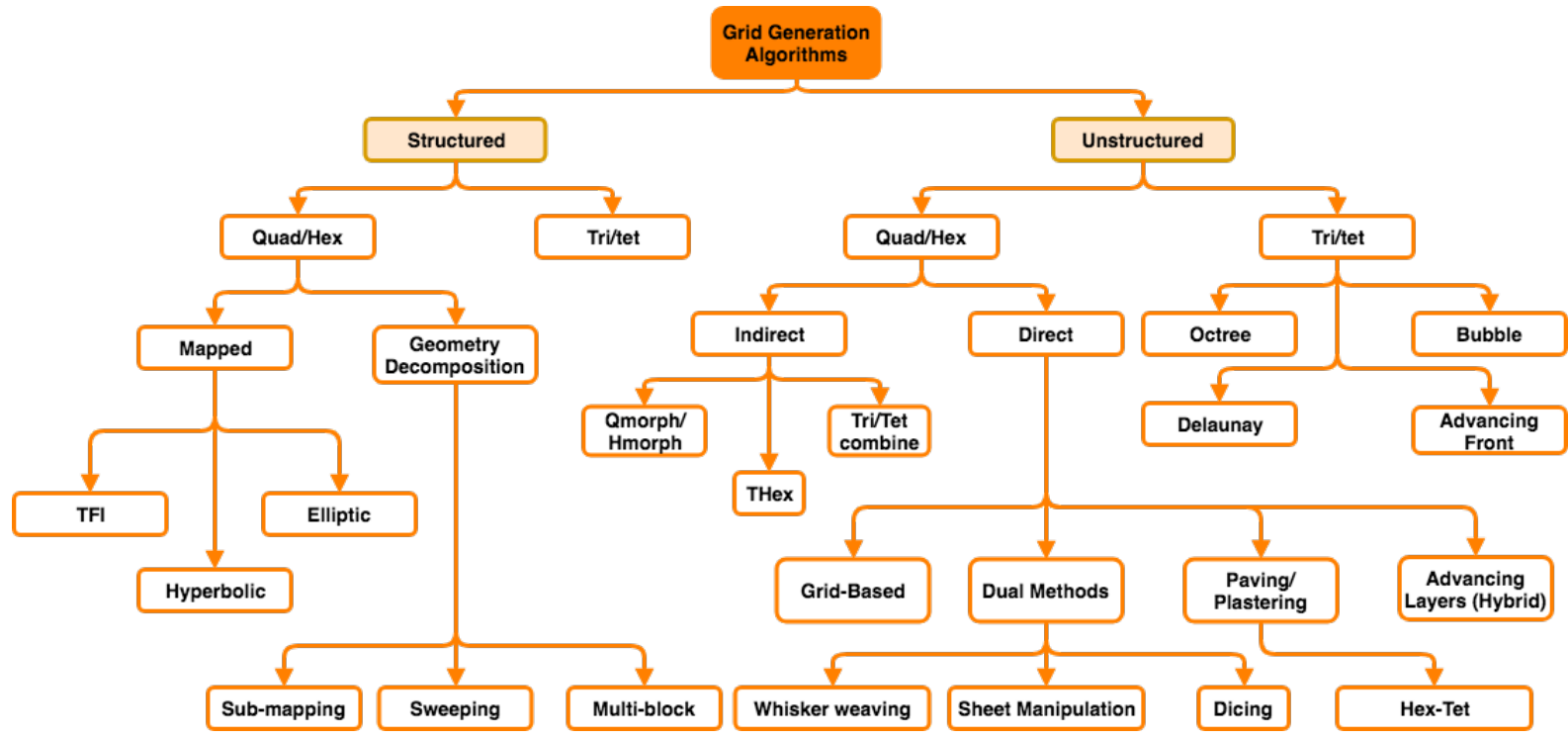


Figure 5.4.: Outline of the various grid generation algorithms [16][17].

### 5.3.1. Data Structure of the Mesh

The data structure is related to the way the information of the generated grid is stored. Using a simple 2D triangular cell seen in Fig.5.5 as an example, the geometric composition consists of nodes, faces, and volumes. Nodes describe the corners of the cell, faces describe connectivity of the nodes, while the corresponding volume is denoted from the nodes and faces. Therefore, the data of the nodes and faces are independent, whereas the volume is dependent on the nodes and face data. Thus, information of nodes and faces must be stored in a data structure.

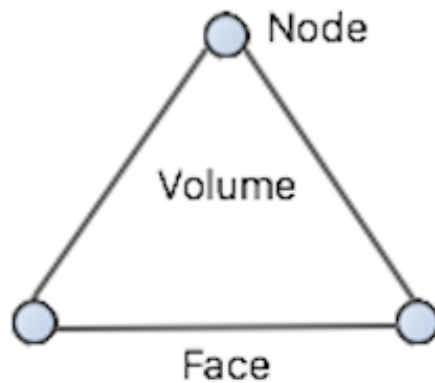


Figure 5.5.: Triangular cell with node, face volume.

The information for each node, face, and cell for the generated grid will have a unique ID numbering. It was previously mentioned in Sec. 5.1 that the normal vector for cell faces needs to be identified, such that this can be stored. This is necessary for calculating convective and diffusive actions in the solver algorithm and specify boundary properties at the faces.

The mesh data can be concluded for the three main parameters for data structuring:

1. *Node data*: Information regarding node position and ID numbering for the entire mesh
2. *Face data*: Information regarding face and face-direction of the normal vector based on node information
3. *Cell data*: Information of cell ID and cell position based on face information

From the data structure created during grid generation, boundary conditions may be applied



directly in a meshing software if desired. This is an option such that boundary condition-input of the computational domain is not needed to be implemented for the flow solver.

### 5.3.2. Data Structure of ANSYS Fluent

For understanding the data structuring for an important mesh in Fluent, a discussion with a simplified example will be presented. The mesh is stored in a mesh file (.msh) format, readable for a wide range of numerical computational software.

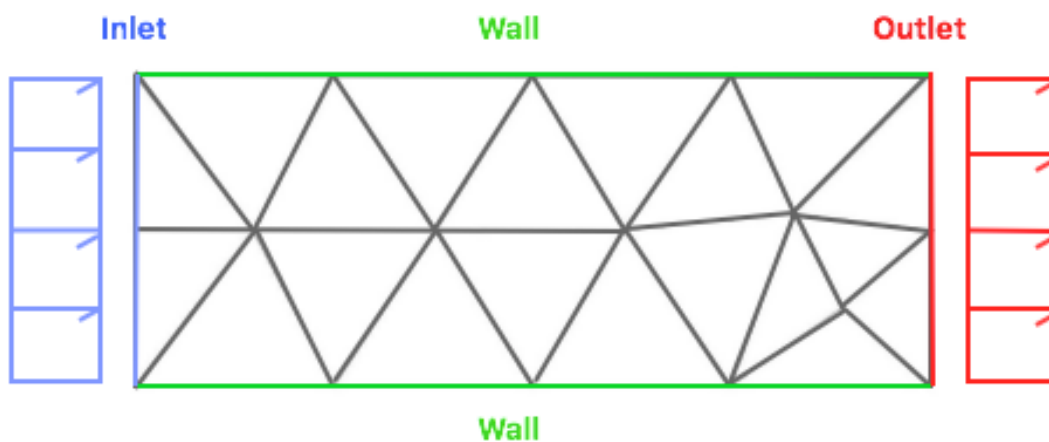


Figure 5.6.: Grid generation of a 2D rectangular domain with tri-cells with highlighted faces.

Fig. 5.6 is a generated grid, where the boundaries are highlighted at the faces. This mesh contains data-blocks containing information about the nodes, faces, cells and user-defined information. The latter is where the data regarding boundary conditions can be stored.

#### Node Information

The node information contains every node in the mesh, where every node are given a unique ID. All information is stored and specified with Cartesian coordinates of the spatial position of the node since the solver also are based on the same coordinate system. Fig.5.7 shows this where the first two code-lines are the ID of all nodes and the indented a summary of the nodes with its spatial position in Cartesian coordinates, respectively. The information is stored using a hexadecimal system.

```
(10 (0 1 11 1 2))
(10 (1 1 11 1 2))
0.0000000000e+000 0.0000000000e+000
4.0000000000e+000 0.0000000000e+000
1.0000000000e+000 0.0000000000e+000
2.0000000000e+000 0.0000000000e+000
4.0000000000e+000 2.0000000000e+000
4.0000000000e+000 1.0000000000e+000
0.0000000000e+000 2.0000000000e+000
3.0000000000e+000 2.0000000000e+000
2.0000000000e+000 2.0000000000e+000
1.0000000000e+000 2.0000000000e+000
0.0000000000e+000 1.0000000000e+000
5.9218874523e-001 1.0015295404e+000
3.5617774565e+000 5.0547988536e+000
3.3172767406e+000 1.1104332902e+000
2.4662988819e+000 1.0087440743e+000
1.5120397407e+000 1.0019497697e+000
))
```

Figure 5.7.: Node information extracted from the .msh-file.

#### Face Information

The face information contains every face, again, where all faces are given a unique face ID. This is shown in Fig. 5.8. The code starts by stating the faces and summarizing the faces. The summarized faces are specified in the node information. Information regarding boundary conditions is also contained in the code, calling on the user-defined information block.

#### Cell Information

The cell information is based on the face information. Since face information is fixed, the cells corresponding to the face will also be fixed such that no detailed cell information is needed. Thus, a few numbers of lines are needed to state the number of cells in the domain, seen in Fig.5.9.

#### User-Defined Information

As stated previously, contains the boundary condition data specified by the user. This is shown in Fig. 5.10.

```
(0 "Faces:")
(13(0 1 24 0))
(13(3 1 2 5 0))
(13(3 1 2 5 0))(
2 2 7 6 0
2 7 6 5 0
))
(13(4 3 4 a 0)(
2 8 c 3 0
2 c 1 1 0
))
(13(5 5 c 3 0)(
2 6 9 4 0
2 9 a 9 0
2 a b d 0
2 b 8 f 0
2 1 3 2 0
2 3 4 b 0
2 4 5 12 0
2 5 2 7 0
))
(13 7 d 24 2 0)(
2 1 d 1 2
```

(a) Face information part (i).

```
2 d c 1 3
2 3 d 2 a
2 d 8 3 f
2 9 f 4 8
2 f 6 4 5
2 f 7 5 11
2 e 2 6 7
2 e 5 7 14
2 9 10 8 9
2 10 f 8 13
2 a 10 9 c
2 3 11 a b
2 11 d a 10
2 4 11 b e
2 a 11 c d
2 11 10 c e
2 b 11 d 10
2 4 10 e 12
2 d b f 10
2 f e 11 14
2 5 10 12 13
2 5 f 13 14
))
```

(b) Face information part (ii).

Figure 5.8.: Face information extracted from .msh-file.

```
(0 "cells:")
(12 (0 1 14 0))
(12 (2 1 14 1 1))
```

Figure 5.9.: Cell information extracted from the .msh-file.

```
(0 "zones:")
(45 (2 fluid fluid)())
(45 (3 pressure-outlet outlet)())
(45 (4 velocity-inlet inlet)())
(45 (5 walls walls)())
(45 (7 interior default-interior)())
```

Figure 5.10.: User-defined information extracted from the .msh-file.

## Part III.

# Simulations & Case Studies

# Single-phase Flow Modelling

---

In the following, an assessment of CFD model validation will be presented, followed by a case-study performed for analyzing the effect of eccentricity in annular flow.

## 6.1. Model Validation: Single-Phase

A series of simulations were performed to validate the CFD model with experimental data of the most relevant rheology. By the courtesy of Zhigarev et al., experimental and simulation data were obtained for comparison of the cases [61].

### Rheological Properties

For the experiments that were carried out by Zhigarev et al., the three drilling fluids were prepared and consisted of a composition of components provided by M-I Swaco, Schlumberger Company. The rheological properties were determined with a rotational viscometer with fluid shear rates varying from 50 to 1022  $s^{-1}$ . The mud density was 1100  $kg/m^3$ .

Table 6.1.: Rheological parameters of drilling mud 1, 2, 3 (Zhigarev 2011).

Drilling Mud	Flow behaviour index, n	Consistency Index, k
1	0.4871	0.2240
2	0.4317	0.5289
3	0.4300	0.8900

The rheological properties are seen in Fig. A.1, as shear rate vs. shear stress curves. As seen from Table. 6.1, the drilling fluids exhibit the same characteristics as that of Power-law fluids, due to the absence of yield stress.

### Concentric Annulus

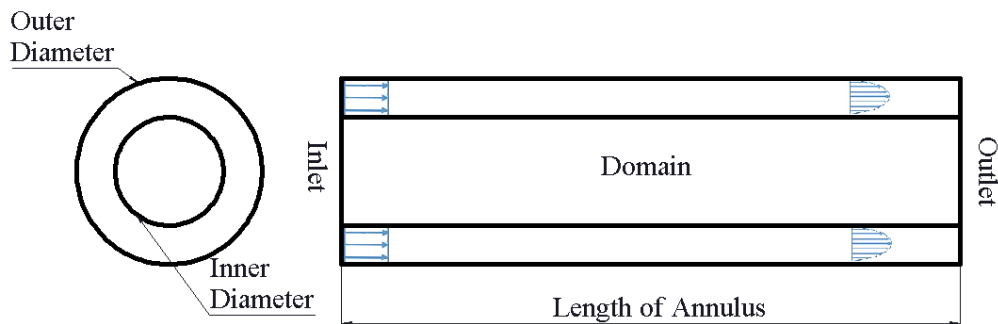


Figure 6.1.: Generated mesh for a concentric case.

The computational domain generated for the concentric annulus was generated in *ANSYS Meshing* where the geometry was  $0.021\text{ m}$  for the outer diameter and  $0.0125\text{ m}$  for the inner diameter. Settings for the grid generations is described in Appendix. A.2.1.

With rheology data and flow variables available, seven simulations for each mud were performed varying the mass flow rate. The CFD results are compared with the calculations performed with Zhigarev et al. and experimental data. A comparison of calculated pressure drop versus mass flow rate can be seen in Fig. 6.3.

To further compare and analyze the deviation of computed pressure drop versus the pressure drop found from the experiments of Zhigarev et al., an error-estimation plot was created, with a 5% error line. Both the calculated results of Zhigarev and the simulated pressure drop from CFD yields reasonable results, showing an accuracy of  $\pm 5\%$  for the specific case. It can be shown that the deviation increases with decreasing flow rates. The same trends are observed from the results of Zhigarev et al.

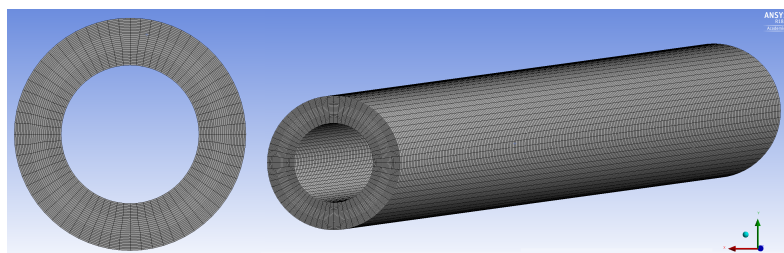


Figure 6.2.: The flow domain of annular flow problems.

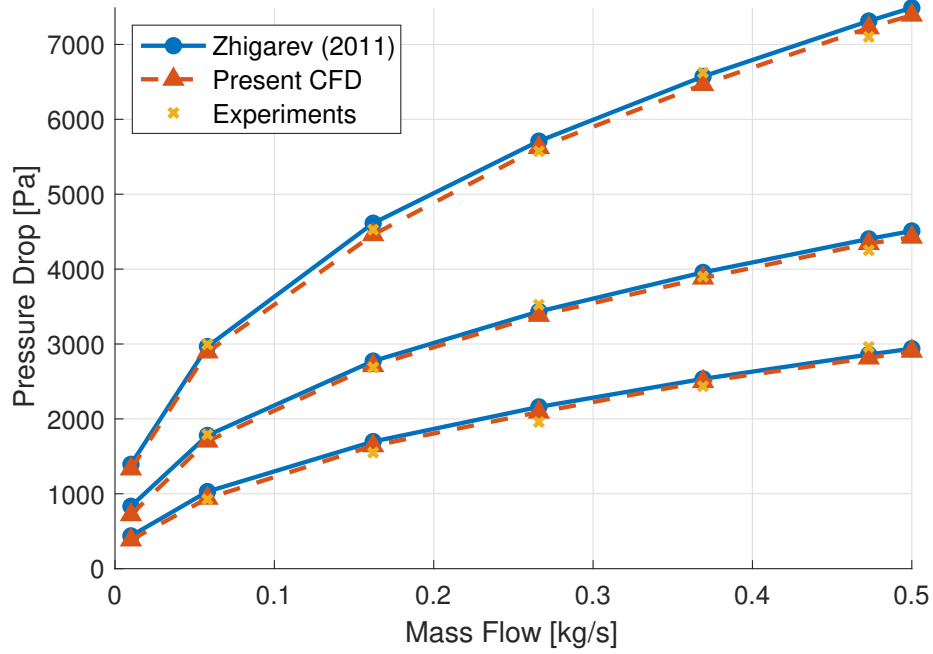


Figure 6.3.: Pressure drop for simulated and experimental data for the different mud varying with mass flow compared with Zhigarev (2011).

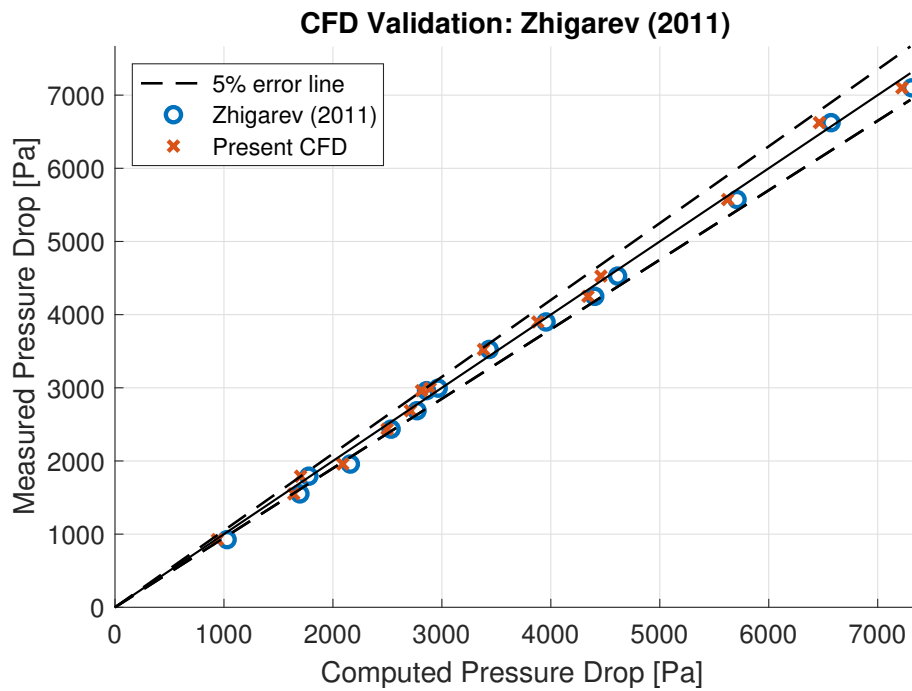


Figure 6.4.: Computed vs. measure pressure drop for results from the present CFD simulations, as well as that of Zhigarev (2011).

**Eccentric Annulus**

A model validation for the effects of eccentricity was also desirable to obtain. Five different simulations are performed with eccentricity varying from 0 to 1 with a 0.25 increment. This was done with the drilling fluid 3 with a constant mass flow rate of 0.473 kg/s. The results are plotted against the results of Zhigarev et al. in Fig. 6.5. The same procedure for comparison was performed for the eccentricity cases, as seen in Fig. 6.6. It is seen that the simulations for eccentric cases agree well with the experimental data.

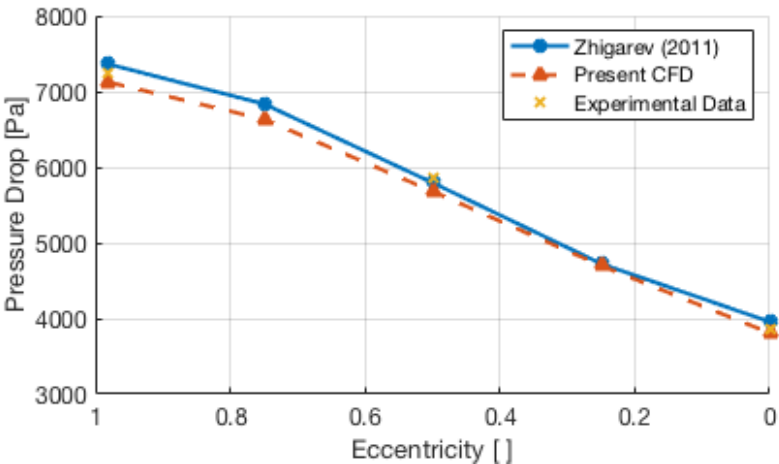


Figure 6.5.: The effects of eccentricity of the pressure drop shows agreement with the experimental data for both Zhigarev (2011) and the performed simulations.

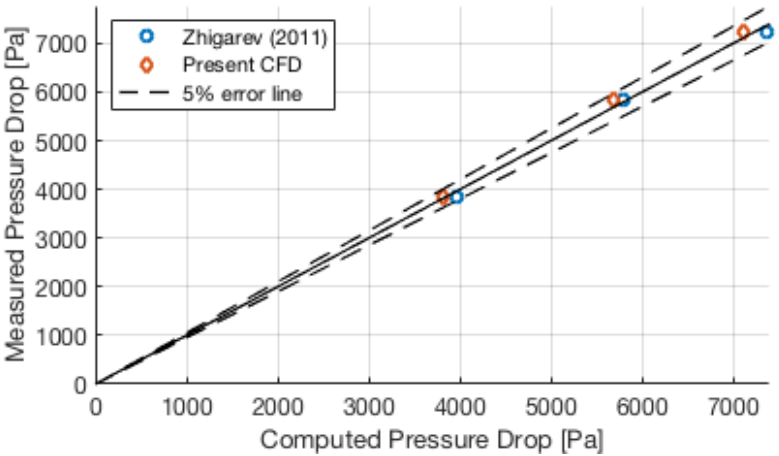


Figure 6.6.: The results from the eccentricity study shows that the model shows a low degree of deviation from the experiments.



## 6.2. Model Validation: Mesh Independence

To analyze the validity of the mesh and quantifying the number of cells needed for the simulations, a mesh convergence study was performed. Seven simulations were performed, starting from  $10^6$  number of cells with an increment of  $5 \cdot 10^5$ , and ended up on  $5 \cdot 10^6$  cells.

The basis for the case was for the CFD model validation cases, discussed in Sec. 6.1, for the zero eccentricity case with a flow rate of 0.473 kg/s and same rheology as discussed previously.

As seen in Fig. 6.7, it was found that the measured parameter of pressure drop showed a converged solution at  $3 \cdot 10^6$  cells. As a result, the eccentricity cases, which will be discussed in the following section, would be based on a cell count from this study. Moreover, as seen from the trend of pressure drop, fewer cells may yield inaccurate results, since the important flow parameter of pressure has not converged for cells less than  $3 \cdot 10^6$ . In addition, seeing that the pressure did not vary, implies that total mesh count based on this study can be above  $3 \cdot 10^6$  without affecting the results in any extent.

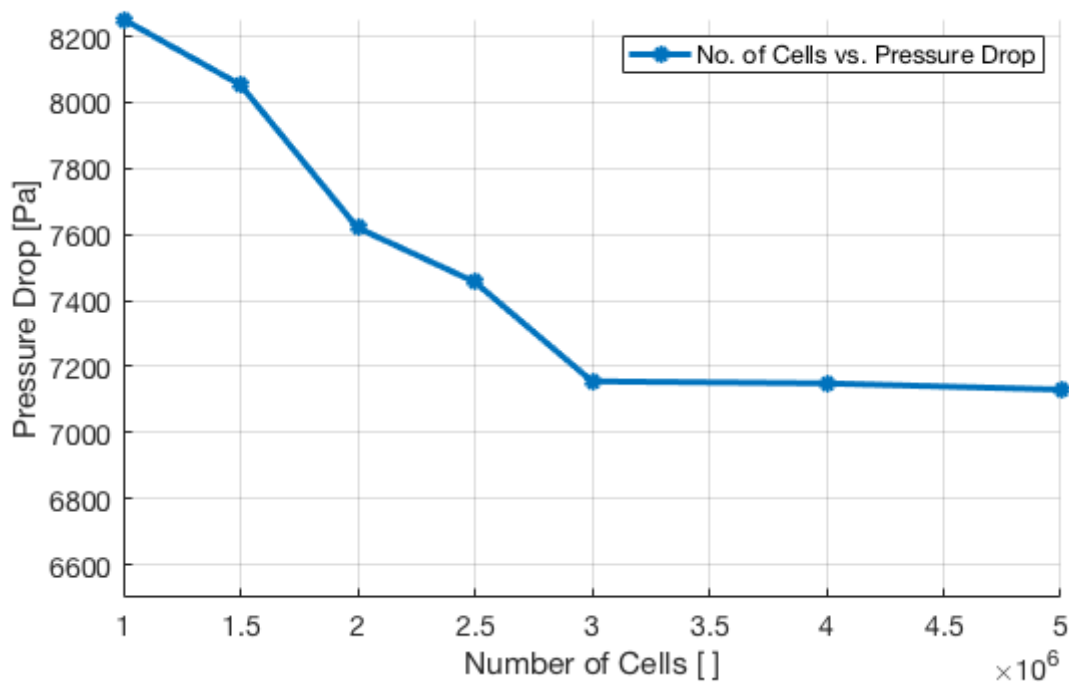


Figure 6.7.: Mesh independence study performed, where pressure drop vs. number of cells is computed.

### 6.3. Single-phase: Eccentricity Analysis

In order to perform analysis of flow displacement for component analysis, it was necessary to conduct a detailed study of the annulus of interest. The simulations were performed with a constant flow rate of 8 BPM, similar to the operational pumping conditions during primary cementing. The well geometry of interest is 9-5/8" casing in a 12-1/4" open-hole, which is the longest section for common well architectures in oil production. A customary rheology for the cement and pumping operations for 9-5/8" primary cementing are developed and specified by Schlumberger.

The aim of this study is to specify flow characteristics during operational conditions. Main parameters of interest are to analyze the effects of eccentricity and its effect on flow parameters such as high- & low-side velocities, velocity profile and pressure drop. The secondary goal is to compare the non-Newtonian Herschel-Bulkley rheology with Newtonian rheology.

#### **Approach**

As a step for evaluating the effect of eccentricity, 3D simulations are performed with a laminar flow model with a non-Newtonian Herschel-Bulkley model and with the Newtonian model for single-phase simulations. Several benchmark cases for both rheological models were performed to ensure that important flow characteristics were captured before a parametric study could be performed. This involved adjusting the cell-count of the mesh, varying the domain length in axial-direction, adjusting discretization-settings and modifying solver-settings. When a sufficient model had been developed with a corresponding adequate mesh, the parametric study was performed.

#### **Assumptions and clarification**

It is necessary to highlight the assumptions being made and uncertainties which come with the modelling assumptions before simulation set-up is considered.

#### *Assumptions*

- Steady-state flow
- Laminar flow
- Isothermal process
- Constant flow rate
- Symmetry along mid-plane of the annulus
- No-slip conditions at walls
- No hydraulic roughness at walls

### *Uncertainties*

#### 1. Casing simplification

The increased diameter at each end of the casing, there exists the male and female connections for connecting casings together to form a string of casings. For the geometry, this is smoothed out such that the casing is modelled as with a uniform smooth pipe.

#### 2. Wellbore simplification

In a realistic wellbore, the walls of the open-hole are never completely straight and have different wall roughness due to different formations, drillbit types, ROP and many other factors. This is modelled as a uniform smooth pipe.

#### 3. Rheology

Rheological data are taken from rotational viscometer, performed by Schlumberger. Any experimental error will lead to deviation from the cement pumped in the well. Moreover, the viscometer tests were taken for six ranges of shear rate and implemented in the derived script for obtaining the rheological parameters and implemented into a rheology model in the CFD model. Such a model will not be completely accurate, and any shear rates beyond the highest shear rate during viscometer tests will result in inaccurate fluid modelling.

#### 4. Downhole Pressure

The downhole pressures are not evaluated for the simulations. Taking into account the formation pressure on the column of fluid makes the case simulation being only valid for different condition and wellbore sections. Neglecting this enables a general case-study possible since the TVD is not taken account for.

### Model Validation

The basis of CFD model is the same as has been validated against the Zhigarev et al. which performed an analysis of eccentricity for drilling mud with both CFD and experiments [32]. The result and model deviated is stated previously in Section. 6.1. It must be noted that since the rheology used for the present case is not the same as the model validation case, the degree of accuracy is only present to a certain extent. The reasoning for this was that experimental data for the present case is not available.

### Geometry

The geometry for the simulations is generated in CAD-environment, *SolidWorks*. The geometry of interest is the outer diameter, dictated by the drilled open-hole of 12-1/4", and the inner diameter of being the outer rim of 9-5/8" casing joints.

Due to symmetry, the computational domain was split at the midplane in the axial direction, resulting in a half-section of an annulus as the geometry.

Five different geometries were created for the corresponding five eccentricities. The dimensions of the outer and inner diameter were fixed, varying only the distance along the vertical axis at which the center for the diameters coincide. This can be visualized in Fig. 6.9. The different cases can be shown in Table. 6.2.

Table 6.2.: Parameters of geometry for the eccentricity cases.

Case	Eccentricity	Low-side gap
1	0	33.34 mm
2	0.25	25.00 mm
3	0.5	16.67 mm
4	0.75	8.33 mm
5	1	0 mm

## Mesh

The mesh for the eccentricity cases were generated on the basis of high-quality cells for capturing the flow characteristics of the flow problems. Having a computational grid being able to satisfy desired numerical accuracy, converge and computational time were also important factors.

Generation of the mesh resulted in a computational domain containing 3.000.000 cells, structured in the flow direction for most cases. For 0% stand-off case, mesh refinement had to be performed due to the extremely small gap in the low-side of the annulus. Using the same grid generation technique, as have been done for all cases, yielded a mesh of 5.697.699 cells. The sweeping method has been used to create the mesh, where a specific number of cells have been chosen for the outer diameter, inner diameter, and symmetry phases at the high- and low-side of the annulus. Details regarding the grid generation can be seen in Appendix A.2.1.

The mesh generation was performed in *ANSYS Meshing*, which is an integrated grid generation tool in the ANSYS environment. All cells satisfied the mesh metrics criteria, stated in Sec. 5.2. Further detail regarding mesh settings and mesh statistics can be found in Appendix A.2.1. In Fig. 6.8, a visual presentation of the mesh can be seen.

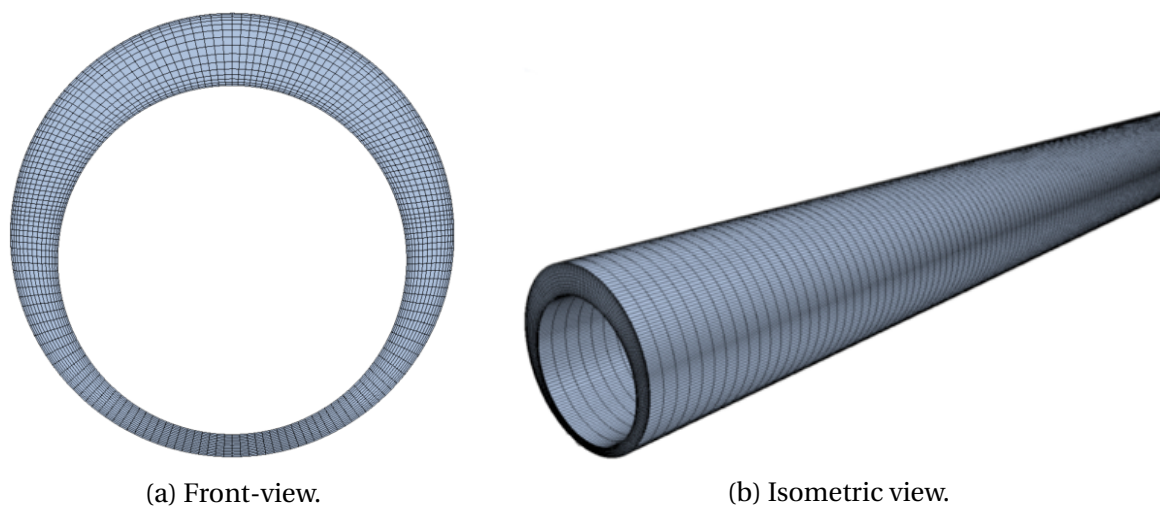


Figure 6.8.: An example of generated mesh, here visualized for the 0.5 eccentricity case.

## Rheology

Rheological parameters were obtained with a basis of rotational viscometer test performed by Schlumberger for their customized cement. The six-range viscometer data were imported into a *MatLab*-script developed for obtaining non-Newtonian rheology data with respect to yield point, flow behaviour, and consistency index. The rheological parameters implemented in the CFD model is shown in Tab. 6.3. Further details of the rheology analysis of the cement can be seen in Fig. A.2.

Table 6.3.: Rheological parameters of 9-5/8" tail cement.

Rheology model	Yield Point, $\tau_0$ [Pa]	Flow behaviour index, $k$ [ $\text{Pa}\cdot\text{s}^n$ ]	Consistency index, $n$ [ ]
Newtonian	0	0.1468	1
Herschel-Bulkley	2.2634	0.7688	0.5582

## Boundary Conditions

The constant operational flow rate of the pump is 8 BPM, which yields a velocity inlet of 0.7286 m/s for the specific case. The boundary conditions implemented are shown in Tab. 6.4. Since the flow conditions were the same for all cases, these settings remained fixed. A velocity inlet/pressure outlet condition was chosen for obtaining the operational condition of constant flow rate in the annulus, and also due to CFD practices explained in Sec.

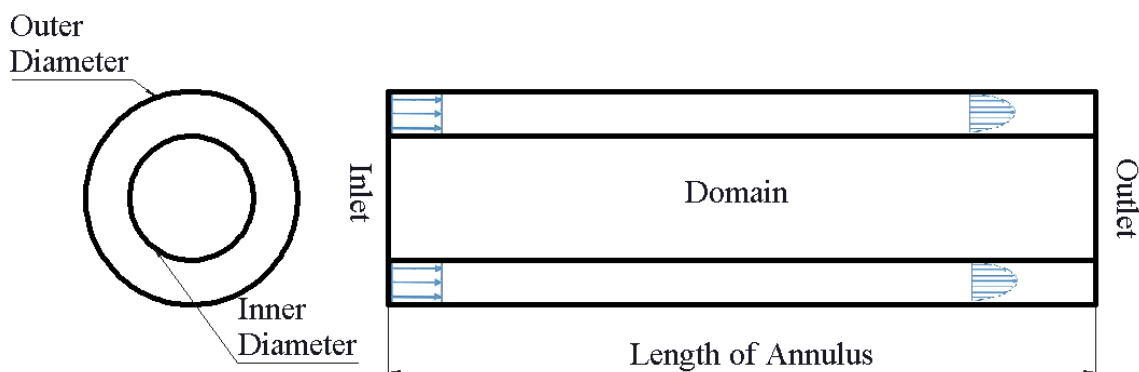


Figure 6.9.: An illustration of the modelling domain for CFD analysis.

## 4.4.1.

For the computational domain for the faces and cell-zones, boundary conditions are assigned as stated during the meshing-phase in *ANSYS Meshing*, which is an integrated meshing software in the ANSYS environment. Assigning this at the integrated mesher in *ANSYS*, results in less effort stating boundary conditions in *Fluent*, where only the scalar quantities are applied. This also makes it possible performing parametric studies, since the outer boundaries for this internal flow problem already are defined.

Table 6.4.: Boundary conditions used for eccentricity cases.

Boundary	Boundary Type	Value
Inlet	Velocity inlet	0.72862 m/s
Outlet	Pressure outlet	0 Pa
Wall	No-slip condition	-
Symmetry	Symmetry plane	-

## 6.3.1. Solver Settings

Details regarding the solver settings are shown in Table. 6.5, below.

Table 6.5.: Solver settings for eccentricity cases.

Properties	Settings
Software	ANSYS Fluent 19.0
Calculation	Steady State
Solver Type	Pressure-Velocity Coupling
Solver Algorithm	SIMPLE
Discretized Equations	Differencing scheme
Gradient	Least squares cell-based
Pressure	Second-order Upwind
Momentum	Second-order Upwind

From the first benchmark cases, high residuals were observed when non-Newtonian rheology model was used. Therefore, refining and generating a high-quality mesh were performed in conjunction with lowering the URF's for the discretized pressure and momentum equations. Details of URF setting used is shown in Table 6.6.

The stopping criteria were set for 1000 iterations. Due to the fact that the residuals varied for

### 6.3. SINGLE-PHASE: ECCENTRICITY ANALYSIS

---

the Newtonian and Non-Newtonian cases, the simulations were run with the same stopping criteria. After the few benchmark simulations where run individually, a *parametric study algorithm* where applied such that all simulations were performed in a sequential manner, at the same time. This is a function available in the *ANSYS* environment for CAE analysis. This resulted in a time-efficient way of running the all the respective cases.

Table 6.6.: Under-relaxation factors implemented for eccentricity cases.

<b>Under-Relaxation Factors</b>	<b>Settings</b>
Pressure	0.2
Density	1.0
Body forces	1.0
Momentum	0.6



6.3.2. Schematic of present CFD set-up



Figure 6.10.: Schematic of CFD set-up in *Fluent* for performing single-phase simulations.

### 6.3.3. Results

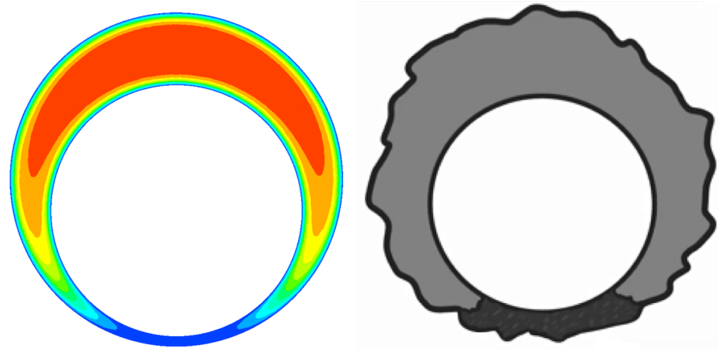


Figure 6.11.: Illustration of the effect of eccentricity yielding improper cement displacement.

For all simulation performed, double-precision using higher-order discretization, in addition to a large computational domain was applied, resulting in a computational time of approximately 8 hours until the stopping criteria were reached. The Newtonian cases took around 2 hours less than the non-Newtonian cases. This was performed with 6 cores on a 3.2 GHz quad-core processor with 16GB RAM.

For multiple visual observations seen from Fig. 6.12-6.21, 3D and 2D velocity plots show the velocities and velocity profiles for eccentricities ranging from 0 to 1. CFD analysis was performed for five cases with a 0.25 increment, for each rheology model. Data for high- and low-side parameters were acquired from the midsection between wellbore and casing. The data for fully developed flow were extracted at 8 m from the inlet for eccentricities 0, 0.25, 0.50 and at 10m for eccentricities of 0.75 and 1.0.

For the two latter cases, an increase of the domain in the axial direction has to be performed, due to the flow not reaching steady-state with an outlet placement 10 m from the inlet. Increasing the domain length showed that the flow reached steady-state for both Newtonian and non-Newtonian compared to a 10 m domain.

## Flow Velocities in Eccentric Annuli

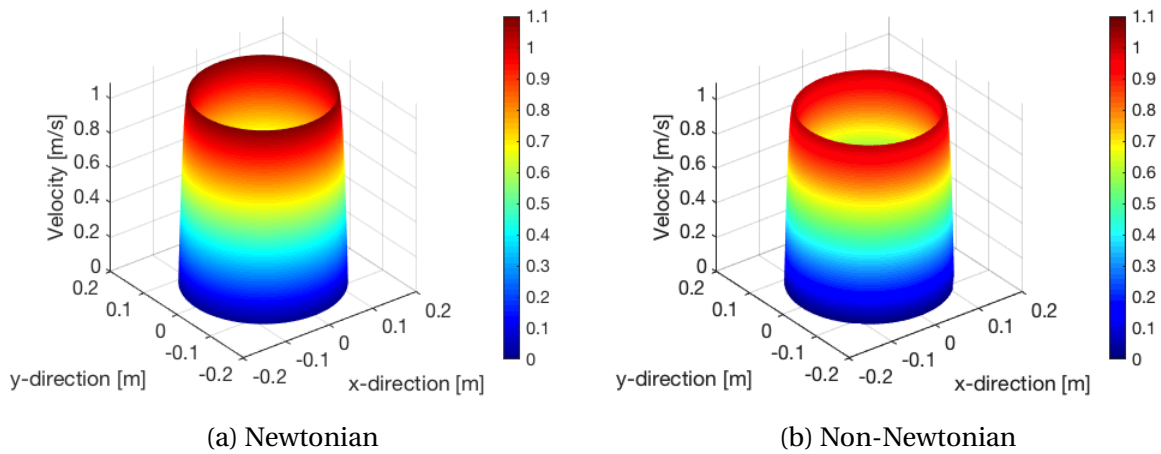


Figure 6.12.: Comparison of Newtonian and Non-Newtonian (*Herschel-Bulkley Model* with eccentricity = 0, visualized with a 3D velocity plot.

For eccentricity = 0, it can be observed that the velocity distributions are equal, due to concentricity. However, it can be observed that the velocity profiles for the two rheological models differ. This can be viewed in Appendix, A.4. The difference of magnitude of maximum velocity is with 7%, where the Newtonian case has a peak velocity of 1.092 m/s where for Herschel-Bulkley modelling a peak of 1.010 m/s. It is observed that the velocity profile is the same everywhere in the annulus, due to concentricity.

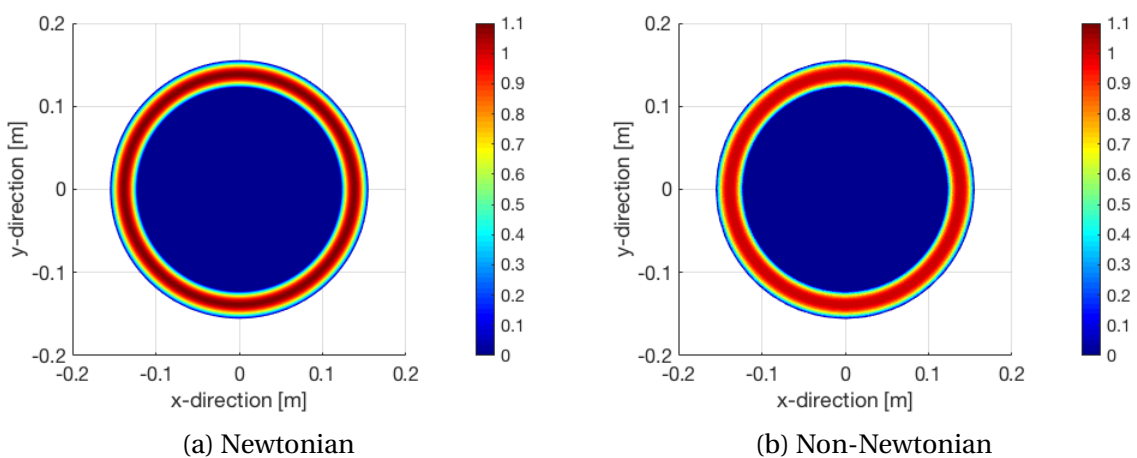


Figure 6.13.: Comparison of Newtonian and Non-Newtonian (*Herschel-Bulkley Model* with eccentricity = 0, visualized with a 2D velocity plot.

### 6.3. SINGLE-PHASE: ECCENTRICITY ANALYSIS

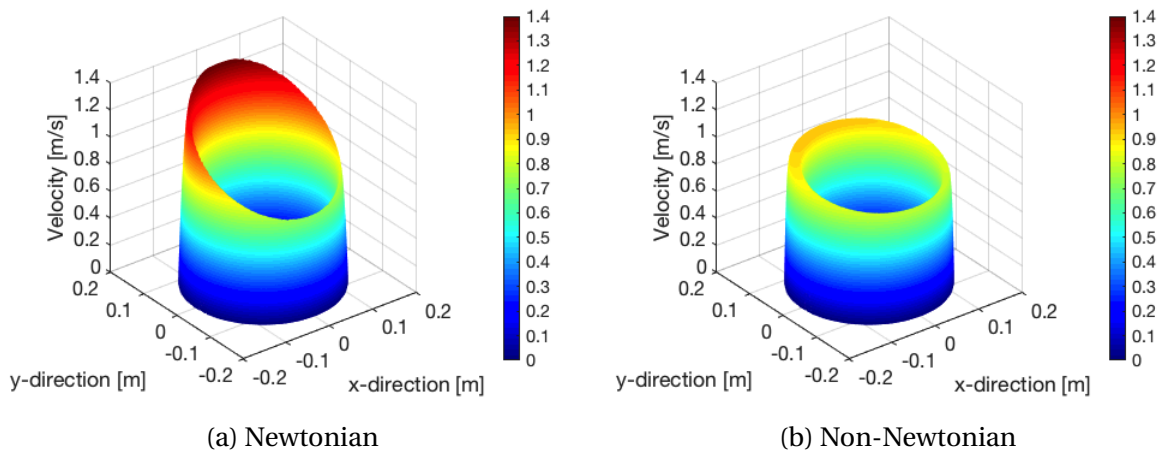


Figure 6.14.: Comparison of Newtonian and Non-Newtonian (*Herschel-Bulkley Model* with eccentricity = 0.25, visualized with a 3D velocity plot.

For eccentricity = 0.25, the effect of eccentricity is visualized in Fig. 6.14a for Newtonian, but not as present for the *Herschel-Bulkley* modelling seen in Fig. 6.14b. The velocity distributions throughout the annulus are seen in Fig. 6.15, which highlights what have been described previously. For Newtonian rheology, the peak high-side velocity is 1.4144 m/s, where for *Herschel-Bulkley* it is 0.9379 m/s. For low-side velocities, these are 0.7236 m/s and 0.7836 m/s for Newtonian and *Herschel-Bulkley*. The peak-velocity difference between low- and high-side of the annulus is 0.6908 m/s for Newtonian and 0.1543 m/s for *Herschel-Bulkley*. The velocity profile in the annulus can be seen in Fig. A.16.

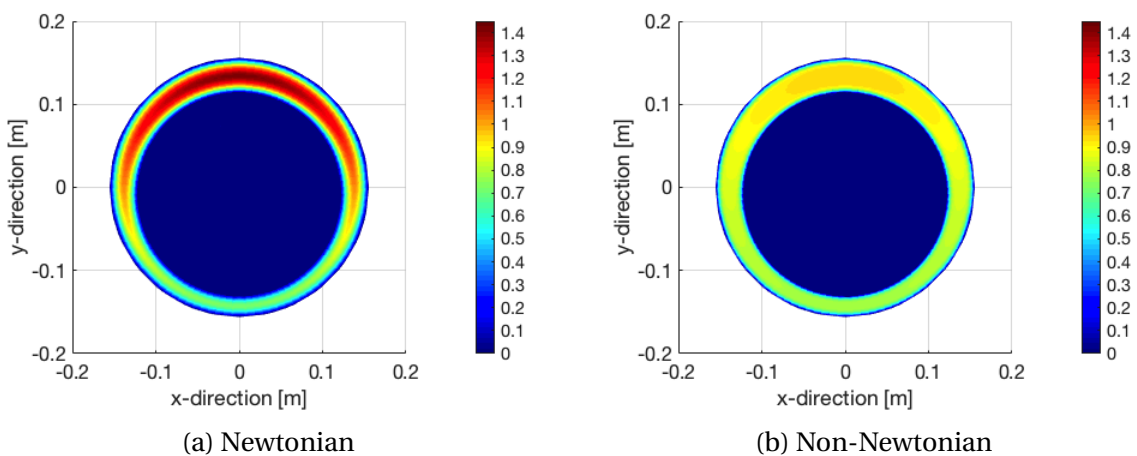


Figure 6.15.: Comparison of Newtonian and Non-Newtonian *Herschel-Bulkley Model* with eccentricity = 0.25, visualized with a 2D velocity plot.

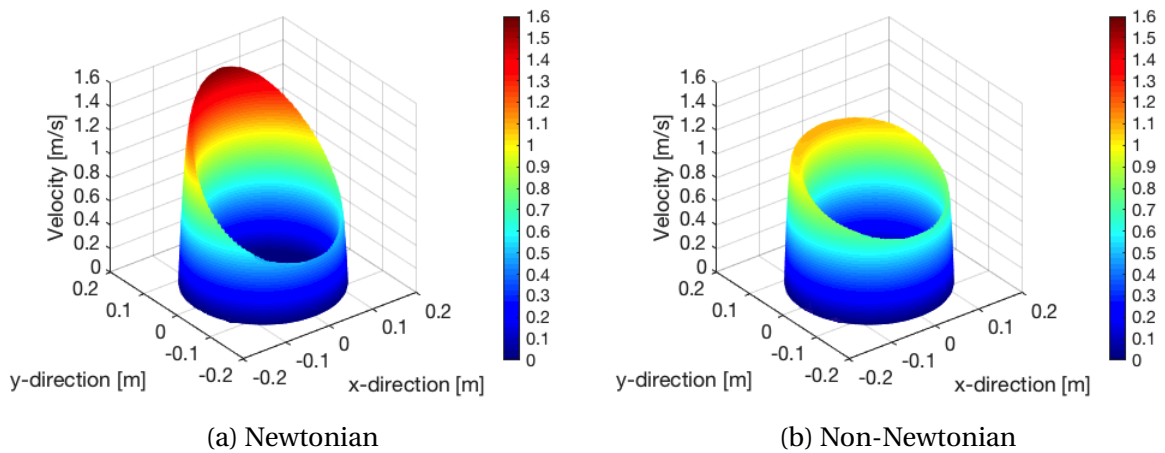


Figure 6.16.: Comparison of Newtonian and Non-Newtonian (*Herschel-Bulkley Model* with eccentricity = 0.50, visualized with a 3D velocity plot.

For eccentricity = 0.5, the gap at the high-side of the annulus is double of the low-side gap. Thus, the eccentricity effects are now clear for both cases, seen for 3D in Fig. 6.14. The peak velocities for Newtonian rheology are 1.5700 and 0.4660 m/s for high- and low-side, respectively. Difference in peak-velocity are 1.1040 m/s. The peak velocities for Herschel-Bulkley are 1.0895 m/s at the high-side and 0.6753 m/s at the low-side, yielding a difference of 0.4142 m/s. Velocity profile for both rheologies is shown in Fig. A.18

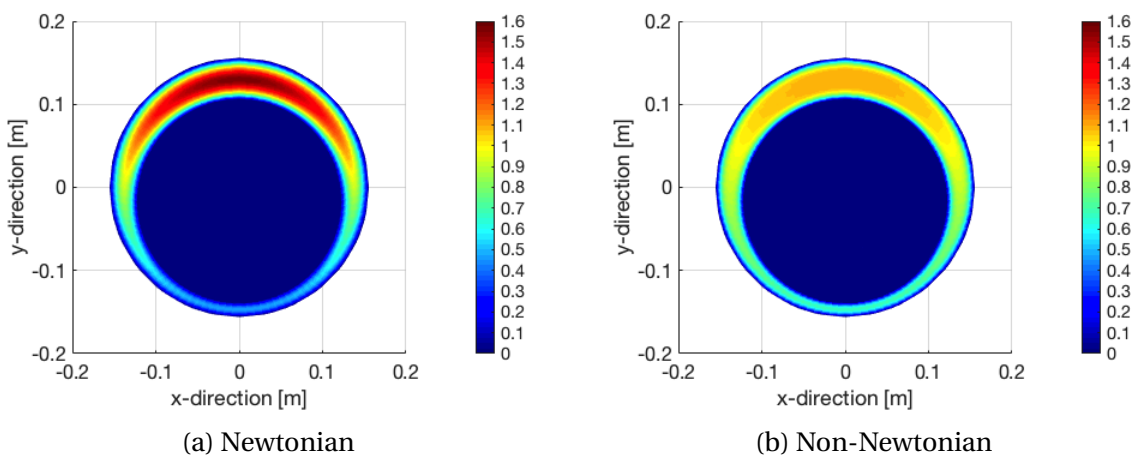


Figure 6.17.: Comparison of Newtonian and Non-Newtonian (*Herschel-Bulkley Model* with eccentricity = 0.50, visualized with a 2D velocity plot.

### 6.3. SINGLE-PHASE: ECCENTRICITY ANALYSIS

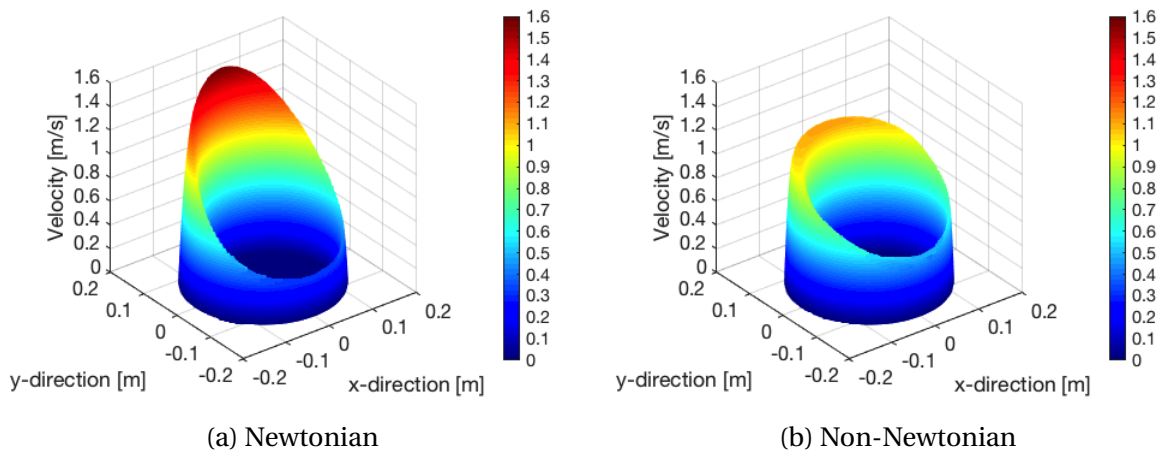


Figure 6.18.: Comparison of Newtonian and Non-Newtonian (*Herschel-Bulkley Model* with eccentricity = 0.75, visualized with a 3D velocity plot).

For eccentricity = 0.75, the geometry exhibits highly eccentric behaviour, which affects the flow characteristics. The velocity shape can be seen in Fig. 6.14 and velocity distribution in Fig. 6.19. For the Newtonian case, the high-side peak velocity is 1.5803 m/s, whereas the low-side is 0.3505 m/s. This gives a difference 1.2298 m/s between the maxima and minima in the annulus. For the Herschel-Bulkley case, high-side peaked at 1.1083 m/s and low-side at 0.5184 m/s giving a difference of 0.5899 m/s. The difference of high-side velocities between Newtonian and Herschel-Bulkley are significant and can be observed in Fig. A.16.

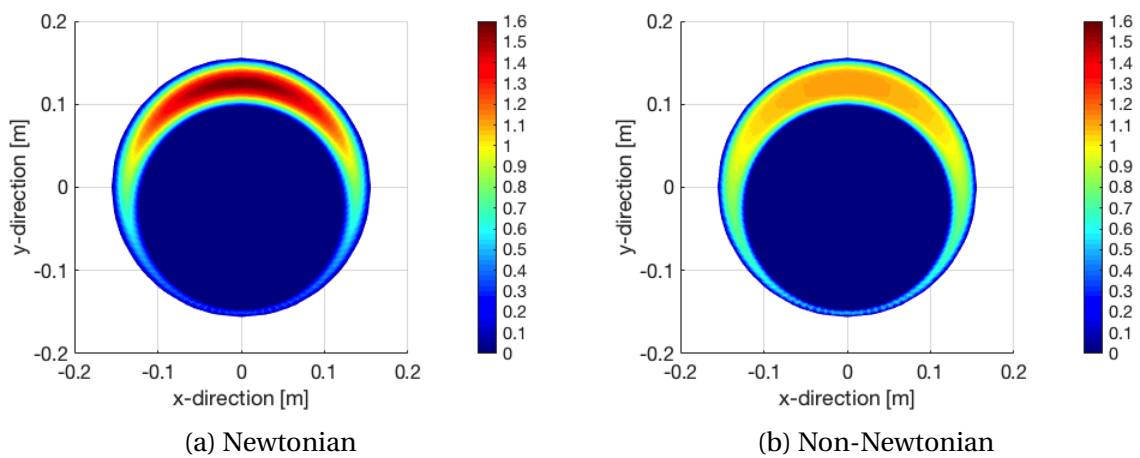


Figure 6.19.: Comparison of Newtonian and Non-Newtonian (*Herschel-Bulkley Model* with eccentricity = 0.75, visualized with a 2D velocity plot).

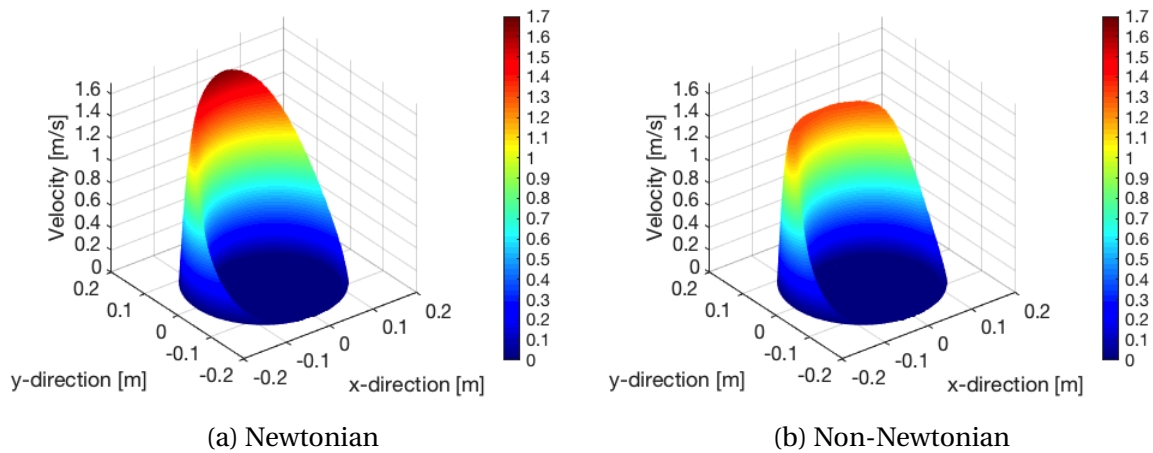


Figure 6.20.: Comparison of Newtonian and Non-Newtonian (*Herschel-Bulkley Model* with eccentricity = 1, visualized with a 3D velocity plot.

For eccentricity = 1, the 3D-shape of the velocity profile is shown in Fig. 6.20. Cross-sectional velocity distribution can be seen in Fig.6.21. These velocity representations show the difference of flow characteristics, where laminar flow exhibit a sharp parabolic velocity form for the Newtonian model (Fig. A.19), whereas the Herschel-Bulkley model exhibits a more flat plug-shaped form. From the 2D-velocity distributions, it can be seen that velocities surrounding the casing, moving in negative y-direction, are greater for the Herschel-Bulkley model. The low-side velocities are not present, thus high-side velocities dominating the flow behaviour in the entire annulus, with peak velocities of 1.5803 m/s and 1.3062 for Newtonian and Herschel-Bulkley. The velocity profiles can be seen in. Fig A.19.

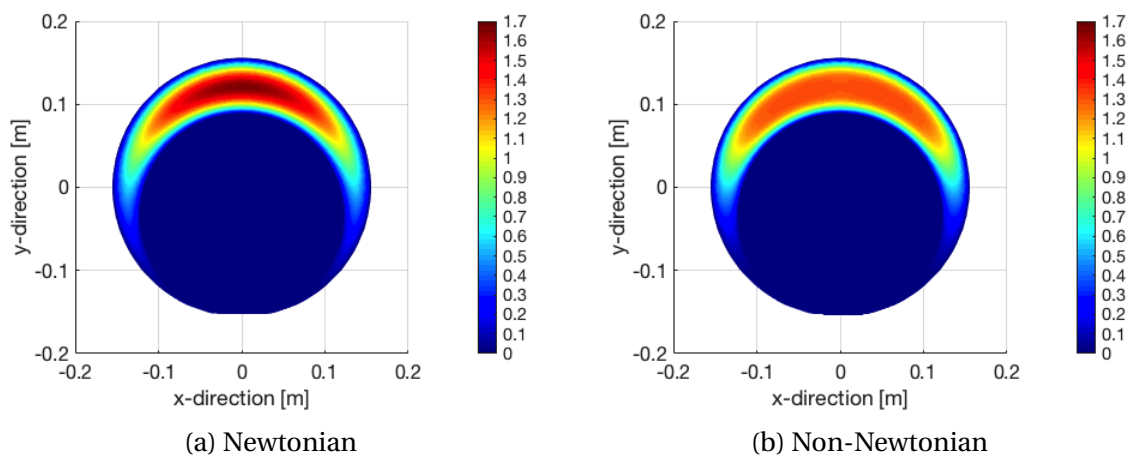


Figure 6.21.: Comparison of Newtonian and Non-Newtonian (*Herschel-Bulkley Model* with eccentricity = 1, visualized with a 2D velocity plot.

Pressure drop in Eccentric Annuli

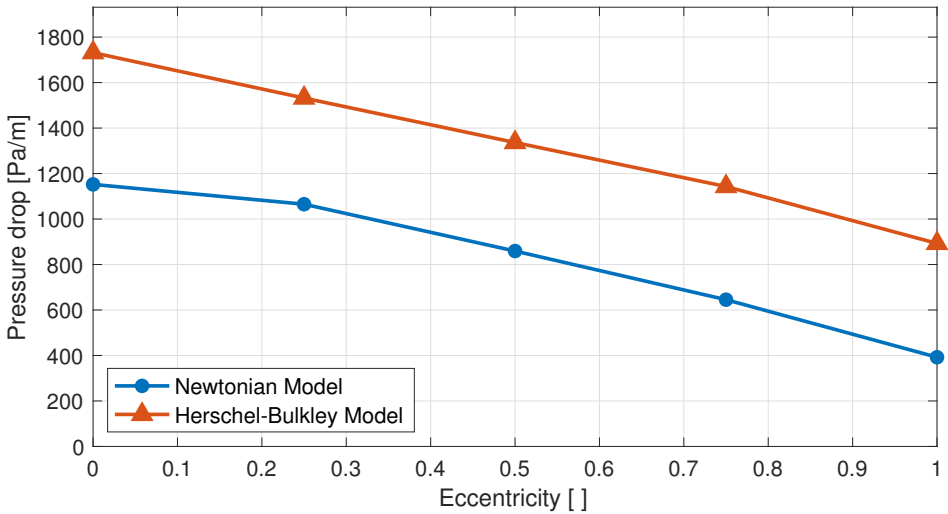


Figure 6.22.: Simulation results for pressure drop [Pa/m] for the various eccentricity cases.

In Fig. 6.22, pressure drop, in [Pa/m], can be observed for all cases. The Newtonian cases show a lower pressure drop, with an almost linear behaviour for eccentricities ranging from 0.25 – 1. The Herschel-Bulkley cases exhibit an even more linear behaviour for increasing eccentricity. Comparing the two rheology models, the Newtonian yields approximately 500 Pa/m lower pressure drop than the Non-Newtonian for all eccentricities.



### 6.3.4. Assessment of Pressures in Annuli with Correlated Models

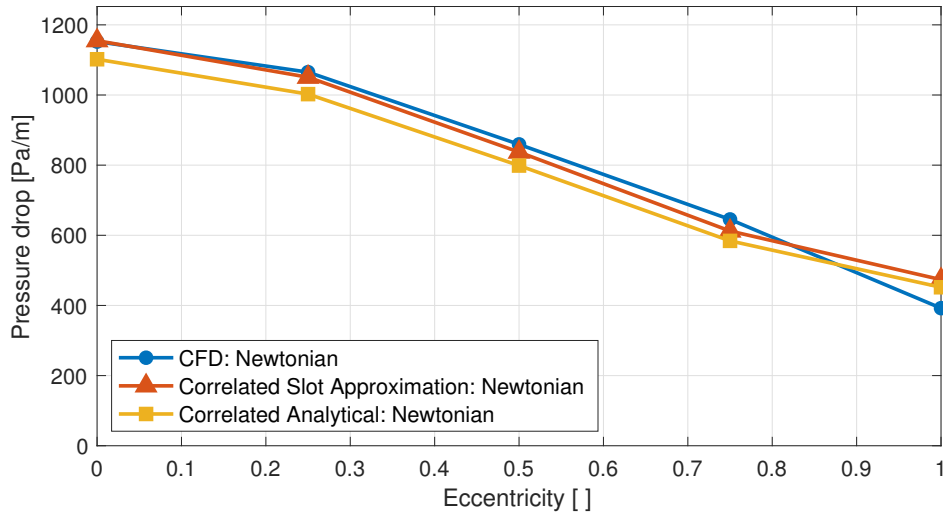


Figure 6.23.: Comparison of pressure drop computed from the present CFD simulations vs. eccentricity for Newtonian rheology model with correlation from the work of Hacıislamoglu & Langlinais (1990) and Madlener et. al.(2009).

As discussed in Sec. 2.2, there exist models which can be used to compare with the CFD simulations. Fig. 6.23 shows a comparison with the slot approximation (Fredrickson & Bird 1985) and the analytical solution for laminar Newtonian flow. Both cases have been calculated for concentric annulus and thereafter been subject to the correlation presented by Hacıislamoglu & Langlinais (1990), discussed in Sec. 2.2, and mathematically described with Eq. 2.5. As observed, the correlated slot-approximation shows an agreement with the CFD results, where the analytical solution also shows a similar trend. It is seen that the correlated models over-predict the pressure drop for fully eccentric annulus. However, the correlations under-predict the pressure drop everywhere else but showing minor deviations.

For the Herschel-Bulkley cases, a comparison has been performed against three different models, seen in Fig. 6.24. The correlated slot approximation (Fredrickson & Bird 1985) describes an analytical solution where the non-Newtonian effects are implemented in the generalized Reynolds number representation (Madlener et al. 2009), in Eq. 2.4. For the two analytical correlations, the Reynolds number for Herschel-Bulkley and generalized Herschel-Bulkley number, previously presented in Eq. 2.1 (Madlener et al. 2009), was used in the

6.3. SINGLE-PHASE: ECCENTRICITY ANALYSIS

analytical solution for pressure drop for laminar flow and correlated with the basis of Hacıislamoglu & Langlinais for estimating with increasing eccentricity.

The results observed in the graph show a much different result than that observed for Newtonian rheology. The slot approximation and analytical Herschel-Bulkley greatly underpredicts the pressure drop compared to the CFD results. On the other hand, the analytical solution in conjunction with the generalized Herschel-Bulkley Reynolds number correlated into Eq. 2.1, shows a better coinciding for the three models used for comparison.

This shows that a more accurate representation of the Reynolds number of the flow can be used as a suitable tool to predict pressure drops in eccentric annular flow, for non-Newtonian Herschel-Bulkley fluids. It is also much more time-efficient, since calculating the Reynolds number and inserting it into the analytic equation can be done in a short time.

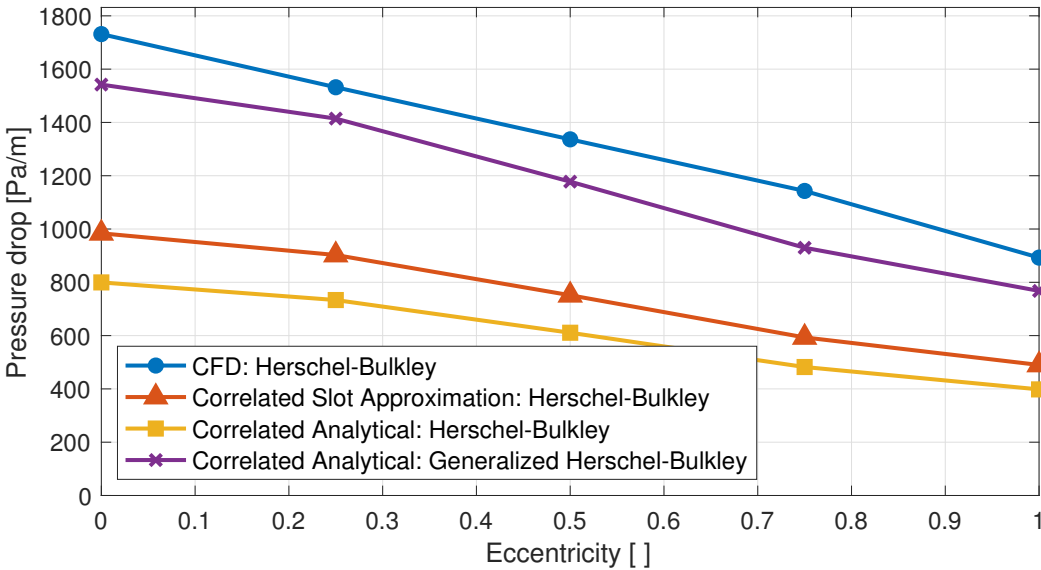


Figure 6.24.: Comparison of pressure drop computed from the present CFD simulations vs. eccentricity for non-Newtonian Herschel-Bulkley rheology model with correlation from the work of Hacıislamoglu & Langlinais (1990) and Madlener et. al.(2009).

### 6.3.5. Effects of Eccentricity

From the simulation results, the following observations are identified for the effects of eccentricity:

- *Low Eccentricity*

Low degree of variations in velocity distributions for Herschel-Bulkley and Newtonian behaviour. Highest pressure drop due to the overall higher velocities present in the annulus.

- *Intermediate Eccentricity*

Due to the eccentricity effects, the velocity distribution may be categorized into two parts, where the high-side shows a plug flow behaviour and low-side shows a lower degree of varying velocity. The effect is significantly higher for Newtonian fluids, where Herschel-Bulkley shows a more distributed velocity contour. Lower pressure drop through the annulus.

- *High Eccentricity*

The low-side flow is absent, indicating a stagnant flow. All the momentum is at the high-side of the annulus. Newtonian flow shows a sharp laminar profile, whereas Herschel-Bulkley flow exhibits a plug flow behaviour. Lowest pressure drop through the annulus.

Comparing the concentric case against the eccentric cases, eccentricity effects cause velocity components to have both radial and axial velocity components, whereas for a concentric case only has axial velocity components. Furthermore, since the Herschel-Bulkley rheology exhibits yield stress behaviour, the flow can form quasi-solid domains in the flow where stresses are below the yield stress of the fluid. These effects are especially prominent in areas next to the walls for high eccentricity.

It is observed that the pressure drop monotonically decreases as the eccentricity decreases for all fluids, seen in Fig. 6.22. Unlike Newtonian fluids or fluids exhibiting yield stress properties, the pressure drop for the Herschel-Bulkley fluids cannot be lower than the value of the yield stress of the fluids. This is one of the factors that indicate the average pressure drop

deviation between the two cases.

Comparing velocity profiles, seen in Fig. A.16, the deviation in profiles are imminent. The Newtonian exhibit sharp peak, whilst the Herschel-Bulkley model shows the cement flow with plug characteristics in high-velocity areas and high gradients in the proximity of the open-hole and casing walls. It can be observed that the velocity gradient for both rheology models is quite similar near the walls. The shape of the velocity profiles coincides with the theory for both rheologies [36], as discussed in Sec. 3.1 and visualized in Fig. 3.2.

### 6.3.6. Assessment of Herschel-Bulkley Modelling of Non-Newtonian Flow

From the study performed, it is clear that numerical simulation of yield shear-thinning fluids based on Herschel-Bulkley model may provide valuable characteristics of the flow. However, there are several problems which need to be addressed to ensure numerical simulation with sufficient accuracy.

Firstly, developing a more robust iterative solution algorithm should be analyzed further to give a better representation of the shearing flow in flow regions with plug- and yield behaviour. This is due to the deformation and elastic action of Herschel-Bulkley fluids, which may express a constraint for the boundaries between regions where the geometry exhibits high eccentricity. The linear interpolation with the gradient method implemented in the CFD model may not capture the deviation of velocity gradients. Ultimately, loss of information may occur due to its crude approximation. For more accurate representations of the physical actions present in the flow, a mechanism-based method should be employed for estimating the correction of the boundary locations where the gradients may be high.

Secondly, as shown for the 3D velocity distributions in Fig.6.14b, 6.16b, 6.18b, and 6.20b, the numerical solution shows a stable plug flow structure. However, this shape may be mechanically unstable for realistic cases, where the steady-state operation will not be as idealized as performed in the present CFD simulations. If any fluctuations are present in the flow, the plug shape may break into sections and dissipate, which cannot be physically captured with a steady-state flow. Thus, for an in-depth analysis of the dynamic flow behaviour and flow

patterns, simulations based on time-dependent studies should be considered.

Lastly, the numerical analysis should be validated against experimental data that are exactly tailored with the exact rheologies and geometries such that the simulation result will have a better validity. For instance, the pressure drops based on flow rates and eccentricity does not reveal differences in terms of a mesoscopic physics that may occur due to the complex nature of the non-Newtonian flow. Experiments with measurement and visualization techniques of high precision are also ideal. The difficulty in this aspect lies with the problem of having fluids showing sufficient transparent properties such that methods like Particle Image Velocimetry and other advanced image techniques such as Laser Doppler Anemometry, may yield more information of perturbations, turbulent effects, and flow structure in transition regions.

# Multiphase Flow Modelling

---

In the following, the study of the multiphase flow of mud-spacer-cement in annulus will be presented. The results of the operational procedure, an assessment of the displacement efficiency, as well as a discussion and comparison with literature will be presented.

## 7.1. Multiphase: Drilling Mud, Spacer & Cement

### Introduction

For this study, an analysis of fluid displacement was performed for the fluid train of drilling mud, spacer, and cement, respectively. The simulations were performed in accordance with actual drilling schedules, developed by *Schlumberger*. The operational target of 900 LPM flow rate was pumped into the well geometry of interest, which is 9-5/8" production casing in a 12-1/4" wellbore. The three rheologies exhibited Herschel-Bulkley behaviour and were modelled accordingly, for immiscible fluid-interaction, which is discussed later.

The aim of this study is to analyze the fluid train and quantify displacement efficiency for the fluid introduced to the annulus, in a specified eccentric configuration of 50% stand-off.

### Approach

For the analysis, 3D simulations are performed for transient flow, laminar flow model, non-Newtonian rheology modelling, with a Euler-Euler approach using Volume-Of-Fluid (VOF) multiphase model.

Several benchmark cases were performed in advance to ensure convergence for mud and spacer, and spacer and cement. Due to the complexity of the CFD model for a large computational domain, high-performance computing (HPC) on NTNU's supercomputer, *Vilje*, was utilized to handle the complex simulations and for reducing the total computational time. With HPC capabilities available, four nodes were used, each containing 16 CPU's, with a processor speed of 2.6 GHz. Using four nodes yields a memory of 32 GB per node.

### Assumptions and clarification

In the following, a list of the assumptions made, as well as uncertainties of the CFD model are considered:

#### *Assumptions*

- Transient simulation
- Laminar flow
- Isothermal process
- Interpenetrating continua (immiscible fluids)
- Constant flow rate
- Symmetry along mid-plane of the annulus
- No-slip conditions at walls
- No hydraulic roughness at walls

#### *Uncertainties regarding multiphase modelling*

##### 1. VOF model

The multiphase model assumes that the fluids are immiscible and avoids any dispersion and intermixing beyond the interface. This may yield inaccurate results compared to real operations.

##### 2. Interfaces between fluids

Due to computational complexity, the donor-acceptor schemes were used. The interface is modelled between the immiscible fluids in a crude way, which will affect the front of the displaced fluid.

### 3. Course mesh

Due to computational time and convergence, the grid size mesh is coarse. This may affect the simulation results.

### 4. Time step

The time step for the simulation may be too large which can affect the simulation results.

## Geometry

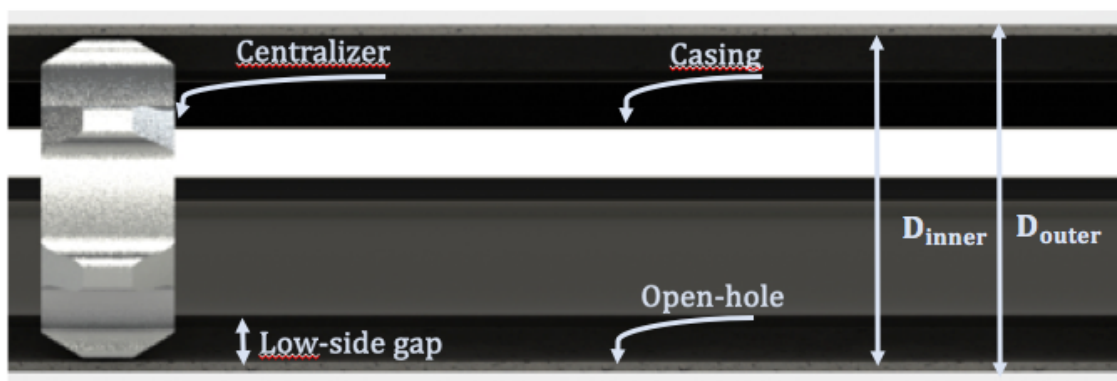


Figure 7.1.: Rendering of CAD representation of the geometry for multiphase cases.

The geometry for the computational domain is dictated by an eccentric annulus of a 12–1/4" open-hole and 9 – 5/8" casing, where the eccentricity is fixed by a centralizer. The blade-height of the centralizer gives an eccentricity of 0.5, or 50 % stand-off. The centralizer is not included in the computational domain but used as a geometric restriction during the creation of the CAD-model.

The length of the domain is 24 m, to re-create a wellbore-section of two casing joints. The domain is split in half, due to symmetry, and for reducing computational time in half.

## Mesh

For the geometry of the domain, the grid generation resulted in 4.500.000 cells, structured with hex-cells. The mesh is generated with a sweeping method after specifying the desired amount of cells of the outer perimeter, inner perimeter, and high- and low-side symmetry



faces. A trial-and-error approach was performed to create a mesh with high-quality cells. Details of the mesh statistics and mesh metrics can be seen in Appendix. A.2.2.

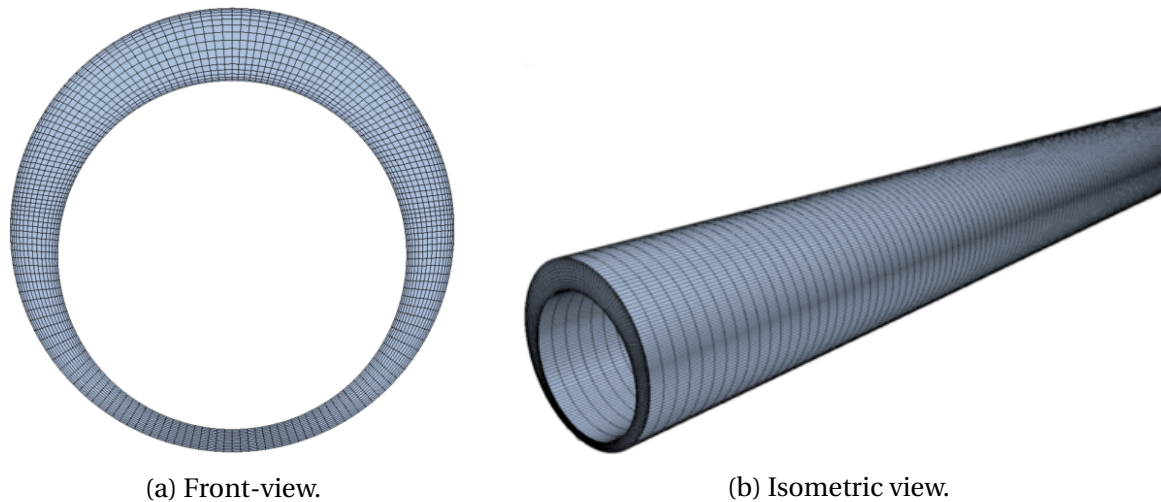


Figure 7.2.: The generated structured hex-mesh for the multiphase cases.

## Rheology

Datasheets for viscometer experiments, which were performed by Schlumberger and MI-Swaco, contain a six-range viscometer data for each fluid of interest. Importing the experimental data of the rheologies gave the result seen in Table. 7.1.

The result from the tests shows that all three rheologies gave best coinciding with the Herschel-Bulkeley model, of the four rheological models that were compared. This can be observed in Fig. A.1, where rheology analysis was performed for all three fluids, using a self-developed code in *MatLab* for obtaining the rheology data.

Table 7.1.: Rheological parameters of drilling mud (WBM), spacer (Mudpush II) and cement (9-5/8" tail cement).

<b>Fluid</b>	<b>Density, <math>\rho</math></b> <b>[kg/s]</b>	<b>Yield Point, <math>\tau_0</math></b> <b>[Pa]</b>	<b>Flow</b> <b>behaviour</b> <b>index, <math>k</math> [Pa·s<sup><i>n</i></sup>]</b>	<b>Consistency</b> <b>index, <math>n</math> [ ]</b>
Mud	1258	5.1367	0.8864	0.5188
Spacer	1200	4.6962	0.6342	0.4926
Cement	1900	2.2634	0.7688	0.5582

### Boundary Conditions

To simulate the desired operational volumetric flow rate of 900 LPM, this was converted to constant velocity inlet of 0.5183 m/s. Due to modelling three different fluids, a time was set for the injection of each fluid. Before solution initialization, the first fluid for the fluid train, which was the drilling mud, the fluid was initialized throughout the domain. Starting the calculation was done by introducing the spacer from 0 to 800 seconds. The inlet velocity distribution was uniform at the face of the inlet. Cement was introduced after 800 seconds until the stopping criteria of 1860 seconds. For the outlet, a pressure of 0 Pa was used by employing a pressure outlet. All boundary conditions used can be seen in Table. 7.2.

Table 7.2.: Boundary conditions used for eccentricity cases.

<b>Boundary</b>	<b>Boundary Type</b>	<b>Value</b>
Inlet	Velocity inlet	0.5183 m/s
	Spacer injection	$0s < t < 800s$
	Cement injection	$800s < t < 1860s$
Outlet	Pressure outlet	0 Pa
Wall	No-slip condition	-
Symmetry	Symmetry plane	-

### 7.1.1. Solver Settings

Details regarding the solver settings are shown in Table. 7.3.

Table 7.3.: Solver settings for eccentricity cases.

<b>Properties</b>	<b>Settings</b>
Software	ANSYS Fluent 19.0
Calculation	Transient
Solver Type	Pressure-Velocity Coupling
Solver Algorithm	Transient SIMPLE
Time Step	$10^{-5}$ seconds
Maximum Iterations	30 per time step
<b>Discretized Equations</b>	<b>Differencing scheme</b>
Gradient	Least squares cell-based
Pressure	Second-order Upwind
Momentum	Second-order Upwind
Volume Fraction	Second-order Upwind

From the initial two-phase cases run, divergence and convergence issues were preeminent. To solve this, change of cell-sizes and time-step were performed in conjunction with a change of URF's. The chosen values of URF are seen in Table. 7.4.

Table 7.4.: Under-relaxation factors implemented for multiphase case.

<b>Under-Relaxation Factors</b>	<b>Settings</b>
Pressure	0.2
Density	1.0
Body forces	1.0
Momentum	0.45
Volume Fraction	0.4

Due to the desired fluid train simulation, the flow initialization for the displacing fluids, spacer, and cement, is seen in Table. 7.2, where the stopping criteria were set for the cement after 1860 seconds of physical time.

7.1.2. Schematic of present CFD set-up

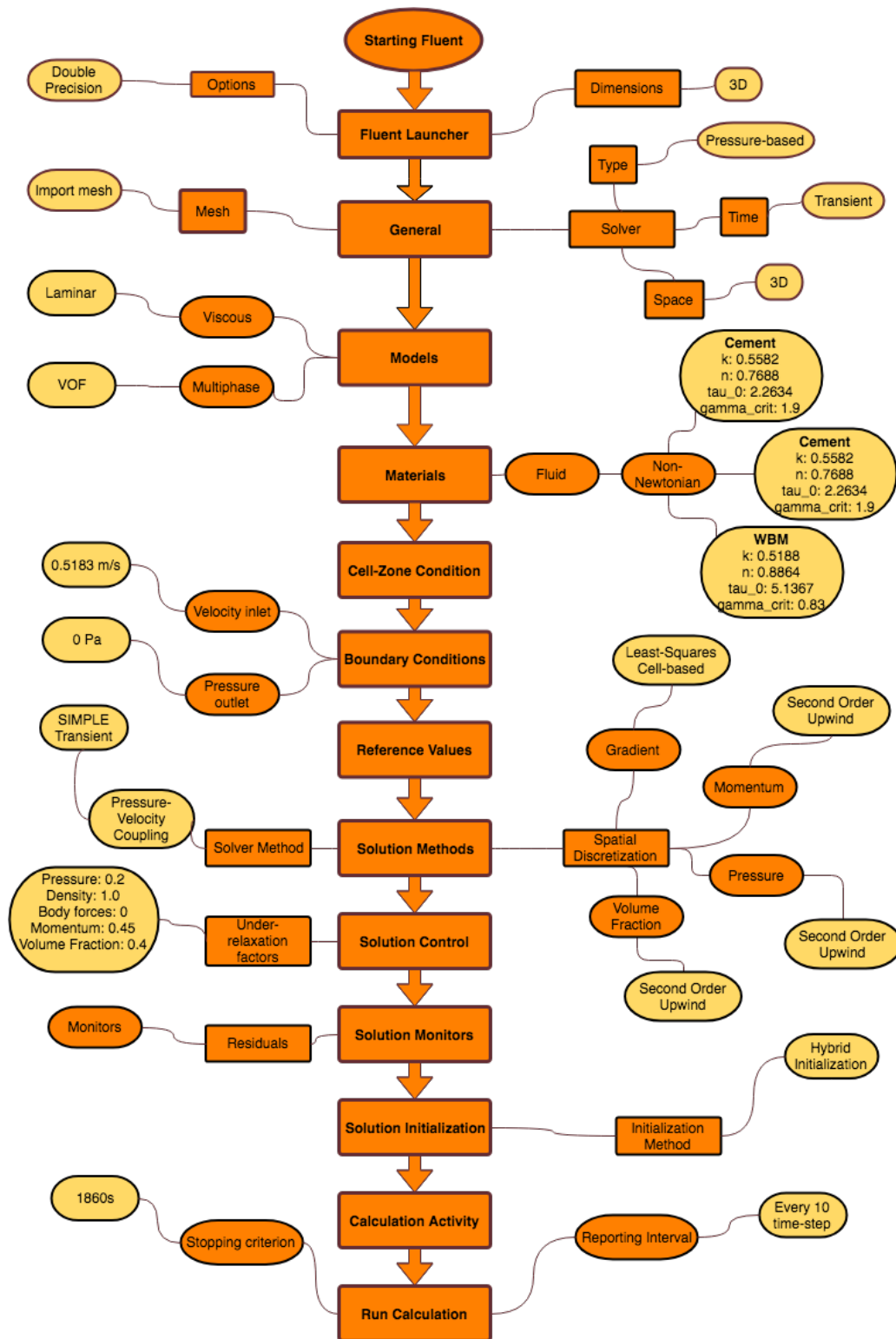


Figure 7.3.: Schematic of CFD set-up in *Fluent* for performing three-phase simulations.

### 7.1.3. Results

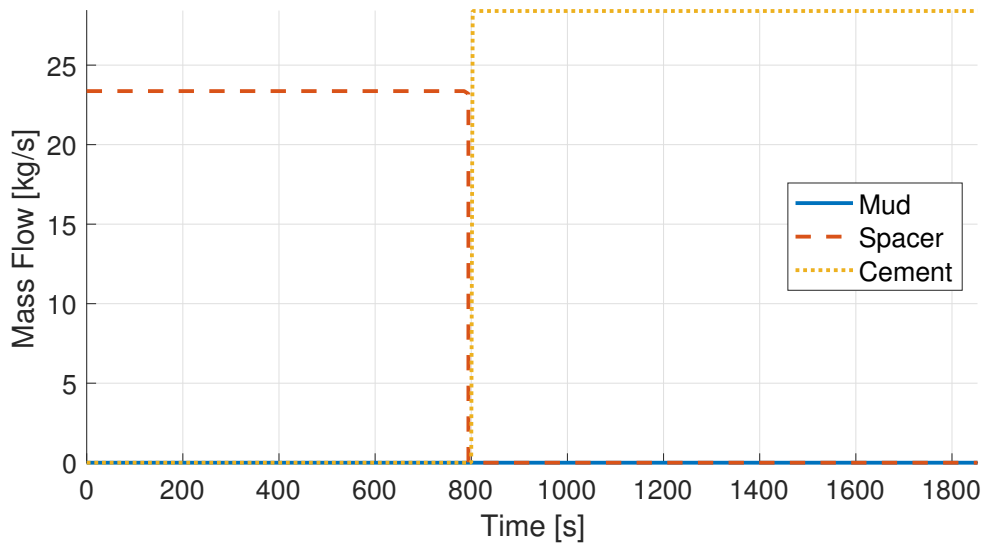


Figure 7.4.: Inflow of mud, spacer and cement vs. elapsed time.

For the data acquisition from the simulations, the inflow of the fluids was tracked, in order to ensure that simulations were performed correctly. This is seen in Fig. 7.4. As observed, the mass flow of mud is zero at the inlet. The simulation was initialized with the drilling mud throughout the domain. The simulation started with the inflow of spacer fluid, and after the specified time, inflow of cement.

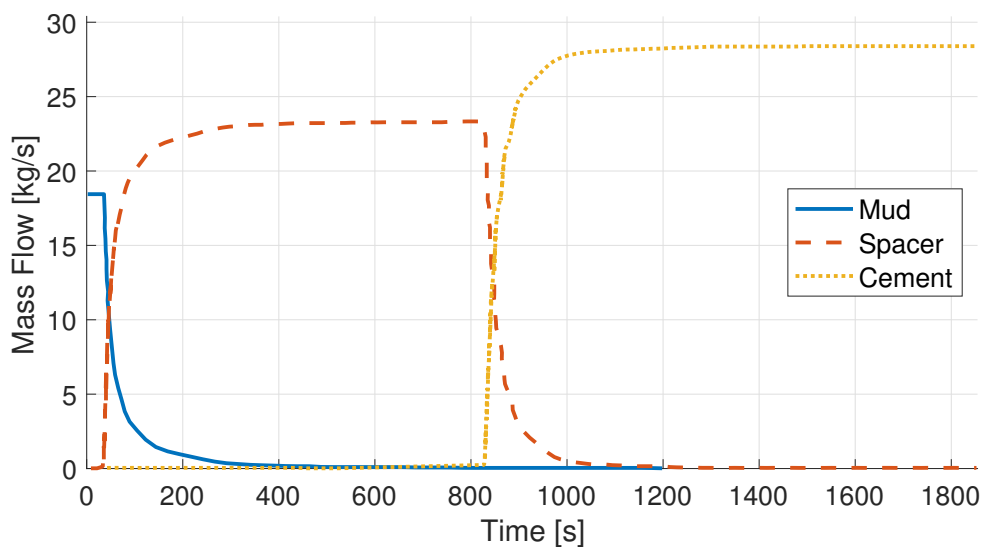


Figure 7.5.: Outflow of mud, spacer and cement vs. elapsed time.

The outflow of fluids was also tracked, seen in Fig. 7.5. After 36 seconds, the mass flow rate and drilling mud started to decline, indicating the mud exiting the domain of 24m. It is observed that the mass flow of mud does not reach a minima until after around 500 seconds. Initialization of spacer displacement and cement breakthrough was observed at 820s elapsed time, whereafter the spacer flow rate rapidly declines. As a result, this indicates that the displacement of cement is propagating through the annulus, reaching the outlet.

Table 7.5.: Volume Fraction of the three-phases at 31min.

Fluids	Volume Fraction
Mud	0.0014
Spacer	0.0033
Cement	0.9953

The displacement of the volume fraction can be observed in Fig. 7.6. The spacer breakthrough is at the time 0 s and rapidly increasing until the spacer plateau is reached. It is observed that the spacer plateau is not retained for long due to the cement breakthrough at 800s elapsed time. As the cement is displaced, the cement plateau region is reached at approximately 1500s. Furthermore, the presented graphs show no instabilities, indicated by the smooth transition in Fig. 7.4, 7.5 and 7.6.

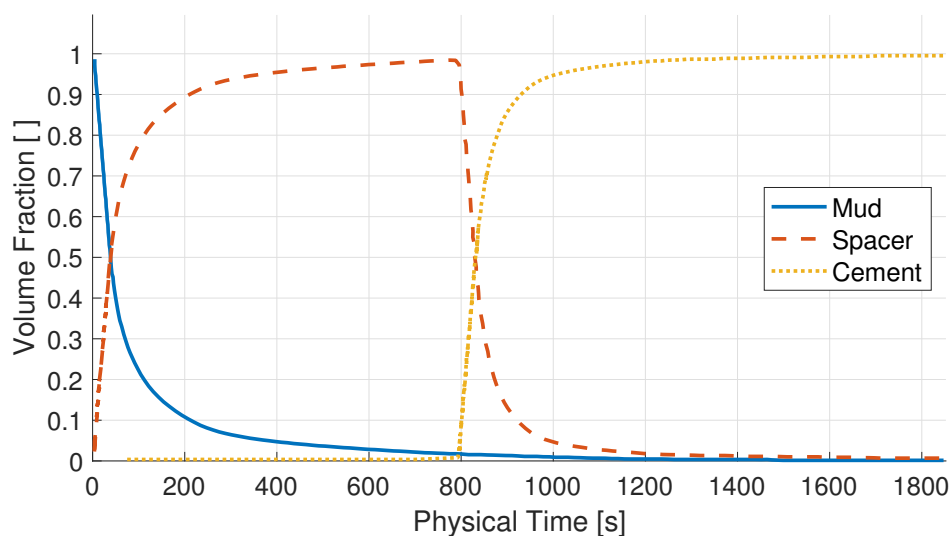




Figure 7.6.: Displacement of mud, spacer and cement vs. elapsed time.

Mud   
Spacer 



(a) Solution at 150 seconds.



(b) Solution at 200 seconds.



(c) Solution at 240 seconds.



(d) Solution at 400 seconds.

Figure 7.7.: Displacement of mud by spacer for the elapsed solution time for a section of the annulus.

In Fig. 7.7, four snapshots give a representation of the displacement profile, interface, and fluid transportation for mud and spacer at given times from an outside point-of-view. This representation is created because the displacement near the wellbore wall is of importance. At inspection, the interface between the two fluids shows the moving front, with characteristics of the same velocity profiles seen for the single-phase case in Fig. A.17 for the 50 % stand-off case. The viewpoint is tilted such that the low-side of the annulus is available for visual observation. Even though the front shows a marked velocity deficit, the front on the low-side is still significant enough in order to displace the mud. Overall, it can be seen that the mud-spacer displacement is of an important effect.

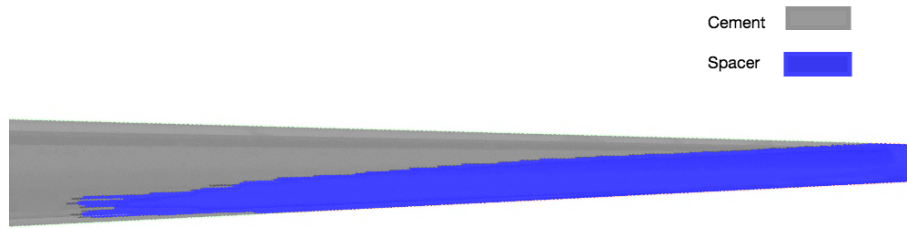
In Fig. 7.8, the displacement of spacer-cement can be observed. As for the mud-spacer, the spacer-cement representations are taken at four time-instances, to see the displacement and flow propagation. It is observed that the interface, or front, of the cement, displacing the spacer, shows larger velocity profile, which means that the eccentricity effects are more significant for spacer-cement, compared to mud-spacer. As observed previously, the low-side flow propagation shows the same effects for spacer-cement displacement, where the cement velocities at the low-side are significant enough to displace the spacer fluid. It can also be seen that the interface at the low-side exhibits a sharper contour compared to the mud-spacer case, where it was more rounded. It displays the effects of the computation at the interface struggle to compute the smooth profile, seen previously for the single-phase case in Fig. 6.16b.

For the different fluids, the relevant Reynolds numbers based on Madlener et al. is seen in Tab. 7.6.

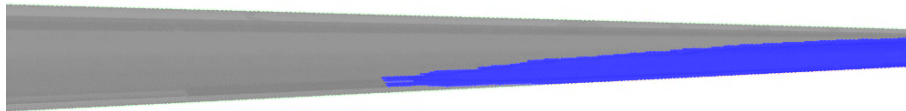
Table 7.6.: The Reynolds numbers computed for the three different fluids, where the second column is the conventional Reynolds number calculation, and the third and fourth is based on the expressions presented by Madlener et al.

<b>Fluid</b>	$Re$	$Re_{HB}$	$Re_{GenHB}$
Mud	1499	279	74
Spacer	1476	368	105
Cement	447	241	97

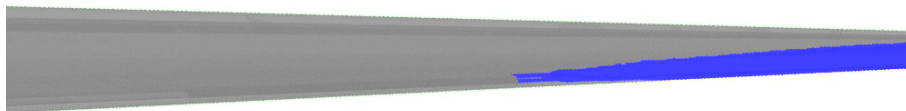




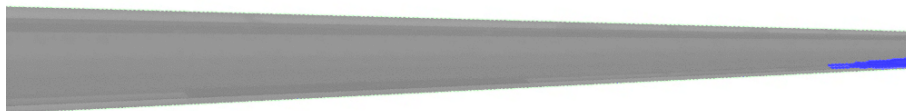
(a) Solution at 920 seconds.



(b) Solution at 980 seconds.



(c) Solution at 1020 seconds.



(d) Solution at 1200 seconds.

Figure 7.8.: Displacement of spacer by cement for the elapsed solution time for a section in the annulus.

#### 7.1.4. Displacement Efficiency

For the specific mud-spacer-cement displacement analysis, the displacement efficiency is listed in the Tab. 7.7, below.

Table 7.7.: Displacement efficiency of the fluid train at 31min.

<b>Fluids</b>	<b>Displacement Efficiency</b>
Mud-Spacer	98.43 %
Spacer-Cement	99.53 %

As presented, the displacement efficiency shows satisfactory results for mud-spacer and spacer-cement fluid interaction. With the stand-off of interest, the effect of eccentricity does not inhibit the displacement efficiency of the fluid train. As observed previously, the eccentric configuration has an impact on the velocity profile of the moving front, where higher channelization is observed for spacer-cement and less for spacer-cement. Overall, the effects of channelization are present to a significant degree.

These results show that with the operational procedure that is analyzed, exhibit no significant displacement issues in a horizontal wellbore of 9 – 5/8" casing in a 12 – 1/4" open-hole occur. This may be due to several factors, that will be discussed below.

From the results of Zulqarnain & Tyagi, their fluid-fluid analysis, utilizing the VOF method, showed a high degree of instability effects of the fluids of interest. As seen in Fig. 7.9, the displacement of the fluid train is quantitatively different from the results of the present study. It can be observed that displacement of the near-wall effects contributed to inadequate displacement, which may result in a poor bonding of cement in the annulus.

It can be mentioned that the presented case is for a 2D CFD analysis of concentric annuli with fluids exhibiting power-law behaviour, which is quite different from the Herschel-Bulkeley model, due to the absence of the yield stress parameter in the fluid.

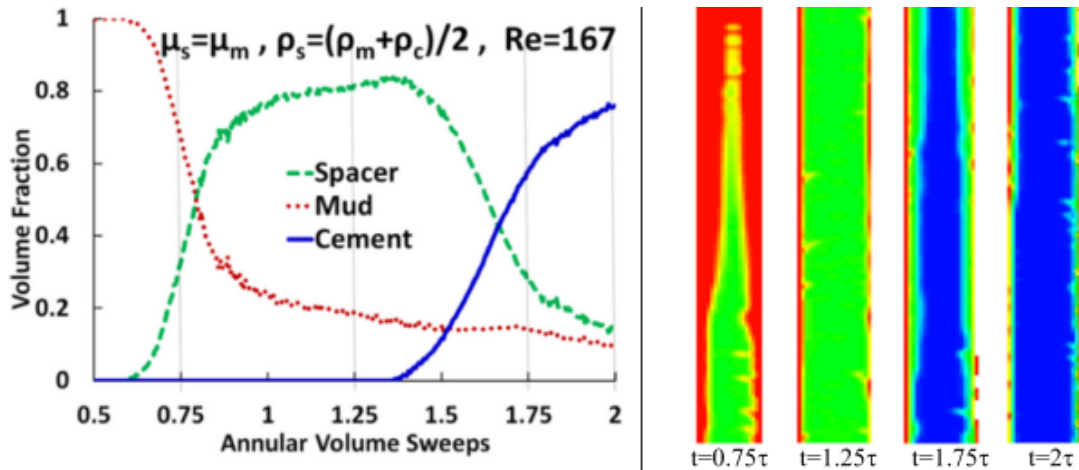


Figure 7.9.: Results from one of the cases performed by Zulqarnain & Tyagi for mud-spacer-cement analysis showing instabilities.

Zulqarnain & Tyagi discuss the role of interfacial instability, such as Rayleigh-Taylor instabilities, due to the displacement of fluids with a high difference in density, and Saffmann-Taylor instabilities, due to the displacement of fluids with different viscosity which, may result in viscous fingering in at the interface. These instabilities are also highly dependent on the flow regime of the flow. The authors also observed fluctuations as the Reynolds number was over 400, where the volume fraction showed instability effects in the annulus.

For the present studies, these effects were not present which may be a result of the satisfactory fluid composition of the mud, spacer, and cement. The rheology characteristics may have been tailored in a proper way, such that the fluid interaction and dispersion between two fluids are kept to a minimum. It can be noted that the effects of this may also be due to insufficient CFD modelling, which does not capture these effects with the present CFD model presented in this study. Some of the issues with resolving the interface due to unsatisfactory CFD implementation may stem from three sources which will be addressed.

Firstly, the pressure interpolation scheme that was chosen. As long as the pressure variation between cells is smooth, the linear interpolation scheme will yield accurate pressure predictions. However, if there is a presence of large gradients in the source in the momentum terms between the cells, the pressure profile may exhibit in high gradients. If this is to occur, the chosen interpolation scheme may give poor results. With improper pressure interpolation, the effect may be an under-prediction or over-prediction the velocity. This will

consequently change the profile of the interface. A higher-order interpolation scheme may result from issues of predicting the pressure gradient at these locations. Another source of error may also be the assumption of zero pressure gradient at the wall. The assumption is valid in the presence of boundary layers but may result in errors for high body forces and curvature, which consequently affect the pressure gradient. The failure to account for the wall pressure gradient will influence the velocity in the proximity of the wall.

Secondly, the mesh used for the multiphase case. Based on the assumptions discussed above, a refined mesh in regions of high-gradients may resolve the pressure variations more adequately. Due to computational time and diverging simulations, generation of a suitable mesh and selecting a proper time step was proven to be a difficult task. More effort should have been spent on mesh refinement for a stable converging simulation which may have yielded better interface prediction.

Lastly, a better-suited method for calculating the interface should be considered. The chosen donor-acceptor method resolves the interface in a much more effective way in terms of computational costs, but at the sacrifice of accuracy. A more suitable method will be the geometric reconstruction method, which interpolates the interface with a higher degree of accuracy. It can be mentioned that computational time may be a limiting factor, due to the complexity of multiphase modelling. This should be kept in mind when choosing more accurate methods. Furthermore, since the displacement efficiency is not directly correlated to detailed interface calculations, it was expected to be as a less important factor for the simulations.

# Conclusion

---

Based on the CFD simulations performed and literature surveyed in this thesis in order to understand the primary cementing process, the following conclusion may be stated:

1. A CFD approach for 3D analysis may yield a satisfactory representation of the flow characteristics of non-Newtonian fluids exhibiting Herschel-Bulkley behaviour. Velocity profiles, pressure drop, and flow development can be readily acquired for analysis of the flow.
2. The eccentricity/stand-off should be kept at a tolerated limit, as it highly affects the flow characteristics in the annulus. For annular flow with eccentricities above 0.5, high-side channeling and plug flow behaviour was observed for Herschel-Bulkley fluids.
3. The frictional pressure drop estimation may be calculated with the basis of CFD results of a concentric annulus in conjunction with the correlation factor presented by Hacıislamoglu [27] and Madlener et al. [25] for quick calculations of pressure drop for eccentric annuli.
4. An increase of geometry complexity, such as wall roughness and non-smooth wellbore may capture the effects of displacement issues, which was not observed with the assumption of smooth walls for the present study. A more realistic representation of the geometry of the wellbore may reveal effects which will influence the displacement to a higher degree.
5. Further increase of modelling the complexity of the proposed CFD models may yield

---

more accurate results and a better flow representation of multiphase effects and instabilities. Furthermore, the flow regimes at a higher Reynolds number which is under the limit of fracture pressure should be studied further.

6. Validation of proposed CFD models against experimental data of the same case should be obtained for increased confidence in the CFD results. For any experimental set-up, a focus on proper rheology composition is of importance, since the flow behaviour highly depends on the rheology parameters.
7. CFD-based correlations may be an adequate tool to quantify displacement efficiency, but need further investigation to enhance accuracy and applicability for operational conditions.

# References

---

- [1] Stick-slip. <https://www.tomax.no/resources/about-stick-slip/>. Accessed: 2018-05-20.
- [2] What is mpd? <http://www.beyondenergy.ca/mpd/>. Accessed: 2018-05-20.
- [3] Sweatman R. *Well Cementing Operations*. IADC, 1st edition edition, 2018.
- [4] Crook et. al. Eight steps to ensure successful cement jobs. *Oil & Gas Journal*, 99:37–43, july 2001.
- [5] Hacıislamoglu M. *Non-Newtonian Fluid Flow in Eccentric Annuli and Its Application to Petroleum Engineering Problems*. PhD dissertation, Louisiana State University, 1989.
- [6] Peng et. al. General method of calculating annular laminar pressure drop of drilling fluids with different rheological models. *Petroleum Exploration and Development*, 40(6):806–810, dec 2013.
- [7] Zulqarnain M. and Tyagi M. Development of simulations based correlations to predict the cement volume fraction in annular geometries after fluid displacements during primary cementing. *Journal of Petroleum Science and Engineering*, 145:1–10, sep 2016.
- [8] Flow properties of polymers: Time-independent fluids. <http://polymerdatabase.com/polymer%20physics/Viscosity2.html>. Accessed: 2017-18-12.
- [9] Bittleston S. and Guillot D. Mud removal: Research improves traditional cementing guidelines. *Oilfield Review*, 1991.

- [10] Bratland O. *Pipe Flow 2: Multi-phase Flow Assurance*. drbratland.com, 1st edition edition, 2013.
- [11] ANSYS Inc. Ansys fluent 12.0/12.1 documentation. 2017.
- [12] Computational fluid dynamics. [http://www.menet.umn.edu/shen/1\\_cfd.html](http://www.menet.umn.edu/shen/1_cfd.html). Accessed: 2018-06-02.
- [13] Parmar M. Solution methods. <https://www.slideshare.net/MehulParmar53/solution-methods>. Accessed: 2018-06-03.
- [14] Arato A. et. al. Staggered grid inversion of cross hole 2-d resistivity tomography. *Journal of Applied Geophysics*, 107(Supplement C):60 – 70, 2014.
- [15] Versteeg H. and Malalasekera W. *An Introduction to Computational Fluid Dynamics*. Pearson Education Ltd., 2 edition, 2009.
- [16] Owen S.J. et. al. Pyramid elements for maintaining tetrahedra to hexahedra conformability. 220:123 – 129, 01 1997.
- [17] Owen S.J. et. al. Q-morph: an indirect approach to advancing front quad meshing. *International Journal for Numerical Methods in Engineering*, 44(9):1317–1340.
- [18] Sauer C.W. Mud displacement during cementing state of the art. *Journal of Petroleum Technology*, 39(9):1091–1101, 1975.
- [19] Savery M., Chin W., and Krishna Y. Modeling cement placement using a new 3-d flow simulator. In *AADE-08-DF-HO-08*, AADE Fluids Conference, Houston, Texas, 2008. American Association of Drilling Engineers.
- [20] Lavrov A. and Torsæter M. *Physics and Mechanics of Primary Well Cementing*. Springer, Trondheim, Norway, 2016.
- [21] Shadravan et. al. Engineering the Mud-Spacer-Cement Rheological Hierarchy Improves Wellbore Integrity, 2015.
- [22] Nelson E. and D. Guillot. *Well Cementing*. Developments in petroleum science. Schlumberger, 2006.



- 
- [23] Khalilova et. al. Newtonian Fluid in Cementing Operations in Deepwater Wells: Friend or Foe?
- [24] Metzner A.B. and J.C. Reed. Flow of non-newtonian fluids—correlation of the laminar, transition, and turbulent-flow regions. *AIChE Journal*, 1(4):434–440, 1955.
- [25] Madlener K., Frey B., and Ciezki H. K. Generalized reynolds number for non-newtonian fluids. In Array, editor, *EUCASS Proceedings Series – Advances in AeroSpace Sciences*, volume 1, pages 237–250, 2009.
- [26] Langlinais J.P, Bourgoyne A.T., and Holden W.R. Frictional pressure losses for annular flow of drilling mud and mud-gas mixtures. *Journal of Energy Resources Technology*, 107(1):142 – 151, 1985.
- [27] Hacıislamoglu M. and Langlinais J. Non-Newtonian Flow in Eccentric Annuli. *Journal of Energy Resources Technology*, 112:163–169, 1990.
- [28] Sorgun M. and Ozbayoglu M.E. Predicting frictional pressure loss during horizontal drilling for non-newtonian fluids. *Energy Sources, Part A: Recovery, Utilization, and Environmental Effects*, 33(7):631–640, 2011.
- [29] Sorgun M. Computational fluid dynamics modeling of pipe eccentricity effect on flow characteristics of newtonian and non-newtonian fluids. *Energy Sources, Part A: Recovery, Utilization, and Environmental Effects*, 33(12):1196–1208, 2011.
- [30] Fredrickson A. and R. Bird. Non-newtonian flow in annuli. *Industrial & Engineering Chemistry*, 50(3):347–352, 1958.
- [31] Rushd et al. Cfd simulation of pressure losses in eccentric horizontal wells. In *In SPE Middle East Oil Gas Show and Conference, 6-9 March Manama, Kingdom of Bahrain*. Society of Petroleum Engineers, 2017.
- [32] Zhigarev et. al. Studying laminar flows of power-law fluids in the annular channel with eccentricity. *Journal of Physics: Conference Series*, 899(9):092016, 2017.
-

- [33] Mao et al. Modeling and numerical simulation of yield viscoplastic fluid flow in concentric and eccentric annuli. *Chinese Journal of Chemical Engineering*, 20(1):191 – 202, 2012.
- [34] Podryabinkin et al. Detailed Modeling of Drilling Fluid Flow in a Wellbore Annulus While Drilling, 2013.
- [35] Enayatpour S. and van Oort E. Advanced modeling of cement displacement complexities. SPE/IADC Drilling Conference and Exhibition, 14-16 March, The Hague, The Netherlands, 2017. Society of Petroleum Engineers.
- [36] Chhabra R.P. and Richardson J.F., editors. *Non-Newtonian Flow and Applied Rheology*. Butterworth-Heinemann, Oxford, 2nd edition, 2008.
- [37] Ofei T. Effect of yield power law fluid rheological properties on cuttings transport in eccentric horizontal narrow annulus. *Journal of Fluids*, vol. 2016, 2016.
- [38] Brennen C. *Introduction to Multiphase Flow*. Cambridge University Press, 2005.
- [39] Andersson et. al. *Computational Fluid Dynamics for Engineers*. Cambridge University Press, 2012.
- [40] Brackbill et. al. A continuum method for modeling surface tension. *Journal of Computational Physics*, 100(2):335 – 354, 1992.
- [41] Courant R. et. al. On the solution of nonlinear hyperbolic differential equations by finite differences. *Communications on Pure and Applied Mathematics*, 5(3):243–255, aug 1952.
- [42] Lax P.D. Hyperbolic difference equations: A review of the courant-friedrichs-lewy paper in the light of recent developments. *IBM Journal of Research and Development*, 11(2):235–238, March 1967.
- [43] Valenta P. Beam–Warming Second-Order Upwind Method. 2015.
- [44] Scarborough J.B. *Numerical mathematical analysis*. Baltimore : Johns Hopkins Press, 4th edition edition, 1958. Includes index.

- 
- [45] Roache P.J. *Fundamentals of Computational Fluid Dynamics*. Hermosa Publisher, 0th edition edition, 1976.
- [46] Rhie C.M. and Chow W.L. Numerical study of the turbulent flow past an airfoil with trailing edge separation. *AIAA Journal*, 21(11):1525–1532, nov 1983.
- [47] Anderson K. and Bonhaus D. An implicit upwind algorithm for computing turbulent flows on unstructured grids. *Computers & Fluids*, 23(1):1 – 21, 1994.
- [48] Barth T. and Jespersen D. The design and application of upwind schemes on unstructured meshes. In *Technical Report AIAA-89-0366*, AIAA 27th Aerospace Sciences Meeting, Reno, Nevada, 1989. American Institute of Aeronautics and Astronautics.
- [49] Farooq M.A. and Müller B. A cartesian grid method for compressible flows to compute shock waves. In *Proceedings of 2012 9th International Bhurban Conference on Applied Sciences Technology (IBCAST)*, pages 274–282, Jan 2012.
- [50] Xia J.L. et. al. Effect of inlet and outlet boundary conditions on swirling flows. *Computers Fluids*, 26(8):811 – 823, 1997.
- [51] Rapaport et al. Iterative methods used in overlap astrometric reduction techniques do not always converge. *Journal of Astronomy and Astrophysics*, 271(3):645–648, 1993.
- [52] Rhie C.M. and Chow W.L. Numerical study of the turbulent flow past an airfoil with trailing edge separation. *AIIA Journal*, 21(6), 1983.
- [53] Harlow F.H. and Welch J.E. Numerical calculation of time-dependent viscous incompressible flow of fluid with free surface. *Physics of Fluids*, 8:2182–2189, 1965.
- [54] Patankar S.V. and Spalding D.B. A calculation procedure for heat, mass and momentum transfer in three-dimensional parabolic flows. *International Journal of Heat and Mass Transfer*, 15(10):1787 – 1806, 1972.
- [55] Chau-Nguyen et. al. A polytree-based adaptive polygonal finite element method for multi-material topology optimization. 08 2017.
-

- [56] Mavriplis J. Chapter 7 - mesh generation and adaptivity for complex geometries and flows. In Roger Peyret, editor, *Handbook of Computational Fluid Mechanics*, pages 417 – 459. Academic Press, London, 1996.
- [57] Skåre P.E. and Krogstad P.-Å. A turbulent equilibrium boundary layer near separation. *Journal of Fluid Mechanics*, 272:319–348, 1994. cited By 166.
- [58] Bharat K.S. Grid generation for internal flow configurations. *Computers Mathematics with Applications*, 24(5):191 – 201, 1992.
- [59] Harris M.J. *Flow Feature Aligned Mesh Generation and Adaption*. PhD dissertation, University of Sheffield, 2013.
- [60] Thompson et al. *Numerical Grid Generation: Foundations and Applications*. Elsevier North-Holland, Inc., New York, NY, USA, 1985.
- [61] Nguyen T. *Non-Newtonian Fluid Displacement in Downhole Horizontal Annulus*. PhD thesis, Norwegian University of Science and Technology, 2017.
- [62] Schlichting H. Boundary-layer theory. *ZAMM - Journal of Applied Mathematics and Mechanics / Zeitschrift für Angewandte Mathematik und Mechanik*, 60(4):217–217.
- [63] White F.M. *Fluid Mechanics*. McGraw-Hill Series in Mech. Eng., New York, NY, USA, 7 edition, 2011.

# Appendix



## A.1. Rheology Analysis

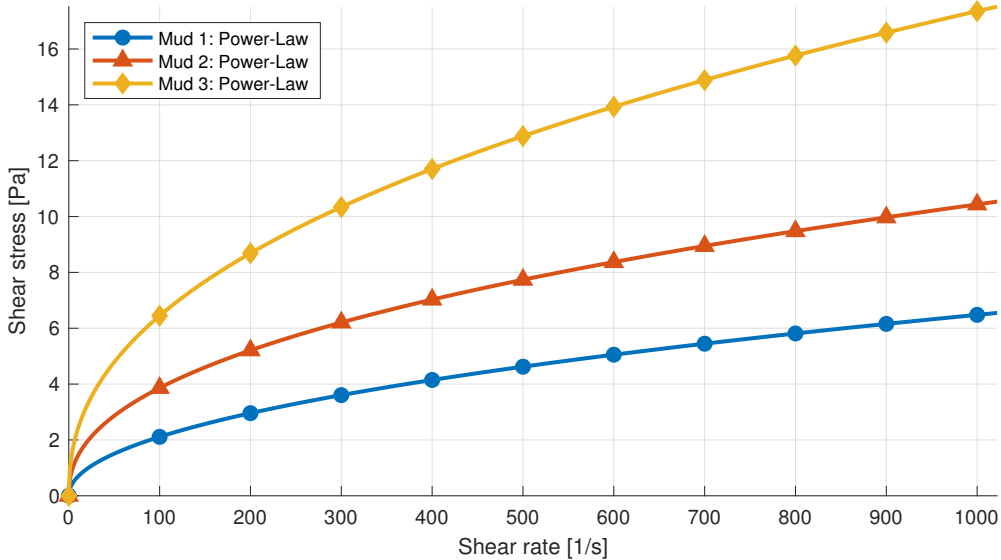


Figure A.1.: Strain rate vs. shear stress plot for the drilling fluids for Oswald de Waele model for the validation case.

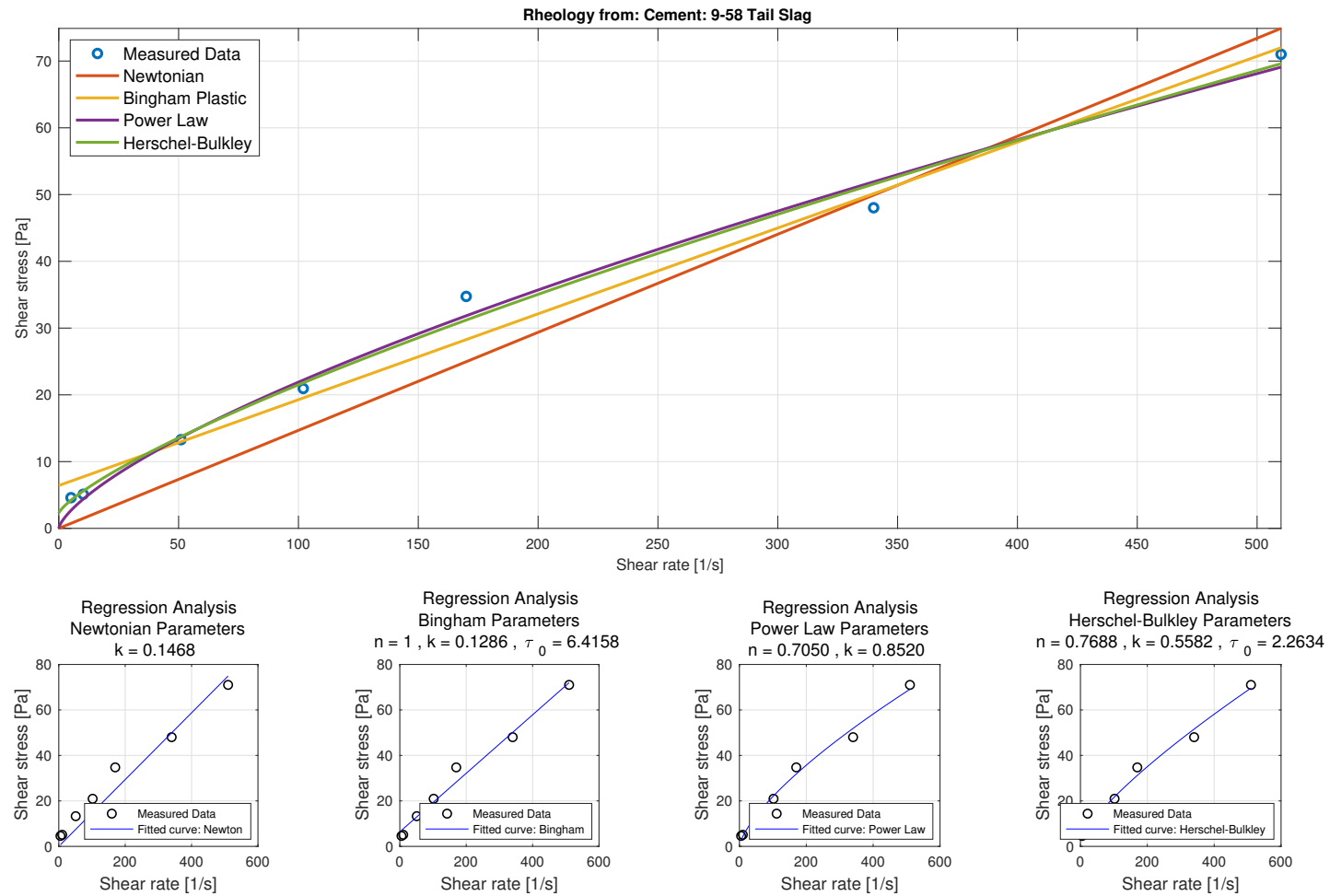


Figure A.2.: Rheology analysis performed for cement (9-5/8" Tail Slag, viscometer data by *Schlumberger*).

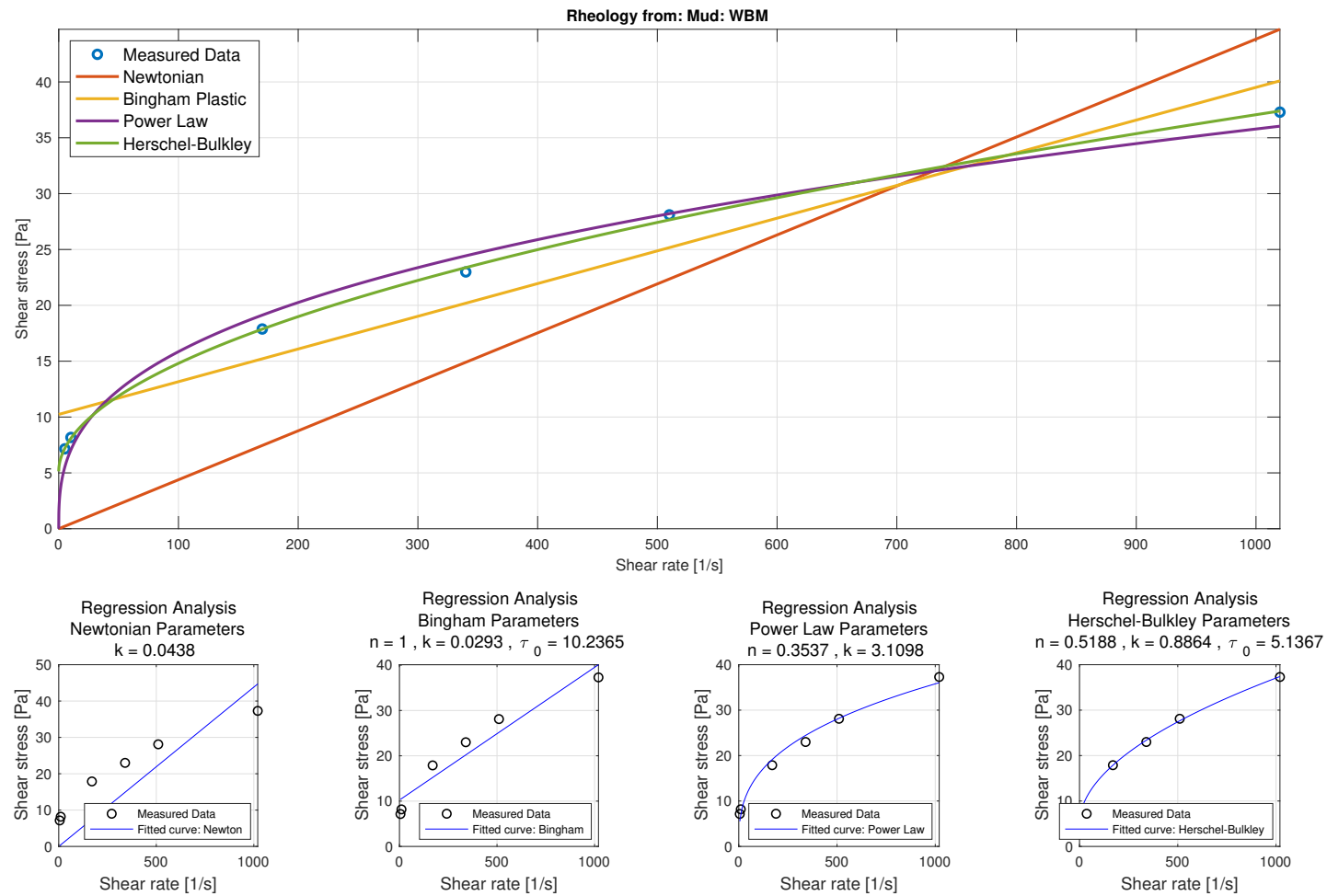


Figure A.3.: Rheology analysis performed for WBM (viscometer data by MI-Swaco).

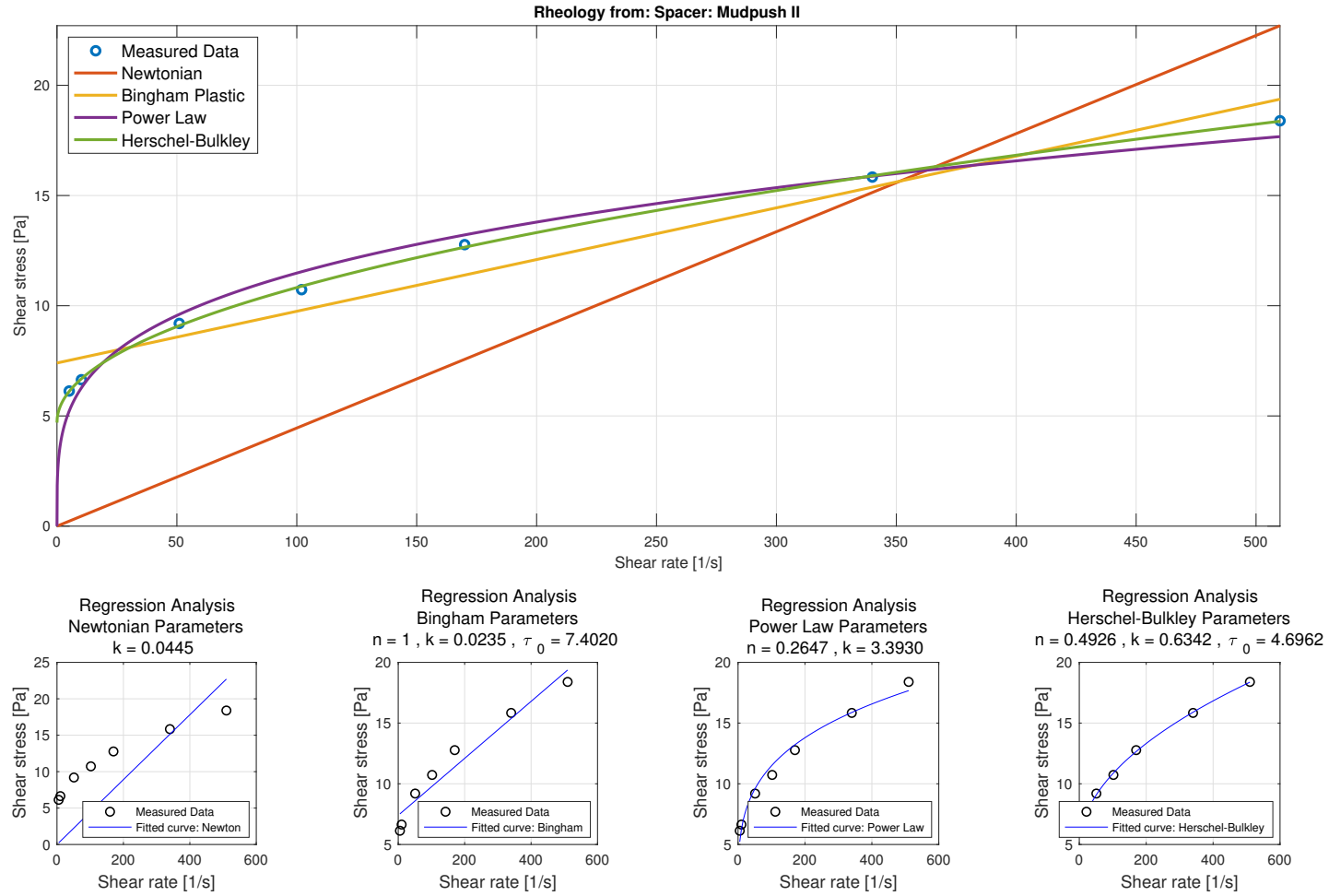


Figure A.4.: Rheology analysis performed for Spacer (Spacer-Mudpush II, viscometer data by Schlumberger.)



## A.2. Mesh Settings and Mesh Statistics

### A.2.1. Single-Phase - Eccentricity Case

Table A.1.: Mesh Settings and Statistics for: Stand-off 100%.

<b>Mesh Settings</b>	<b>Parameter</b>
Grid Classification	Structured
Cell Type	Hexahedron
Method	Sweep
Sweep size	25 mm
Relevance center	Fine
Maximum face size	10 mm
Minimum face size	1e-003 mm
<b>Mesh Statistics</b>	<b>Value</b>
Number of Elements	2 000 000
Maximum Skewness	0.001 (Excellent)
Minimum Orthogonal Quality	0.99988 (Excellent)

Table A.2.: Mesh Settings and Statistics for: Stand-off 75%.

<b>Mesh Settings</b>	<b>Parameter</b>
Grid Classification	Structured
Cell Type	Hexahedron
Method	Sweep
Sweep size	25 mm
Relevance center	Fine
Maximum face size	10 mm
Minimum face size	1e-003 mm
<b>Mesh Statistics</b>	<b>Value</b>
Number of Elements	2 000 000
Maximum Skewness	0.18086 (Excellent)
Minimum Orthogonal Quality	0.95992 (Excellent)

Table A.3.: Mesh Settings and Statistics for: Stand-off 50%.

<b>Mesh Settings</b>	<b>Parameter</b>
Grid Classification	Structured
Cell Type	Hexahedron
Method	Sweep
Sweep size	25 mm
Relevance center	Fine
Maximum face size	10 mm
Minimum face size	1e-003 mm
<b>Mesh Statistics</b>	<b>Value</b>
Number of Elements	2 000 000
Maximum Skewness	0.35323 (Very good)
Minimum Orthogonal Quality	0.84999 (Very good)

Table A.4.: Mesh Settings and Statistics for: Stand-off 25%.

<b>Mesh Settings</b>	<b>Parameter</b>
Grid Classification	Structured
Cell Type	Hexahedron
Method	Sweep
Sweep size	25 mm
Relevance center	Fine
Maximum face size	10 mm
Minimum face size	1e-003 mm
<b>Mesh Statistics</b>	<b>Value</b>
Number of Elements	3 000 000
Maximum Skewness	0.54989 (Good)
Minimum Orthogonal Quality	0.63797 (Very good)

Table A.5.: Mesh Settings and Statistics for: Stand-off 0%.

<b>Mesh Settings</b>	<b>Parameter</b>
Grid Classification	Structured
Cell Type	Hexahedron
Method	Sweep
Sweep size	25 mm
Relevance center	Fine
Maximum face size	10 mm
Minimum face size	1e-003 mm
<b>Mesh Statistics</b>	<b>Value</b>
Number of Elements	5 697 699
Maximum Skewness	0.59036 (Good)
Minimum Orthogonal Quality	0.22908 (Good)

## A.2.2. Multiphase - Three-phase Case

Table A.6.: Mesh Settings and Statistics for: Three-phase case.

<b>Mesh Settings</b>	<b>Parameter</b>
Grid Classification	Structured
Cell Type	Hexahedron
Method	Sweep
Sweep size	25 mm
Relevance center	Fine
Maximum face size	10 mm
Minimum face size	1e-003 mm
<b>Mesh Statistics</b>	<b>Value</b>
Number of Elements	4 500 000
Maximum Skewness	0.35323 (Very good)
Minimum Orthogonal Quality	0.84999 (Very good)

## A.3. Results - Eccentricity Cases: Pressure & Velocity Development

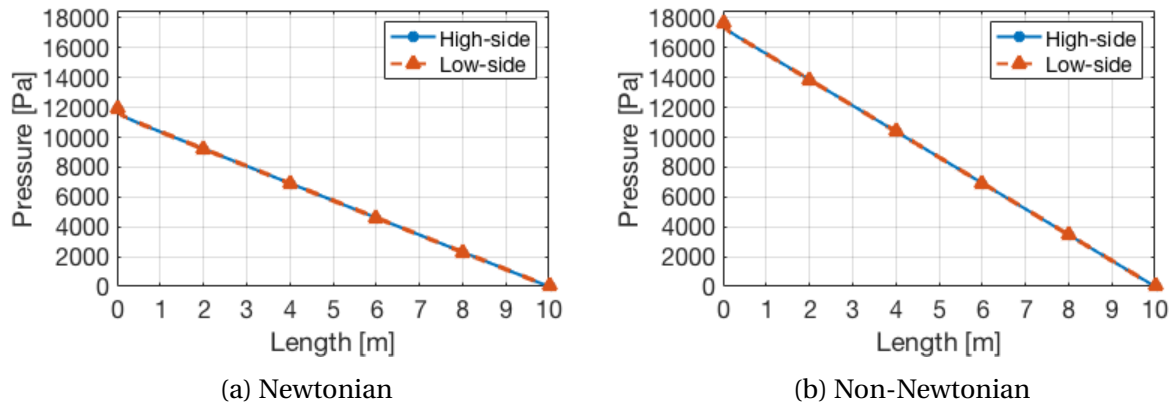


Figure A.5.: Comparison of pressure development for the eccentricity = 0 cases.

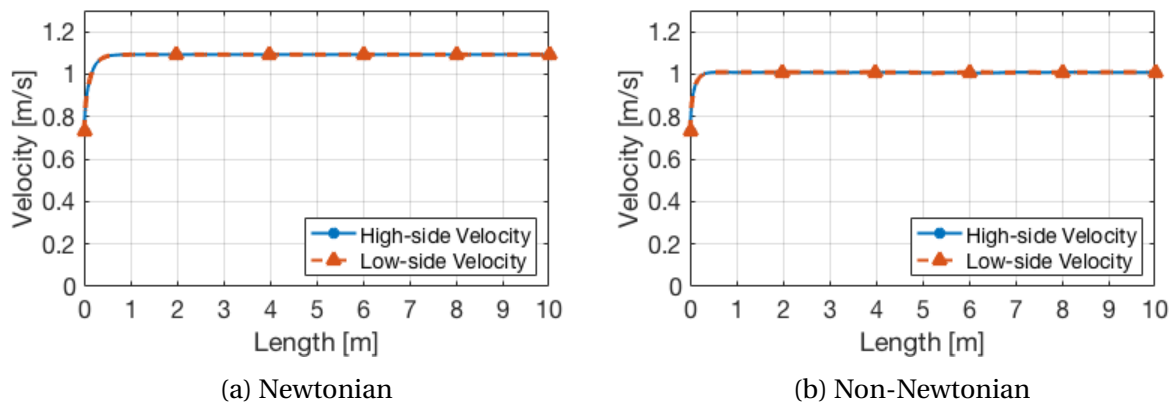


Figure A.6.: Comparison of velocity development for the eccentricity = 0 cases.

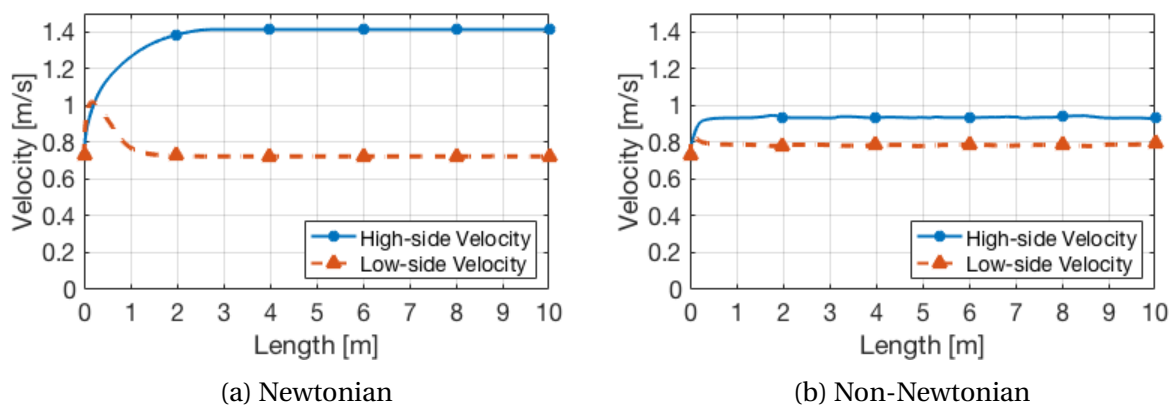


Figure A.8.: Comparison of velocity development for the eccentricity = 0.25 cases.

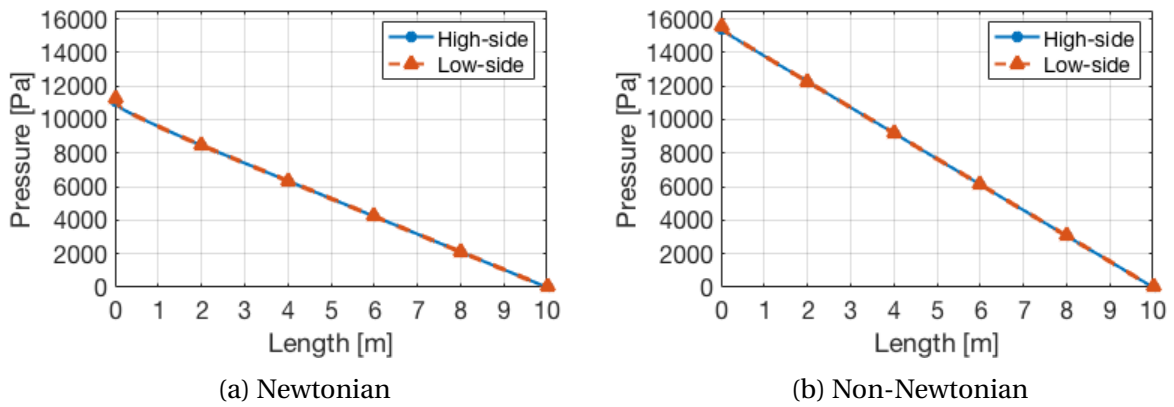


Figure A.7.: Comparison of pressure development for the eccentricity = 0.25 cases.

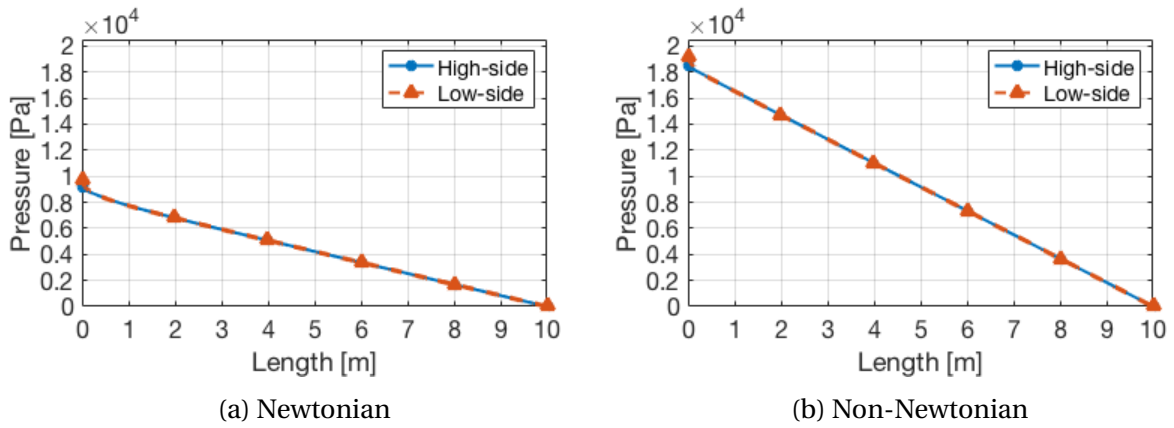


Figure A.9.: Comparison of pressure development for the eccentricity = 0.5 cases.

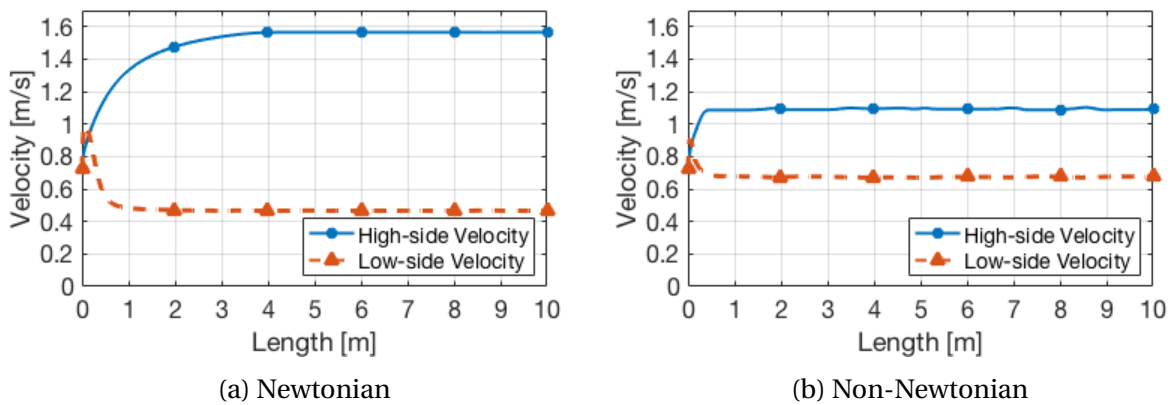
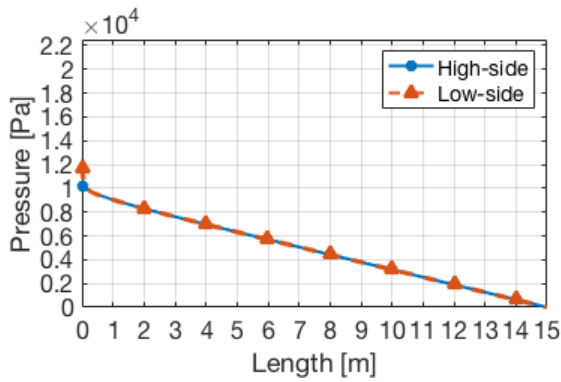
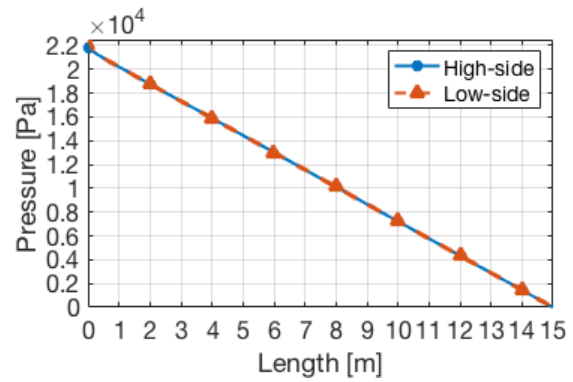


Figure A.10.: Comparison of velocity development for the eccentricity = 0.5 cases.

### A.3. RESULTS - ECCENTRICITY CASES: PRESSURE & VELOCITY DEVELOPMENT

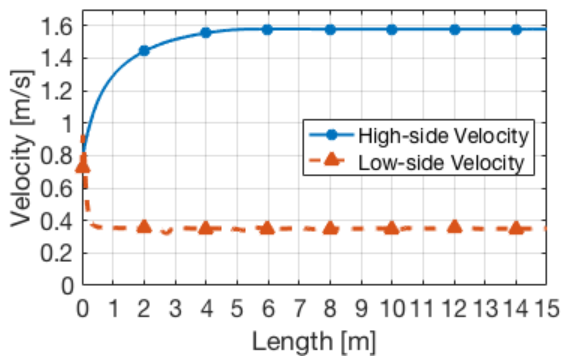


(a) Newtonian

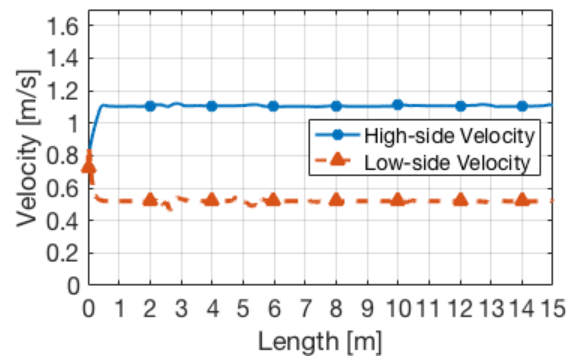


(b) Non-Newtonian

Figure A.11.: Comparison of pressure development for the eccentricity = 0.75 cases.

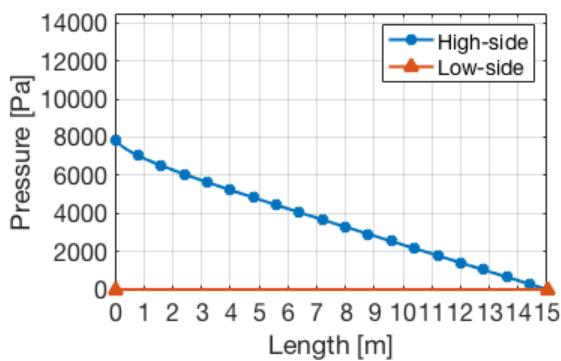


(a) Newtonian

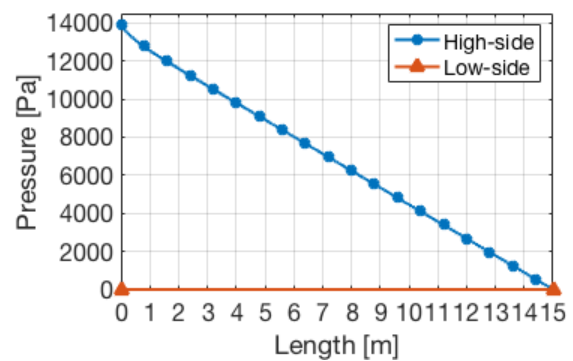


(b) Non-Newtonian

Figure A.12.: Comparison of velocity development for the eccentricity = 0.75 cases.

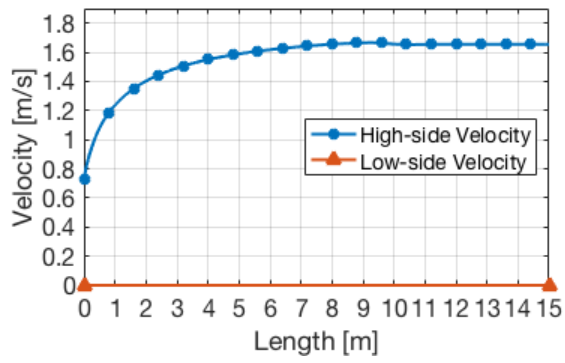


(a) Newtonian

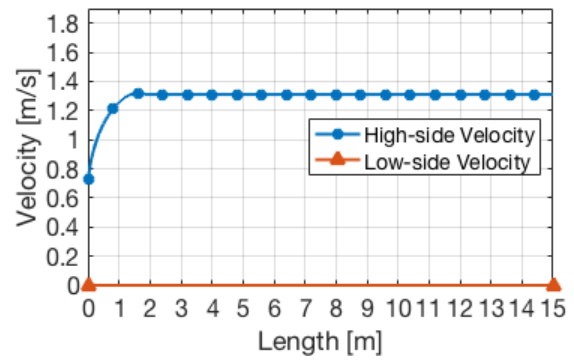


(b) Non-Newtonian

Figure A.13.: Comparison of pressure development for the eccentricity = 1 cases.



(a) Newtonian



(b) Non-Newtonian

Figure A.14.: Comparison of velocity development for the eccentricity = 1 cases for.

## A.4. Results - Eccentricity Cases: Velocity Profiles

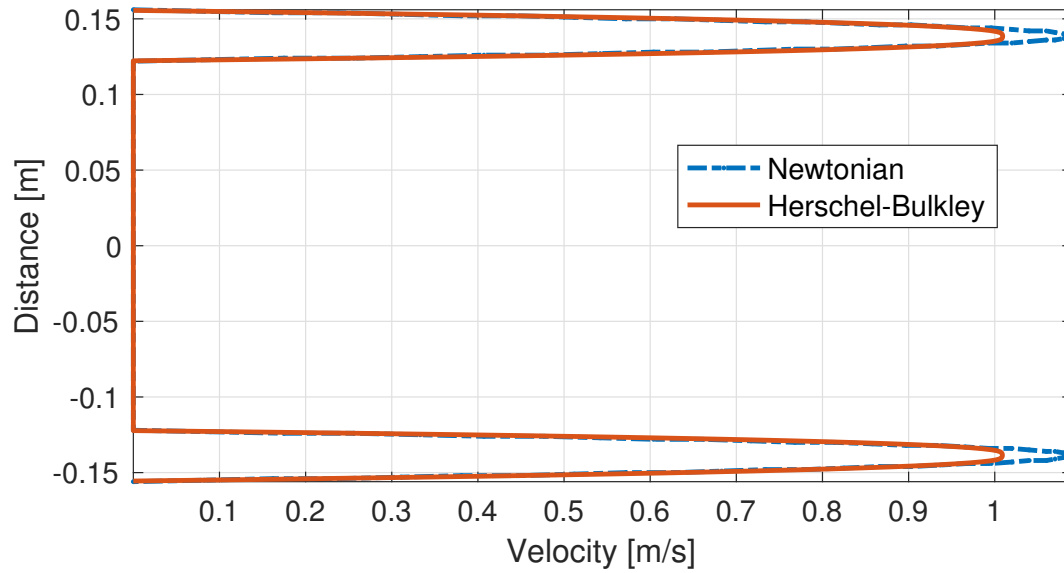


Figure A.15.: Comparison of velocity profiles for the eccentricity cases between Newtonian and Herschel-Bulkley rheology modelling for eccentricity=0.



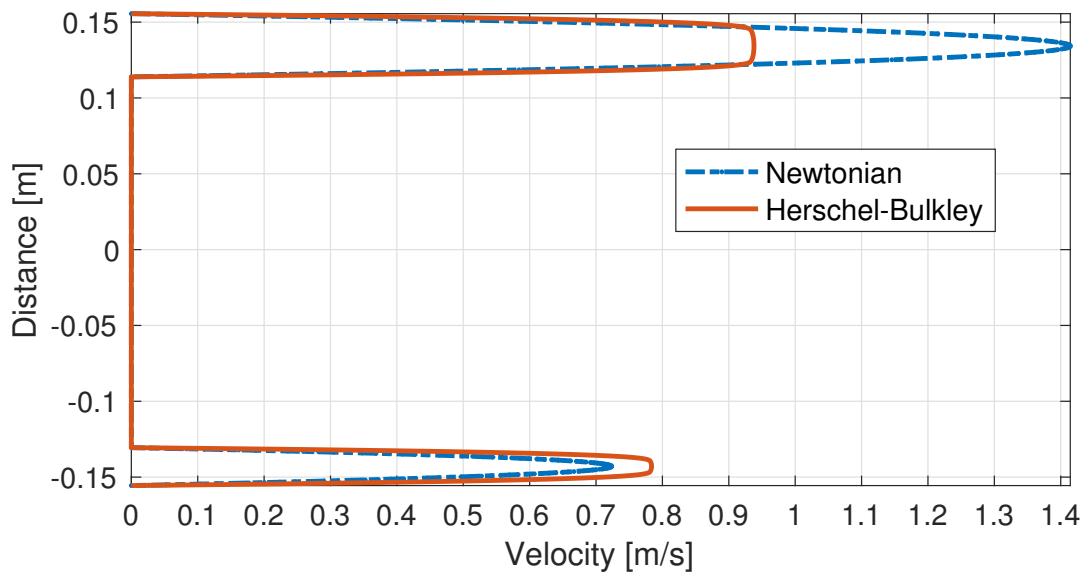


Figure A.16.: Comparison of velocity profiles for the eccentricity cases between Newtonian and Herschel-Bulkley rheology modelling for eccentricity=0.25.

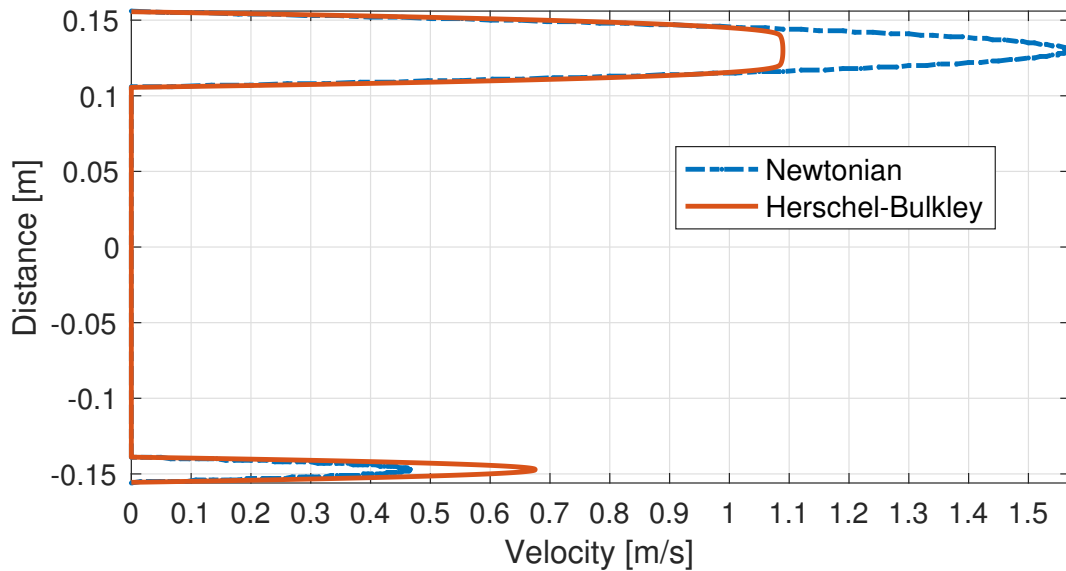


Figure A.17.: Comparison of velocity profiles for the eccentricity cases between Newtonian and Herschel-Bulkley rheology modelling for eccentricity=0.5.

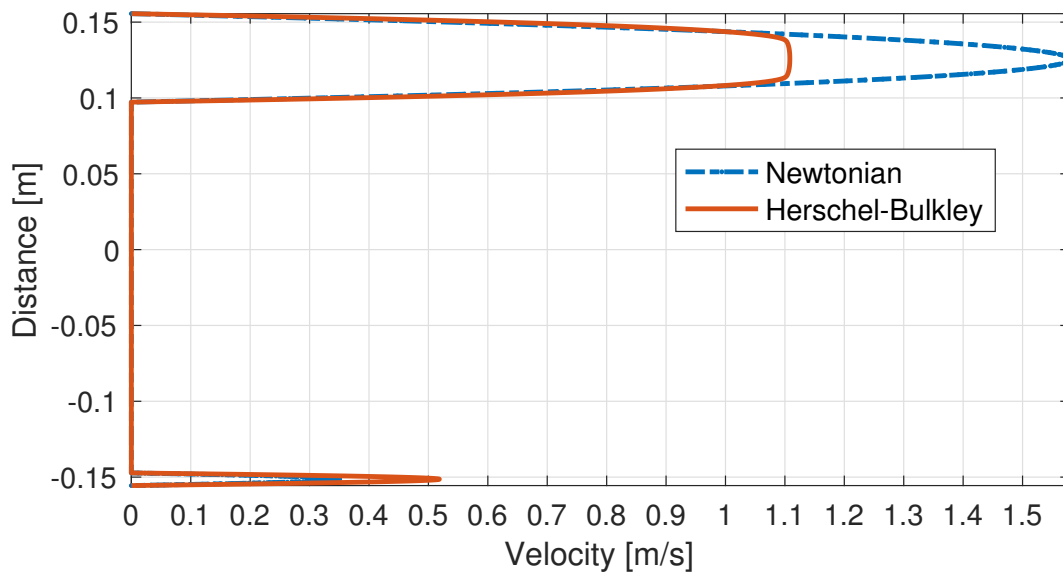


Figure A.18.: Comparison of velocity profiles for the eccentricity cases between Newtonian and Herschel-Bulkley rheology modelling for eccentricity=0.75.

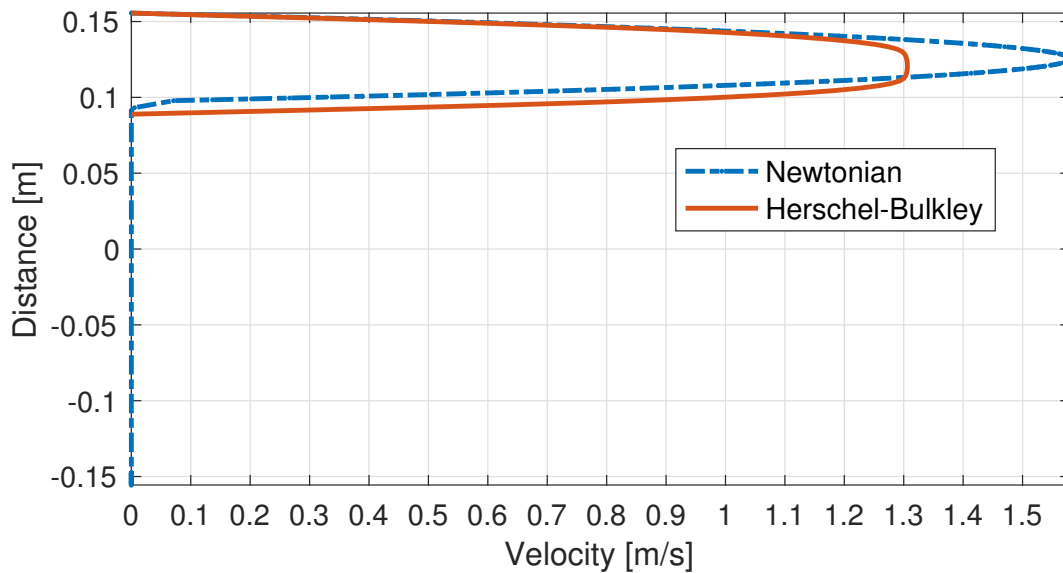


Figure A.19.: Comparison of velocity profiles for the eccentricity cases between Newtonian and Herschel-Bulkley rheology modelling for eccentricity=1.

## A.5. Results: Residuals

Residuals from: Single-phase Eccentricity Cases for Newtonian Model

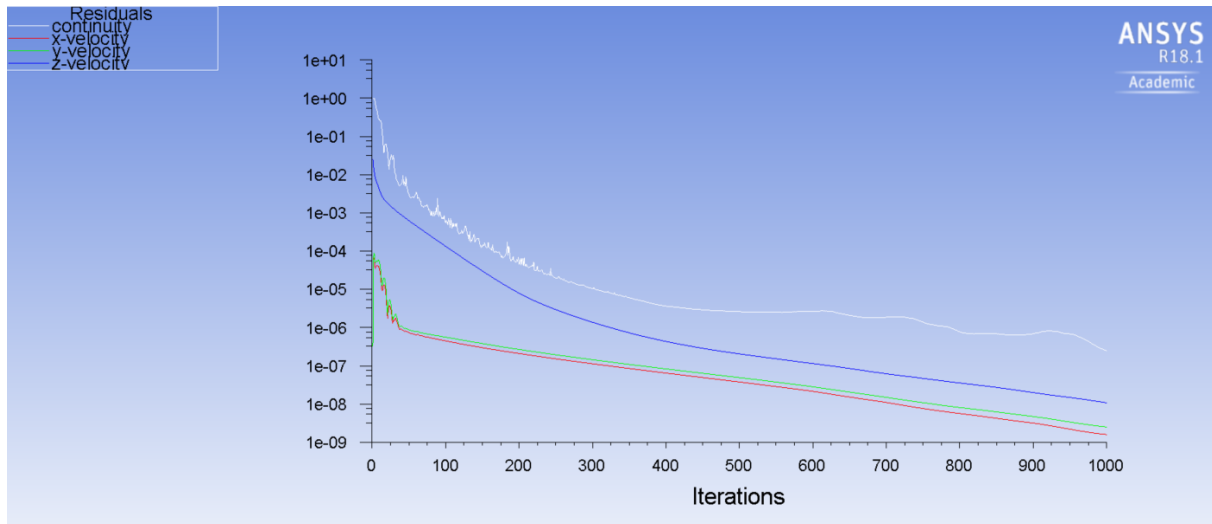


Figure A.20.: Residuals for simulation of Newtonian model with 0 eccentricity.

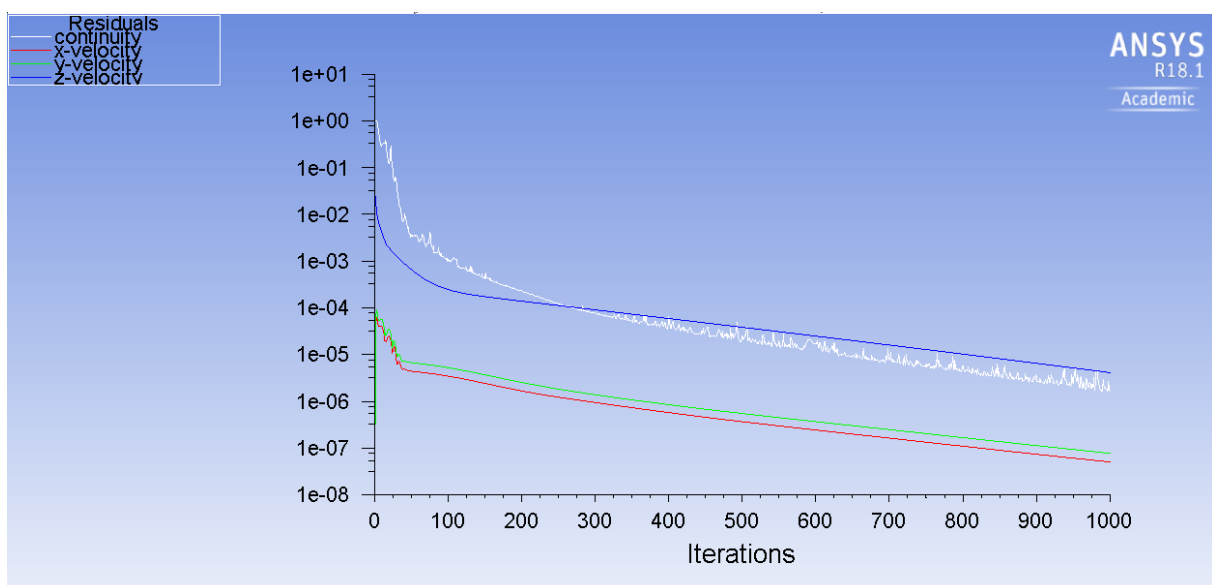


Figure A.21.: Residuals for simulation of Newtonian model with 0.25 eccentricity.

## A.5. RESULTS: RESIDUALS

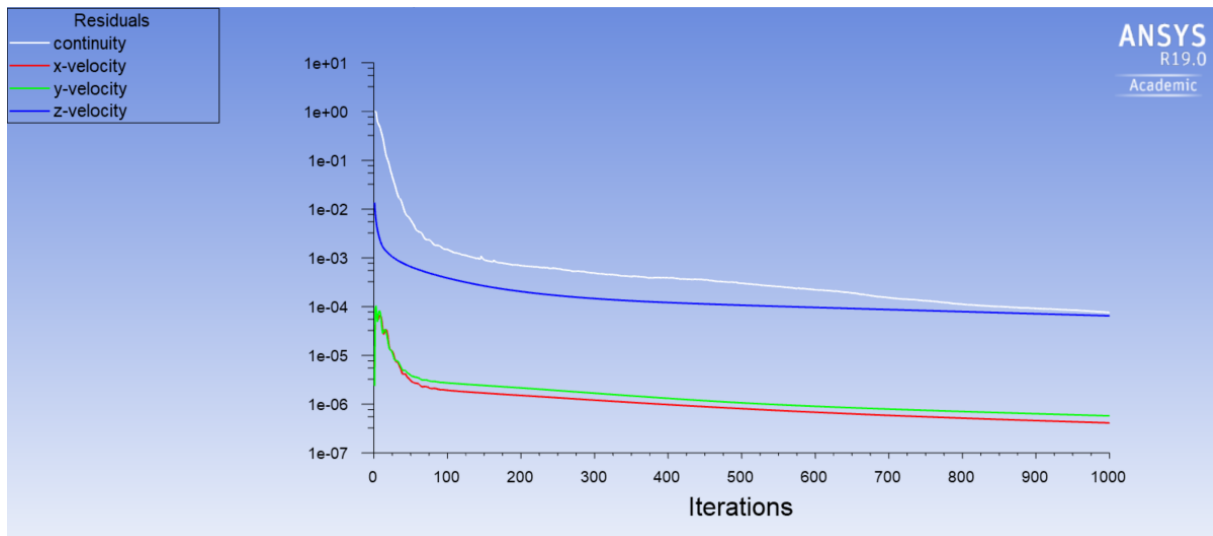


Figure A.22.: Residuals for simulation of Newtonian model with 0.50 eccentricity.

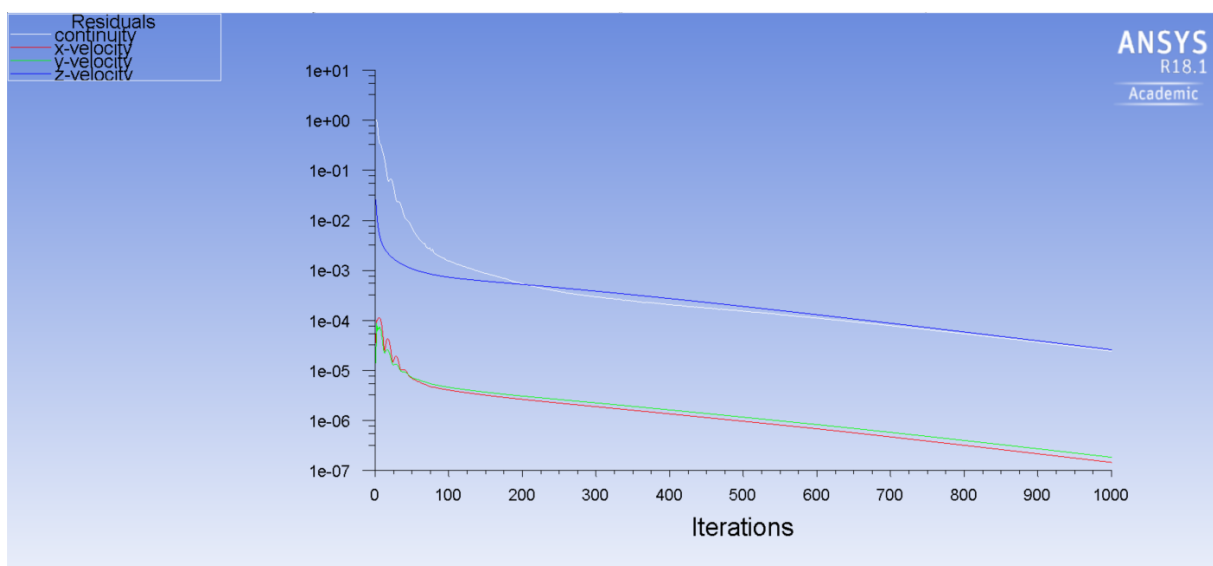


Figure A.23.: Residuals for simulation of Newtonian model with 0.75 eccentricity.

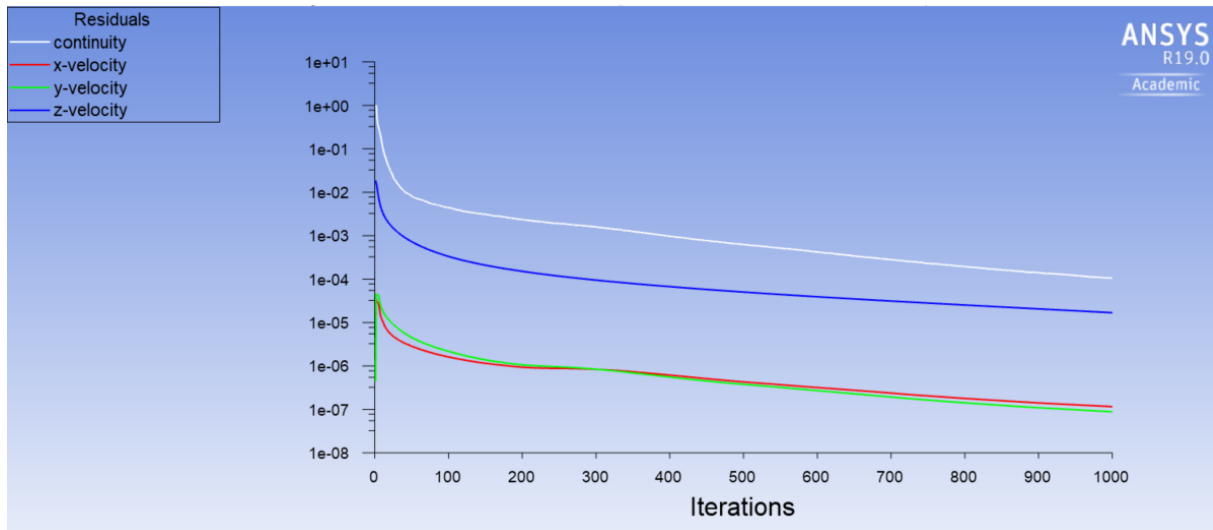


Figure A.24.: Residuals for simulation of Newtonian model with 1 eccentricity.

### Residuals from: Single-phase Eccentricity Cases for Herschel-Bulkley Model

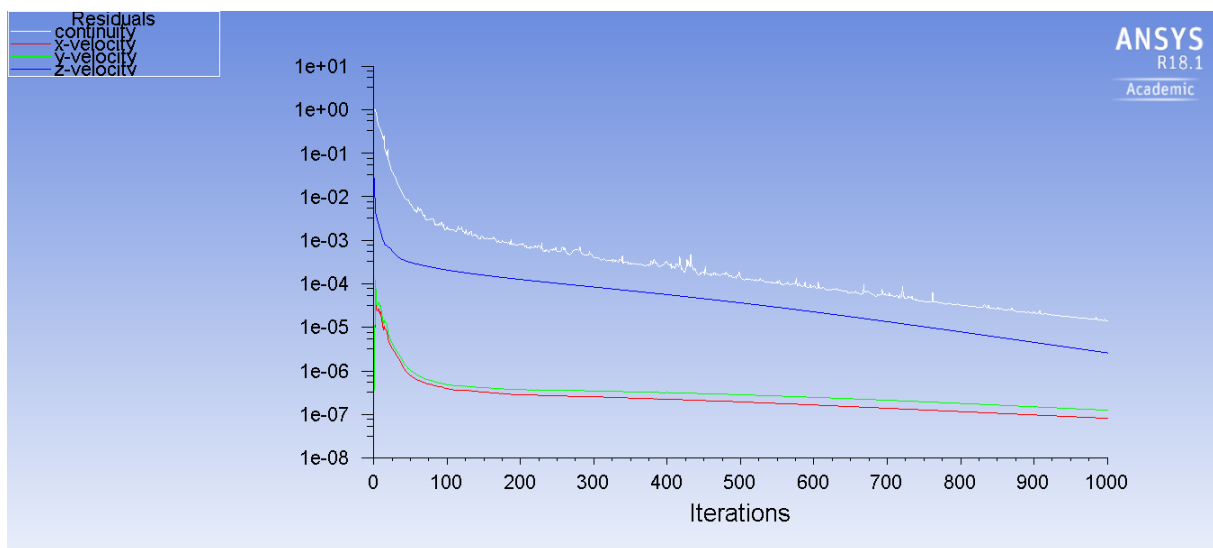


Figure A.25.: Residuals for simulation of Herschel-Bulkley model with 0 eccentricity.

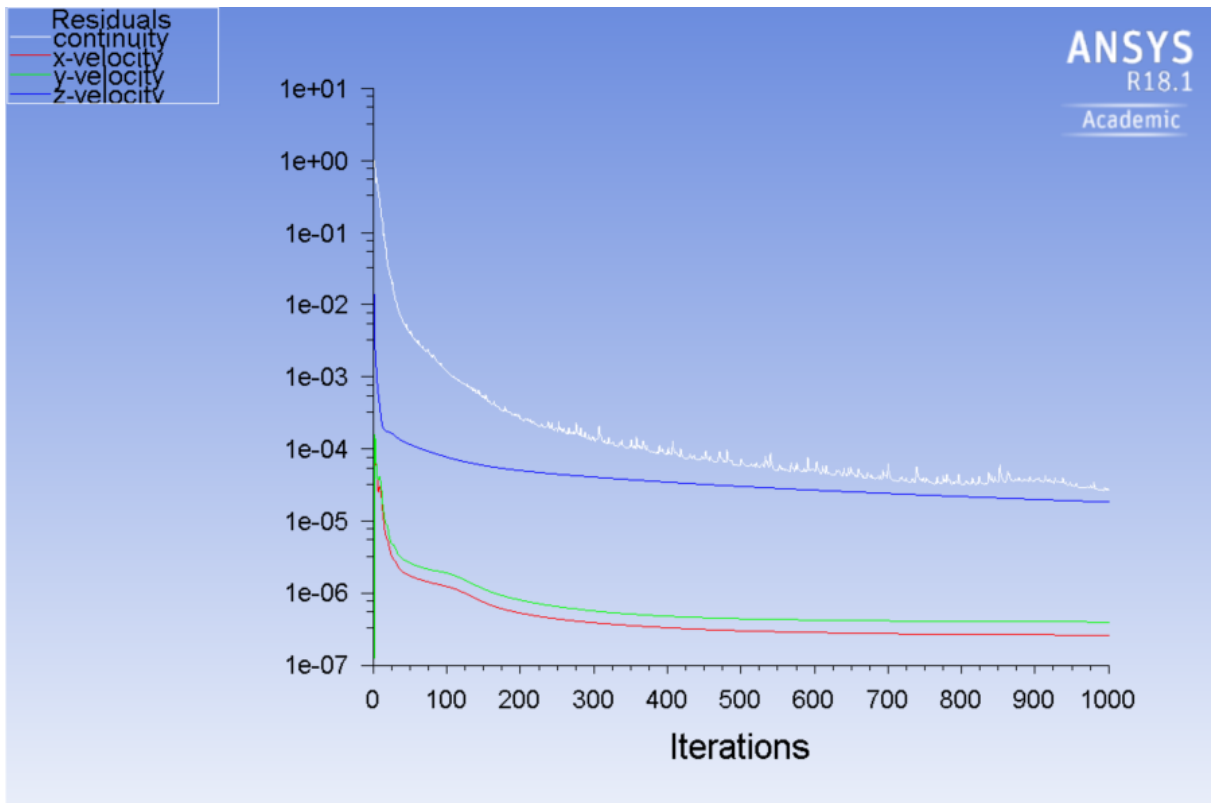


Figure A.26.: Residuals for simulation of Herschel-Bulkley model with 0.25 eccentricity.

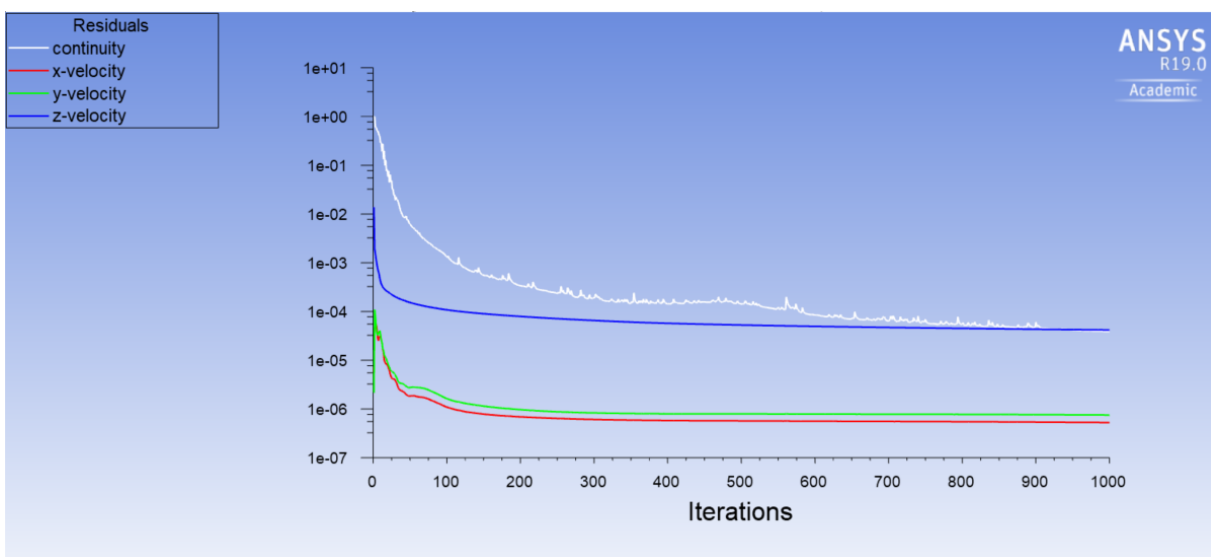


Figure A.27.: Residuals for simulation of Herschel-Bulkley model with 0.50 eccentricity.

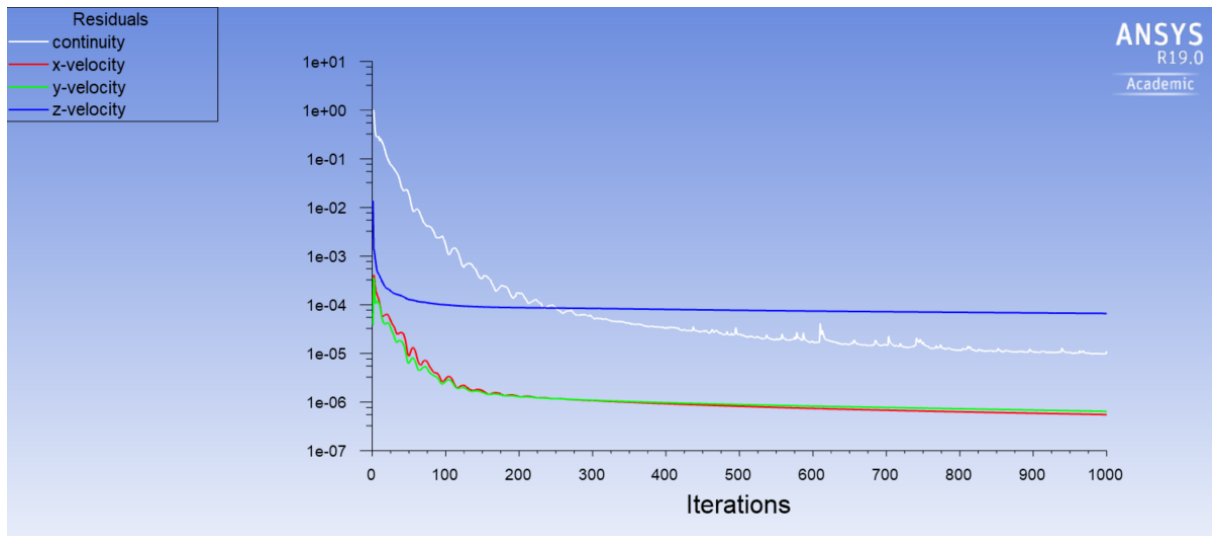


Figure A.28.: Residuals for simulation of Herschel-Bulkley model with 0.75 eccentricity.

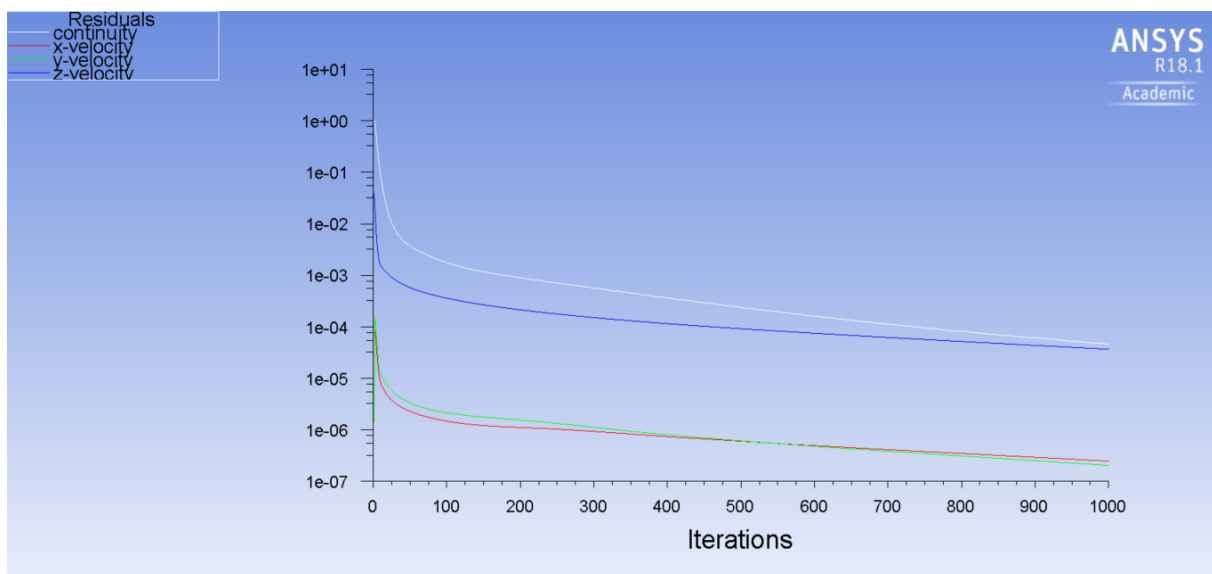


Figure A.29.: Residuals for simulation of Herschel-Bulkley model with 1 eccentricity.

## A.6. CFD Implementation

### A.6.1. Schematic of Approach for problem solving with CFD

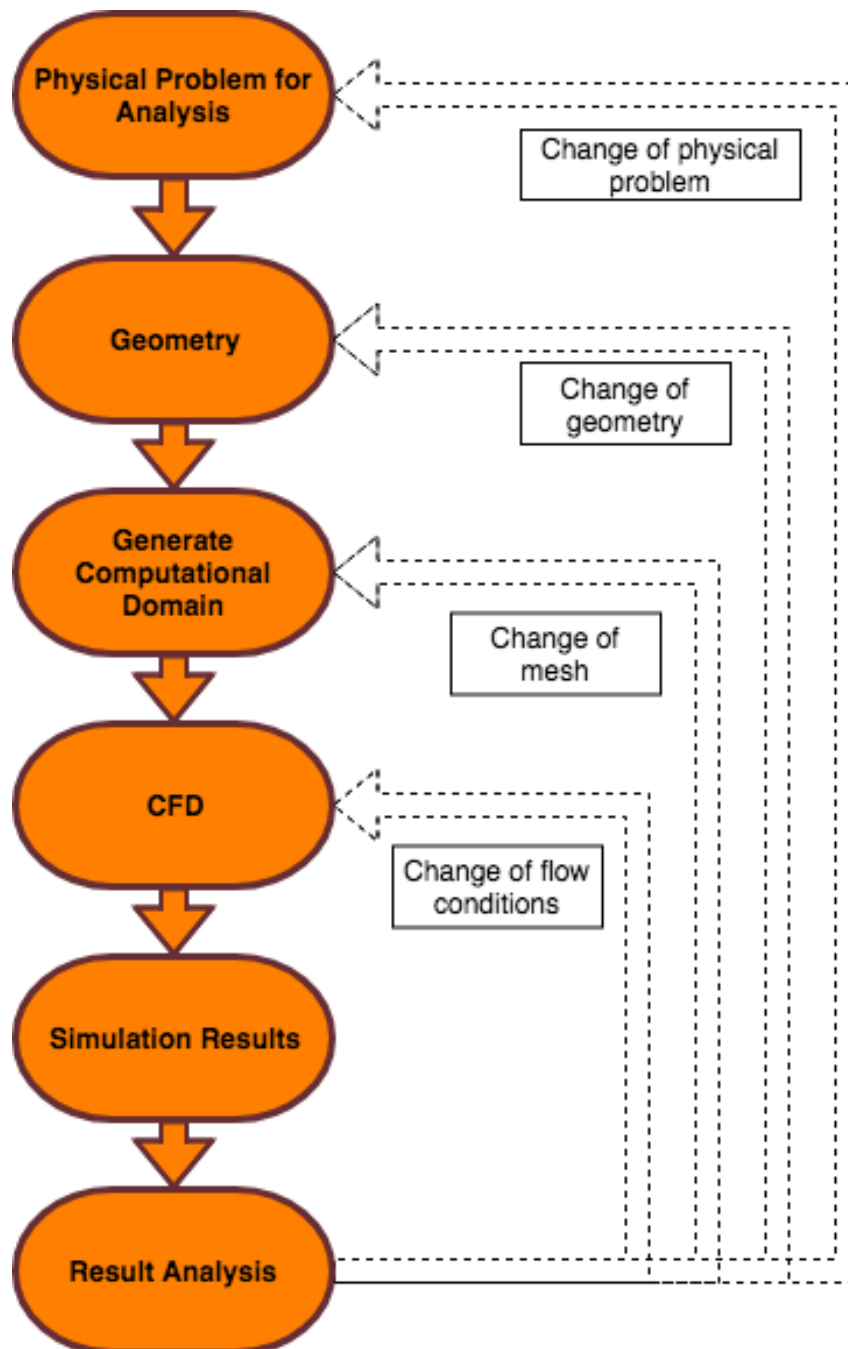


Figure A.30.: Schematic of the general algorithm using CFD.



A.6.2. Schematic of CFD Flowchart for Fluent

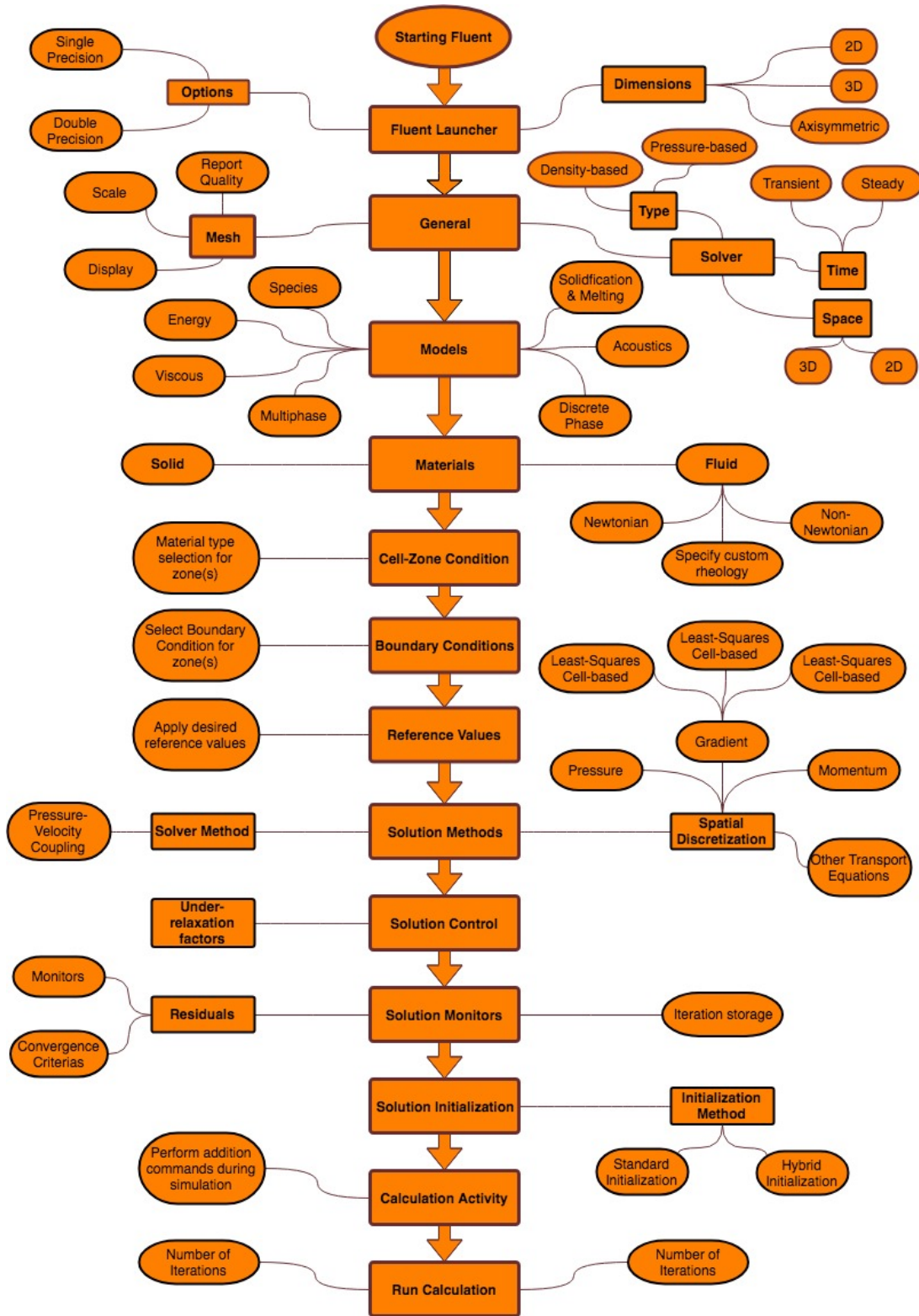


Figure A.31.: Schematic of the complete process in *Fluent* for solving CFD problems.

### A.6.3. Schematic of Solver

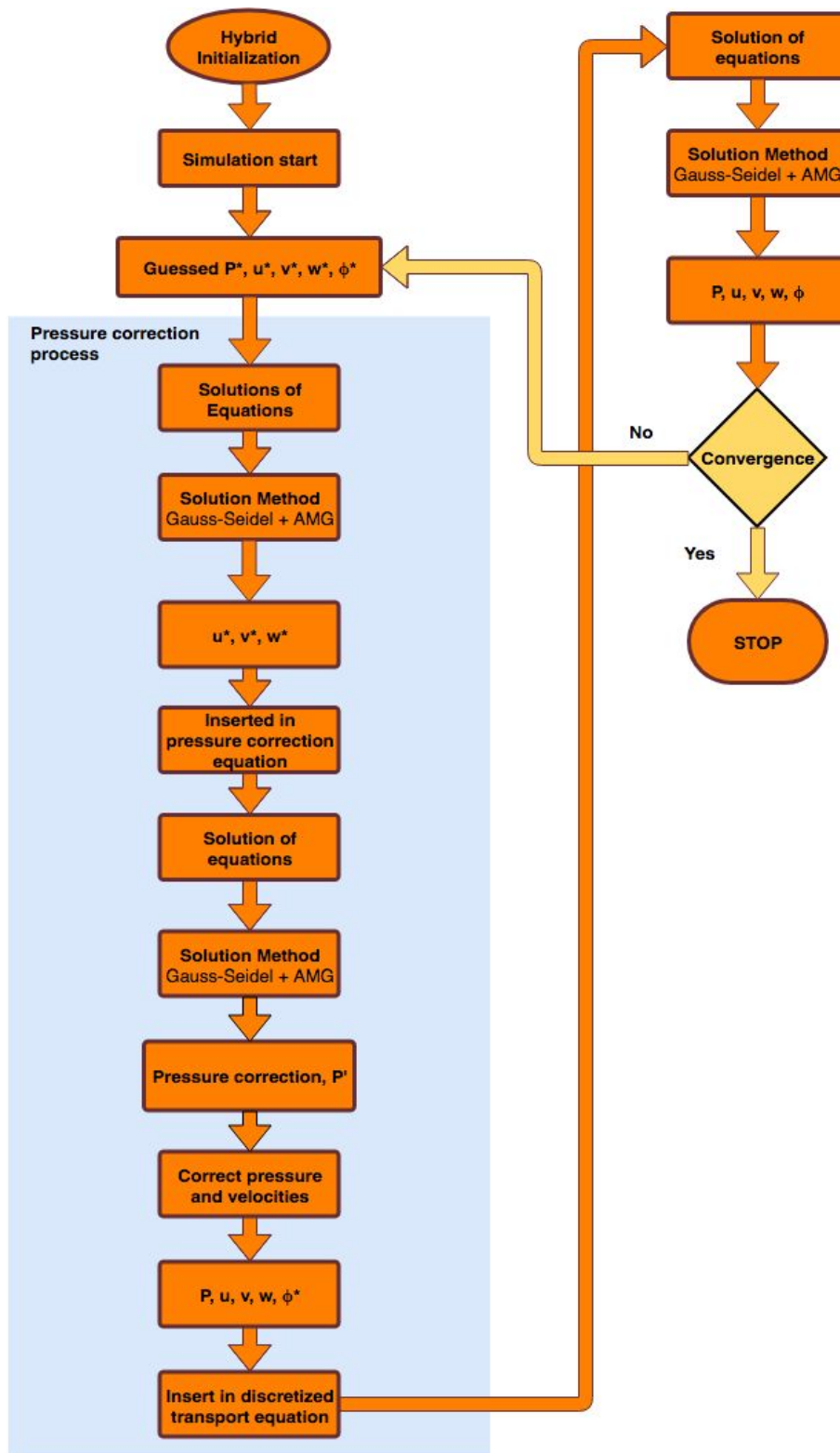


Figure A.32.: Schematic of the modified solver process for SIMPLE.

## A.7. Fundamentals of Fluid Dynamics

The governing equations of fluid flow represents mathematical statements of the conservation laws of physics, which are the following:

- **Conservation of Mass:** The mass of a fluid is conserved.
- **Conservation of Momentum:** From Newton's Second Law, the rate of change of momentum equals the sum of the forces on a fluid particle.
- **Conservation of Energy:** From the first law of thermodynamics, the rate of energy is equal to the sum of the rate of heat addition and the rate of work done on a fluid particle.

The fluid is regarded as a continuum. This means that the analysis of the kinematics and mechanical behaviour of material is modelled as a continuous mass, rather than as discrete particles, which was formulated by *Cauchy*.

For analysis of fluid flow, macroscopic length scales are assumed such that for molecular structures of matter in a microscale, the molecular motions are neglected. With the utilization of macroscopic properties, description of fluid behaviour can be reduced velocity, pressure, density and temperature, respectively. By the assumption of macroscopic point-of-view, properties are assumed to be averages over number of molecules. Consequently, a fluid particle becomes the smallest element possible, describing the fluid properties [15].

### A.7.1. Mass Conservation of a Fluid Element

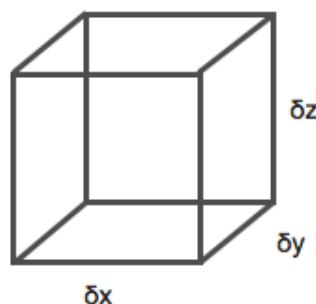


Figure A.33.: Fluid element for Conservations laws

Considering an element of fluid with sides  $\delta x$ ,  $\delta y$  and  $\delta z$ . The fluid element is assumed to be infinitesimal, visualized in Fig. A.33, which takes account of changes of mass, momentum and energy due to flow across its boundaries. The properties of the fluid element are functions of time and space, where the properties are a function of  $x$ ,  $y$ ,  $z$  and  $t$ , respectively.

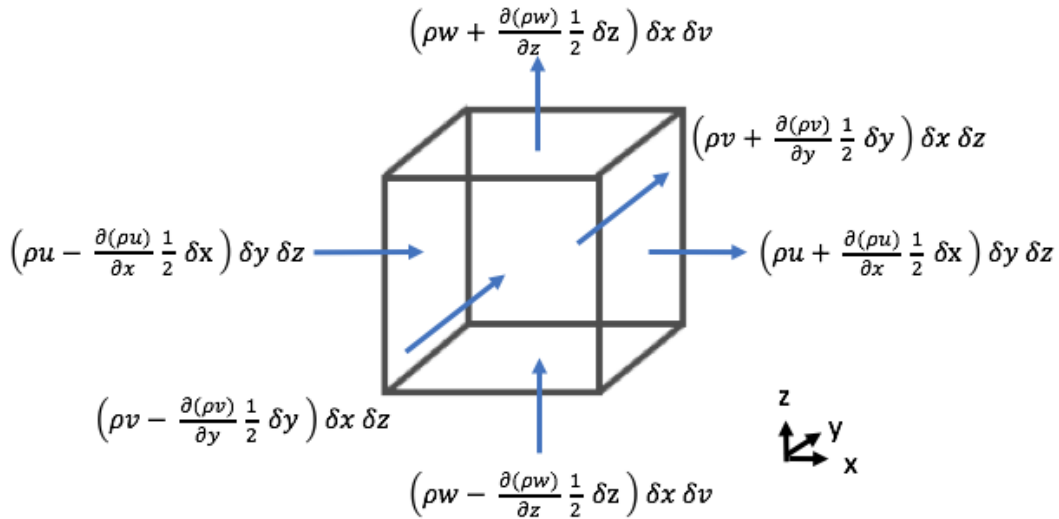


Figure A.34.: Mass flows in and out of a fluid element.

Considering the conservation of mass for a fluid element, the mass conservation states that the rate of change of mass in the fluid element has to be equal to net rate of flow of mass into the fluid element. This can mathematically be represented as:

$$\frac{\partial}{\partial t}(\rho \delta x \delta y \delta z) = \frac{\partial \rho}{\partial t} \delta x \delta y \delta z \tag{A.1}$$

The net rate of mass flow into an element across its boundaries, graphically shown in Fig. A.34 may be rearranged such that the mass conservation can be expressed as the following:

$$\frac{\partial \rho}{\partial t} + \frac{\partial \rho u}{\partial x} + \frac{\partial \rho v}{\partial y} + \frac{\partial \rho w}{\partial z} = 0 \tag{A.2}$$

or in a compact vector notation:

$$\frac{\partial \rho}{\partial t} + \nabla \cdot (\rho \mathbf{u}) = 0 \quad (\text{A.3})$$

, where  $\mathbf{u}$  is the velocity vector for  $u$ ,  $v$  and  $w$  in three-dimensions. The first term of eq. (A.3) describes the local rate of change in density and the second term describes the convective flow of mass across the boundaries of the domain.

Equation (A.3) is the unsteady, three-dimensional mass conservation, also known as the *continuity equation* at a point for a compressible fluid. Applying the assumption of incompressible fluid, i.e no change of density with respect to time yields:

$$\frac{\partial u}{\partial x} + \frac{\partial v}{\partial y} + \frac{\partial w}{\partial z} = 0 \quad (\text{A.4})$$

which in vector notation is expressed by:

$$\nabla \cdot \mathbf{u} = 0 \quad (\text{A.5})$$

This presented expression may also be called the *incompressibility constraint*, which a fluid element must satisfy to be referred to as an incompressible fluid.

### A.7.2. Momentum Equation in Three-Dimensions

The second governing physical law, which is Newton's second law, states that the rate of change of momentum of a fluid particle is equal to the sum of forces on a particle. The forces that affects fluid particles can be distinguished into two types. That is, surface forces and body forces. The surface forces consists of pressure forces, viscous forces and gravity force, and the body forces consists of centrifugal, Coriolis and electromagnetic force [15].

The state of stress of a fluid element is defined in terms of the pressure and nine viscous stress components. Pressure stresses, denoted  $P$ , and viscous stresses denoted by  $\tau$ . The

magnitude of a force resulting from a surface stress is the product of stress and area. The net force in an arbitrary direction is the sum of the force components acting in that direction on the fluid element. All the stress components can be graphically presented for a volume, as presented earlier, seen in Fig. A.35.

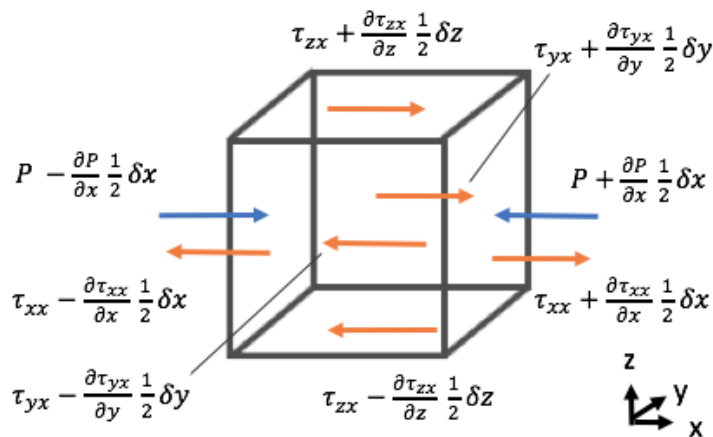


Figure A.35.: Stress components in a fluid element

The body forces is not discussed in further detail, but their overall effect can be included by defining a source,  $S_M$ , where the index  $M$  presents the source contribution from the momentum, where the source is momentum per unit volume per unit time.

Let  $\Psi$  be a any arbitrary direction of,  $x$ ,  $y$ , or  $z$ . The momentum equation for the  $\Psi$ -direction can be found by setting the rate of change of momentum of the fluid particle equal to the total force in the direction of the element, plus the rate of increase of the momentum due to sources. For example, with  $\Psi = x$ , we get

$$\rho \frac{Du}{Dt} = \frac{\partial(-P + \tau_{xx})}{\partial x} + \frac{\partial\tau_{xy}}{\partial y} + \frac{\partial\tau_{zx}}{\partial z} + S_{Mx} \quad (\text{A.6})$$

, where  $\frac{D}{Dt}$  is the material derivative, in the  $x$ -direction.

The accounts of surface stresses are accounted explicitly. The source terms  $S_M$  include contributions due to body forces.

### A.7.3. Equations of State

The dynamics of fluids can be described by a system of five PDEs: The mass conservation, the momentum equations in  $x$ -,  $y$ - and  $z$ -direction, and the energy equation. For these fundamental fluid equations, there exist four thermodynamic variables, that is  $\rho$ ,  $P$ ,  $e$  and  $T$ , which represents the density, pressure, specific internal energy and temperature, respectively. In the following, a brief discussions is presented in order to explain the link between these four variables.

The connection of the thermodynamic variables can be obtained by the assumption of *thermodynamic equilibrium*. The velocity components of a fluid element may be of significant magnitude, but usually varies in a low degree for a infinitely small change of position in space. Thus, the fluid will have the ability to thermodynamically adjust to the new set of conditions, which effectively are assumed instantaneous. In other words, a fluid element will always remain in thermodynamic equilibrium. Although, there exist exceptions, such as flows with the presence of shockwaves. Usually for these physical problem, a near-equilibrium assumption will be a reasonable approximation.

The state of a substance in thermodynamic equilibrium can be described by means of three state variables. These *equations of state* relate one variable to the other two state variables. Using the density and temperature as state variables, the state equations for pressure and specific internal energy or obtained and may be expressed as:

$$P = P(\rho, T) \quad (\text{A.7}) \quad e = e(\rho, T) \quad (\text{A.8})$$

For an ideal gas, the following, well-known, equation of state are:

$$P = \rho RT \quad (\text{A.9}) \quad e = C_v T \quad (\text{A.10})$$

In compressible flow, the equations of state provides a link between the energy equation and mass and momentum conservation equations. This linkage arises due to density variations as a results of pressure and temperature variations in the flow field.

For liquid and gases at low subsonic speeds ( $M \leq 0.3$ ), all fluids behave as an *incompressible fluid*. Without the presence of density variations, there are no link coupling the state variables. Therefore, the flow field can often be solved by solving the mass and momentum conservation.

#### A.7.4. Navier-Stokes Equations for Fluid Flow

In the following, isothermal flow is considered, i.e the energy conservation equation is not included, due to its non relevance for this thesis.

The conservation equation of momentum contain more unknowns represented as the viscous stress components,  $\tau_{ij}$ . An useful attribute is to express the viscous stresses as local deformation rates, also known as strain rates. In 3D flow analysis, the strain rates consists of linear and volumetric deformation rates.

Assuming isotropic liquids and gases, the rate of deformation of a fluid element becomes linear and has nine components in three-dimensions, of which six are independent in isotropic fluids [62]. Denoted by  $s_{ij}$ , where the suffix system is identical to that for stress components. The three linear elongating deformation components given by the following:

$$s_{xx} = \frac{\partial u}{\partial x} \qquad s_{yy} = \frac{\partial v}{\partial y} \qquad s_{zz} = \frac{\partial w}{\partial z}$$

as well as six shearing linear deformation components:

$$s_{xy} = s_{yx} = \frac{1}{2} \left( \frac{\partial u}{\partial y} + \frac{\partial v}{\partial x} \right) \qquad s_{xz} = s_{zx} = \frac{1}{2} \left( \frac{\partial u}{\partial z} + \frac{\partial w}{\partial x} \right) \qquad s_{yz} = s_{zy} = \frac{1}{2} \left( \frac{\partial v}{\partial z} + \frac{\partial w}{\partial y} \right)$$



Volumetric deformation may be expressed as:

$$\frac{\partial u}{\partial x} + \frac{\partial v}{\partial y} + \frac{\partial w}{\partial z} = \nabla \mathbf{u} \quad (\text{A.11})$$

For Newtonian fluids, the viscous stresses are proportional to the deformation rate. Newton's law of viscosity in three dimension, involves two constant of proportionality. Firstly, the dynamic viscosity,  $\mu$ , which relates stresses to linear deformations, and the second viscosity,  $\lambda$ , which relates the volumetric deformation to a difference between mechanical and thermodynamic pressure [63]. Enforcing this, we get nine viscous stress components, whereas six are independent given as in tensor notation:

$$\tau_{ii} = 2\mu \frac{\partial u_i}{\partial x_i} + \lambda \nabla \mathbf{u}, \quad i = j \quad (\text{A.12})$$

and

$$\tau_{ij} = \mu \left( \frac{\partial u_i}{\partial x_j} + \frac{\partial u_j}{\partial x_i} \right), \quad i \neq j \quad (\text{A.13})$$

, where the stress tensor here is represented with index notation.

The second viscosity,  $\lambda$ , has a small effect in practice [15]. For gases a reasonable approximation is the set the second viscosity as  $\lambda = -\frac{2}{3}\mu$  [62]. Since most liquids are incompressible, the mass conservation states that  $\nabla \mathbf{u} = 0$ , and the viscous terms a function of the local rate of linear deformation and dynamic viscosity.

By substituting the stresse into Eq. (A.6), yields the famous *Navier-Stokes* equations in the most useful form:

$$\frac{\partial(\rho \mathbf{u})}{\partial t} + \nabla \cdot (\rho \mathbf{u} \otimes \mathbf{u}) = -\nabla P + \mu \nabla \cdot \tau + S_M \quad (\text{A.14})$$

The continuity equation, momentum equations, energy equation, and equations of state

constitute the governing equations of fluid flow.